DESIGNING AUTOPILOT AND GUIDANCE ALGORITHMS TO CONTROL TRANSLATIONAL AND ROTATIONAL DYNAMICS OF A FIXED WING VTOL UAV

A THESIS SUBMITTED TO
THE GRADUATE SCHOOL OF NATURAL AND APPLIED SCIENCES
OF
MIDDLE EAST TECHNICAL UNIVERSITY

BY

ANIL GÜÇLÜ

IN PARTIAL FULFILLMENT OF THE REQUIREMENTS
FOR
THE DEGREE OF DOCTOR OF PHILOSOPHY
IN
AEROSPACE ENGINEERING

JULY 2020

Approval of the thesis:

DESIGNING AUTOPILOT AND GUIDANCE ALGORITHMS TO CONTROL TRANSLATIONAL AND ROTATIONAL DYNAMICS OF A FIXED WING VTOL UAV

submitted by **ANIL GÜÇLÜ** in partial fulfillment of the requirements for the degree of **Doctor of Philosophy in Aerospace Engineering Department, Middle East Technical University** by,

Prof. Dr. Halil Kalıpçılar
Dean, Graduate School of **Natural and Applied Sciences** _____

Prof. Dr. İsmail Hakkı Tuncer
Head of Department, **Aerospace Engineering** _____

Prof. Dr. Dilek Funda Kurtuluş
Supervisor, **Aerospace Engineering, METU** _____

Assist. Prof. Dr. Kutluk Bilge Arıkan
Co-supervisor, **Mechanical Engineering, TED University** _____

Examining Committee Members:

Prof. Dr. Ozan Tekinalp
Aerospace Engineering, METU _____

Prof. Dr. Dilek Funda Kurtuluş
Aerospace Engineering, METU _____

Prof. Dr. Ünver Kaynak
Aerospace Engineering, Yıldırım Beyazıt University _____

Prof. Dr. Coşku Kasnakoğlu
Electrical and Electronics Engineering, TOBB ETU _____

Assist. Prof. Dr. Ali Emre Turgut
Mechanical Engineering, METU _____

Date:

I hereby declare that all information in this document has been obtained and presented in accordance with academic rules and ethical conduct. I also declare that, as required by these rules and conduct, I have fully cited and referenced all material and results that are not original to this work.

Name, Surname: Anıl Güçlü

Signature :

ABSTRACT

DESIGNING AUTOPILOT AND GUIDANCE ALGORITHMS TO CONTROL TRANSLATIONAL AND ROTATIONAL DYNAMICS OF A FIXED WING VTOL UAV

Güçlü, Anıl
Ph.D., Department of Aerospace Engineering
Supervisor: Prof. Dr. Dilek Funda Kurtuluş
Co-Supervisor: Assist. Prof. Dr. Kutluk Bilge Arıkan

July 2020, 123 pages

Guidance and autopilot algorithms are designed and applied to a fixed wing VTOL air vehicle. The algorithms are developed on a rotary wing and a fixed air vehicle. Each air vehicle is identified by experimentation to reduce the discrepancies among the system model and the actual air vehicles. Designed controllers for the air vehicles are deployed to Pixhawk Cube controller board. Indoor and outdoor flight tests are carried out. For the rotary wing air vehicle, active disturbance rejection control algorithms are used to control the states. Trajectory tracking is also carried out with distinct load cases which are unloaded, asymmetrically placed constant load, and slung load. Disturbances which are induced by the loads and the environment are estimated and rejected during indoor and outdoor tests. Control allocation algorithms are focused and applied to a fixed wing VTOL air vehicle for the flight phases among vertical and horizontal flights. Consumed energy during the flight is minimized by a dynamic direct control allocation algorithm. Desired force and moments (virtual inputs) which comes from the controllers are mapped to the set of actuators via control allocation algorithms. The fixed wing VTOL air vehicle is loaded with two loads

underneath of the main wing. In the scenario, the fixed wing VTOL air vehicle takes off with loads. One of them is released at a point, and then the asymmetric load is carried to another point. Developed active disturbance control allocation and control allocation algorithms are used together.

Keywords: ADRC, fixed wing, VTOL, UAV, control allocation, Pixhawk

ÖZ

DİKEY İNİŞ KALKIŞ YAPABİLEN SABİT KANATLI HAVA ARACININ DOĞRUSAL VE DÖNÜSEL DİNAMİKLERİNİN DENETİMİ İÇİN GÜDÜM VE OTOPİLOT ALGORİTMASI TASARIMI

Güçlü, Anıl
Doktora, Havacılık ve Uzay Mühendisliği Bölümü
Tez Yöneticisi: Prof. Dr. Dilek Funda Kurtuluş
Ortak Tez Yöneticisi: Dr. Öğr. Üyesi. Kutluk Bilge Arıkan

Temmuz 2020 , 123 sayfa

Sabit ve döner kanatlı hava aracının ardından dikey iniş kalkış yapabilen sabit kanatlı hava aracına yönelik güdüm-otopilot algoritması tasarlanmış ve gerçek sisteme uygulanmıştır. Sistem modelleri ile hava araçları arasındaki farkı azaltmak için hava araçları deneysel olarak test edilmiştir. Uçuşlu testler, tasarlanan algoritmaların Pixhawk Cube denetimci kartına yüklenmesi ile hava araçları üzerinde test edilmiştir. Döner kanatlı hava aracı dinamiklerinin denetimi için doğrusal aktif bozucu savurucu tasarlanmıştır. Yüksüz, asimetrik yerleştirilen sabit yük ve salınan yük ile yörünge takibi yapılmıştır. Yüklerden ve çevreden gelen bozucu etkiler bertaraf edilmiştir. Sabit kanatlı dikey iniş kalkış yapabilen hava aracının yatay ve dikey uçuş fazları arasındaki geçişler için denetimci tahsis algoritması üzerine odaklanılmıştır. Uçuş boyunca harcanan enerji dinamik denetimci tahsisi algoritması ile minimize edilmiştir. Denetimci çıktısı olan kuvvet ve momentler, bu algoritma ile uygun eyleyicilere dağıtılarak uçuşun kritik fazları olan yatay ve dikey uçuşlar arasındaki geçiş fazlarında minimum enerji harcanması sağlanmıştır. Tasarlanan denetimci ve dinamik denetimci tahsisi al-

goritmaları bir senaryo ile test edilmiştir. Senaryo kapsamında, sabit kanatlı dikey iniş kalkış yapabilen hava aracı simetrik olarak yüklenmiştir. Yüklerin farklı noktalara taşınmaktadır. Yükün birinin bırakılmasının ardından, sabit kanatlı hava aracı asimetrik olarak yüklenmiş olmaktadır ve varış noktasına bu şekilde uçmaktadır.

Anahtar Kelimeler: ADRC, fixed wing, VTOL, UAV, denetimci tahsisi, Pixhawk

This dissertation is dedicated to my wife, Selva SARGIN GÜÇLÜ, who encouraged me to pursue my dreams and finish my dissertation.

ACKNOWLEDGMENTS

I want to express my greatest appreciation to my supervisor Prof. Dr. D. Funda KURTULUŞ for her leadership, advice, criticism, encouragements and understanding throughout the research.

I also want to thanks to Dr. K. Bilge ARIKAN who is ready to help and motivate every time I need. His guidance and brotherhood are the principal force that motivate me during the research.

I want to thank my wife Selva SARGIN GÜÇLÜ for her endless motivation and help. My son, Berk GÜÇLÜ cheers me up with his smile everytime.

I want to thank you my family; Ümit GÜÇLÜ, Yılmaz GÜÇLÜ, Egemen GÜÇLÜ, Zuhal SARGIN, Aydoğan SARGIN, and Esra SARGIN. I am very appreciate to Kaan GÖKER and Egemen GÜÇLÜ for their help during the indoor and outdoor flight tests.

I want to thank İbrahim OĞUL for his support during the experimental studies of the fixed wing VTOL air vehicle.

This work was supported by the ROKETSAN Missile Inc. [project number 90003, W-6686]; the Middle East Technical University, SAYP [project number 2015-03-13-2-00-06]; and the Presidency of Defence Industries.

TABLE OF CONTENTS

ABSTRACT v

ÖZ vii

ACKNOWLEDGMENTS x

TABLE OF CONTENTS xi

LIST OF TABLES xiv

LIST OF FIGURES xvi

LIST OF SYMBOLS xxi

CHAPTERS

1 INTRODUCTION 1

1.1 Motivation and Problem Definition 2

1.2 Literature Review 4

1.3 Proposed Methods and Models 7

1.4 Contributions and Novelties 8

1.5 The Outline of the Thesis 9

2 ROTARY WING AIR VEHICLE 11

2.1 Physical System 11

2.1.1 Controller board 12

2.1.2 Thrust unit 14

2.2 System Identification 15
2.2.1 Bifilar pendulum test for rotary wing air vehicle 15
2.2.2 Thrust measurement for rotary wing air vehicle 17
2.3 Mathematical Modelling of the Rotary Wing Air Vehicle 20
3 FIXED WING AIR VEHICLE 25
3.1 Physical System 25
3.2 System Identification 25
3.2.1 Bifilar pendulum test for fixed wing air vehicle 25
3.2.2 Thrust measurement for fixed wing air vehicle 27
3.2.3 Control surface identification for fixed wing air vehicle 27
3.2.4 Aerodynamic analysis for fixed wing air vehicle 28
3.3 Mathematical Modelling of the Fixed Wing Air Vehicle 31
4 FIXED WING VTOL AIR VEHICLE 35
4.1 Physical System 36
4.2 System Identification 37
4.2.1 Bifilar pendulum test for fixed wing VTOL air vehicle 38
4.2.2 Thrust measurement for fixed wing VTOL air vehicle 40
4.2.3 Aerodynamic analysis for fixed wing VTOL air vehicle 42
4.3 Mathematical Modelling of the Fixed Wing VTOL Air Vehicle 45
5 CONTROLLER DESIGN 49
5.1 PID controller 49
5.2 Linear Active Disturbance Rejection Controller (LADRC) 50
5.2.1 Second Order ADRC (without actuator dynamic) 52

5.2.2 Third Order ADRC (with actuator dynamic) 55
5.2.3 n^{th} order ADRC 58
5.3 Control Allocation 60
5.3.1 Constrained linear control allocation methods 63
5.3.1.1 Redistributed pseudo-inverse 63
5.3.1.2 Daisy chaining 64
5.3.1.3 Direct allocation 65
5.3.2 Linear and Quadratic Programming Optimization Methods . . 65
5.3.3 Solving the Linear Problem (LP) Problem 67
5.3.4 Control allocation algorithm comparisons 68
6 SIMULATION AND FLIGHT TESTS 69
6.1 Rotary wing air vehicle 69
6.1.1 Trajectory tracking 69
6.1.2 Attitude control 70
6.1.3 Results 71
6.2 Fixed wing air vehicle 87
6.3 Fixed wing VTOL air vehicle 89
7 CONCLUSION 105
REFERENCES 107
APPENDIX
A CODE DEPLOYMENT FROM MATLAB TO PIXHAWK CUBE 117
CURRICULUM VITAE 121

LIST OF TABLES

TABLES

Table 1.1 Pros and Cons of Air Vehicles 3

Table 1.2 Fixed wing VTOL air vehicle examples 6

Table 2.1 Components of the rotary wing air vehicle 11

Table 2.2 Parameters of bifilar pendulum test 16

Table 2.3 Mass moment of inertias of the rotary wing air vehicle 17

Table 2.4 BLDCs transfer functions 20

Table 3.1 Specifications of the fixed wing air vehicle 26

Table 3.2 Mass moment of inertias of the fixed wing air vehicle 26

Table 3.3 PWM signal and control surface position relations 28

Table 3.4 Fixed wing air vehicle properties 30

Table 3.5 Fixed wing air vehicle longitudinal derivatives 31

Table 3.6 Fixed wing air vehicle lateral derivatives 31

Table 4.1 Fixed wing VTOL air vehicle parts 37

Table 4.2 Parameters of fixed wing VTOL air vehicle bifilar pendulum test . . 40

Table 4.3 Mass moment of inertias of the fixed wing VTOL air vehicle 40

Table 4.4 Fixed wing VTOL air vehicle properties 44

Table 4.5 Fixed wing VTOL air vehicle longitudinal derivatives 44

Table 4.6 Fixed wing VTOL air vehicle lateral derivatives 45

Table 4.7 Fixed wing VTOL air vehicle notations 46

Table 5.1 Comparison of the control allocation algorithms 68

Table 6.1 Flight test types 73

Table 6.2 Controller gains 74

Table 6.3 Fixed wing air vehicle controller gains 87

Table 6.4 ISE values of the roll and pitch states 88

LIST OF FIGURES

FIGURES

Figure 1.1 First fixed and rotary wing air vehicles 1

Figure 1.2 Fixed wing types [6] 2

Figure 1.3 Rotary wing types [7] 2

Figure 2.1 Assembled rotary wing air vehicle 12

Figure 2.2 Pixhawk Cube measured Euler angles 13

Figure 2.3 Pixhawk Cube data loss 14

Figure 2.4 Thrust unit 15

Figure 2.5 Bifilar pendulum experiment 16

Figure 2.6 Bifilar pendulum experiment of the rotary wing air vehicle for $roll$ and yaw axes 17

Figure 2.7 Thrust measurement setup 18

Figure 2.8 Measured thrust forces 19

Figure 2.9 Measured rotational velocities 19

Figure 2.10 Rotary wing air vehicle scheme 20

Figure 3.1 Fixed wing air vehicle 26

Figure 3.2 Thrust force and rotational velocity due to PWM duty ratio . . . 27

Figure 3.3 Angle measurement apparatus 28

Figure 3.4 Aerodynamic analysis of fixed wing air vehicle 29

Figure 3.5 Fixed wing air vehicle scheme 32

Figure 4.1 Fixed wing VTOL air vehicle scheme 35

Figure 4.2 Fixed wing VTOL air vehicle flight phases 36

Figure 4.3 Fixed wing VTOL air vehicle scheme 37

Figure 4.4 Bifilar pendulum experiment of fixed wing VTOL air vehicle . . 38

Figure 4.5 Oscillation data of fixed wing VTOL air vehicle in *roll* axis . . . 39

Figure 4.6 Oscillation data of fixed wing VTOL air vehicle in *yaw* axis . . . 39

Figure 4.7 Vertical thrusts of *motors 1-4* 41

Figure 4.8 Rotational velocities of *motors 1-4* 41

Figure 4.9 Horizontal thrust and rotational velocity of *motor 5* 41

Figure 4.10 Aerodynamic analysis of fixed wing VTOL air vehicle 43

Figure 4.11 Fixed wing VTOL air vehicle 45

Figure 5.1 Closed loop system with a PID controller 50

Figure 5.2 Block diagram of second order closed loop system 52

Figure 5.3 Block diagram of third order closed loop system 55

Figure 5.4 Control allocation application areas 60

Figure 5.5 Conventional aircraft control surfaces 61

Figure 5.6 Control allocation algorithm architecture 62

Figure 5.7 Types of the control allocation algorithms 62

Figure 6.1 Tracking controller structure 71
Figure 6.2 Test methodology 72
Figure 6.3 Indoor and outdoor flights 72
Figure 6.4 Load position 73
Figure 6.5 Flight trajectories 73
Figure 6.6 Flight trajectories for different loads for 20m and 40m flights . . 75
Figure 6.7 Flight trajectories for different controllers for 20m and 40m flights 76
Figure 6.8 Scaled ISE values for different controllers and flight cases 77
Figure 6.9 Roll dynamics for unloaded case - 20m flight 77
Figure 6.10 Roll dynamics for unloaded case - 40m flight 78
Figure 6.11 Pitch dynamics for unloaded case - 20m flight 78
Figure 6.12 Pitch dynamics for unloaded case - 40m flight 79
Figure 6.13 Disturbance estimation for static loaded case - 20m flight 79
Figure 6.14 Disturbance estimation for static loaded case - 40m flight 80
Figure 6.15 Roll dynamics for static loaded case - 20m flight 81
Figure 6.16 Roll dynamics for static loaded case - 40m flight 81
Figure 6.17 Pitch dynamics for static loaded case - 20m flight 82
Figure 6.18 Pitch dynamics for static loaded case - 40m flight 82
Figure 6.20 Disturbance estimation for slung loaded case - 40m flight 83
Figure 6.19 Disturbance estimation for slung loaded case - 20m flight 83
Figure 6.21 Roll dynamics for slung loaded case - 20m flight 84
Figure 6.22 Roll dynamics for slung loaded case - 40m flight 85

Figure 6.23 Pitch dynamics for slung loaded case - 20m flight 85

Figure 6.24 Pitch dynamics for slung loaded case - 40m flight 86

Figure 6.25 Scaled ISE values for different controllers and flight cases 86

Figure 6.26 Fixed wing air vehicle 88

Figure 6.27 Flight test data - roll control 88

Figure 6.28 Flight test data - pitch control 88

Figure 6.29 Flowchart of the flight phases 89

Figure 6.30 Dynamic control allocation inputs and outputs 90

Figure 6.31 Architecture of direct control allocation algorithm 91

Figure 6.34 Positions in NED coordinate system 92

Figure 6.32 XZ trajectories of different control allocation algorithms 93

Figure 6.33 Consumed powers of different control allocation algorithms . . . 93

Figure 6.35 Velocities in NED coordinate system 94

Figure 6.36 Fixed wing VTOL air vehicle flight scenario 94

Figure 6.37 Fixed wing VTOL air vehicle flight path 96

Figure 6.38 Fixed wing VTOL air vehicle positions in NED coordinate frame 96

Figure 6.39 Fixed wing VTOL air vehicle velocities in NED coordinate frame 97

Figure 6.40 Fixed wing VTOL air vehicle Euler angles 97

Figure 6.41 Force and moment distributions 99

Figure 6.42 Power consumption of rotary wings of fixed wing VTOL air vehicle 101

Figure 6.43 Power consumption of fixed wings of fixed wing VTOL air vehicle 101

Figure 6.44 Power consumption of fixed wing VTOL air vehicle 102

Figure 6.45 Control surface positions of fixed wing VTOL air vehicle 103

Figure 6.46 Vertical thrusters' velocities of fixed wing VTOL air vehicle . . . 103

Figure A.1 Pixhawk Toolchain setup (screenshot) 117

Figure A.2 Ubuntu Bash in Microsoft store (screenshot) 118

Figure A.3 PX4 Installation and CMake Installation (screenshot) 119

LIST OF SYMBOLS

F	Force
M	Moment
I	Mass moment of inertia
C_P	Pressure coefficient
C_D	Drag coefficient
C_L	Lift coefficient
I_x	Mass moment of inertia around x axis
I_y	Mass moment of inertia around y axis
I_z	Mass moment of inertia around z axis
L	Transformation matrix
L	Roll moment
M	Pitch moment
N	Yaw moment
cs_a	Aileron position
cs_e	Elevator position
cs_r	Rudder position
b	Thrust coefficient of propeller
d	Drag coefficient of propeller
dt	Duty ratio of PWM signal
g	gravitational acceleration
l	Moment arm of the rotary wing air vehicle
m	mass
p	roll rate in body fixed frame
q	pitch rate in body fixed frame

r	yaw rate in body fixed frame
u	translational velocity along x axis in body fixed frame
v	translational velocity along y axis in body fixed frame
w	translational velocity along z axis in body fixed frame

List of Greek letters

α	Angle of attack
θ	Pitch angle
ϕ	Roll angle
ψ	Yaw angle
θ, ϕ, ψ	Euler angles
Ω	Angular velocity of propellers

CHAPTER 1

INTRODUCTION

Aerial vehicles are broadly used in the military (surveillance, war, shipment, inspection) and civilian areas in (mapping, search and rescue, transporting people and goods) many applications. Unmanned air vehicles have become popular in the 21^{st} century with the improvements in modelling, simulation, control theories, and manufacturing. Air vehicles can be investigated in two groups, such as rotary and fixed wing air vehicles corresponding to their wing types [1–3]. Orville and Wilbur Wright (also known as Wright Brothers) developed the first heavier than air machine named as Wright Flyer in 1903 [4] given in Figure 1.1a. Igor Sikorsky developed the first rotary wing air vehicle named as VS-300 in 1939 [5] depicted in Figure 1.1b. Fixed and rotary wing air vehicles can be investigated in different categories which are given in Figures 1.2 [6] and 1.3 [7], respectively.

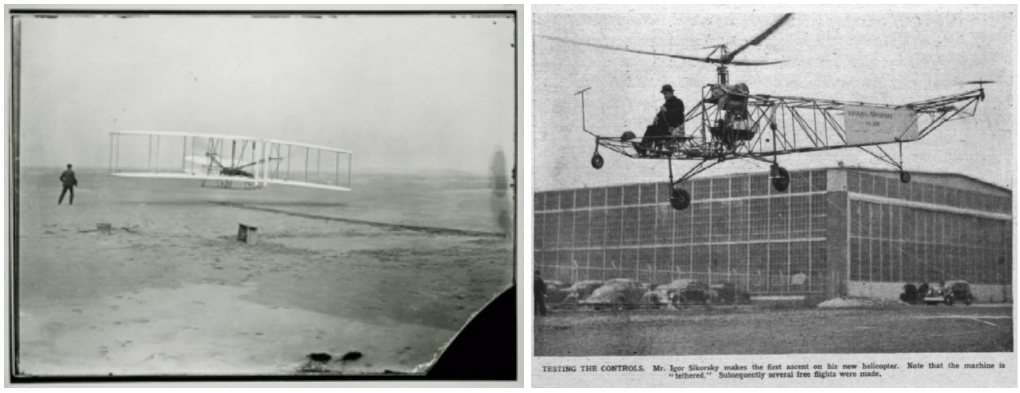

(a) Wright Flyer [4] (b) VS-300 [5]

Figure 1.1: First fixed and rotary wing air vehicles

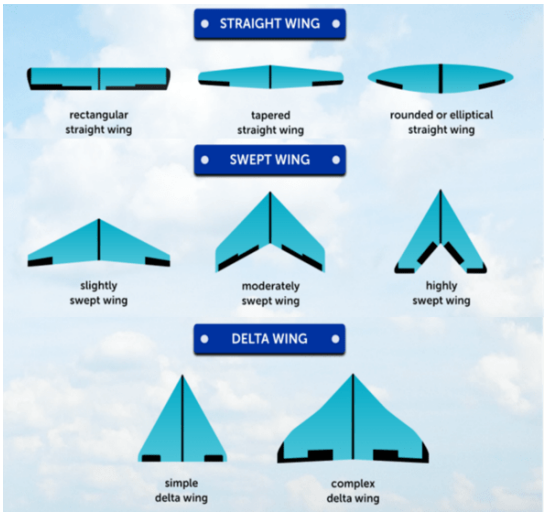

Figure 1.2: Fixed wing types [6]

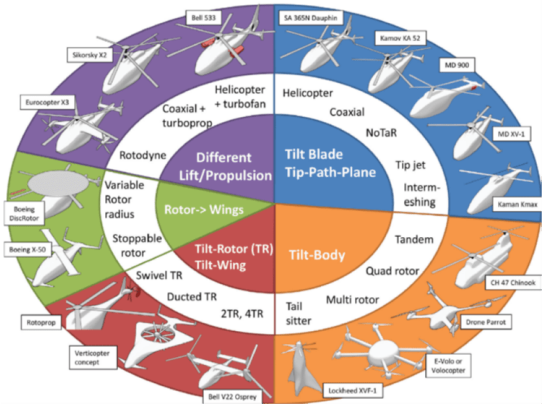

Figure 1.3: Rotary wing types [7]

1.1 Motivation and Problem Definition

Fixed and rotary wing air vehicles have advantages and disadvantages compared to each other. Rotary wing air vehicles hover in the air so they can be used for applications in small area missions. They can take-off and land vertically, so there is no need for a runway. On the other hand, all actuators like brushless DC motors and propellers must rotate during the flight, which is a disadvantage of rotary wing air vehicles in the sense of energy consumption. Besides, their electrical structure is more complex. Fixed wing air vehicles have long endurance, higher speed, longer

flight time, affordable (lower fuel bills), lower maintenance, greater stability and linear flight advantage. However, they cannot make hover and slow speed flights. They need a runway for take-off and landing [8, 9]. To dispose of these drawbacks and combining the upsides of these two sort air vehicles, a fixed wing VTOL UAV idea is advertised [10–12].

Pros and cons of the air vehicle types are given in Table 1.1 [13]. With taking into account both advantages and disadvantages of fixed and rotary wing air vehicles, it is aimed to compensate for the deficiencies of air vehicles by combining them in one platform. Fixed wing VTOL air vehicles are made by adding the ability of hover and vertical take-off and landing to the fixed wing air vehicles.

Table 1.1: Pros and Cons of Air Vehicles

Ability	Platform Types		
(+:good, o:neutral, -:bad)	Rotary wing	Fixed wing	Fixed wing VTOL
Energy efficiency	-	+	+
Range	-	+	+
Endurance	-	+	+
Hover	+	-	+
Complexity	+	-	o
Manoeuvrability	+	-	+
VTOL	+	-	+

Air vehicles are appropriately used for the mission type. For example, if precise motions or hovering are required, and there is a small area to take-off and land, then rotary wing air vehicles are used. However, if the requirements are extensive range, high payload, and endurance, then fixed wing air vehicles are preferred. The advantages of rotary and fixed wing air vehicles are merged in fixed wing VTOL air vehicles. Endurance and range of the fixed wing VTOL air vehicle cannot be as high as a fixed wing air vehicle. Similarly, it cannot hover as long as a rotary wing air vehicle. Although there are some inefficiencies of the fixed wing VTOL air vehicles compared to the fixed wing and rotary wing ones, it solves many problems.

1.2 Literature Review

Unconventional air vehicles are developed with the improvements on mechanical, electronic, and software industries. Innovations on the metallurgical and material technology provide an opportunity for lighter and more robust parts. Besides, it is easier to shape them that open new windows for designers [14, 15]. One of the essential components is controller hardware that runs algorithms during the operation of air vehicles. Compared to the old personal computers, cards' technical properties are much higher in the sense of processor, memory, compactness, interfaces, such a pitch that some commercial off-the-shelf ready to fly **autopilot cards** are available on the market. These cards can even be configurable to different platforms. Some famous commercial off-the-shelf ready to fly autopilot cards are Dronee Cockpit [16], Navio2 [17], BeagleBone Blue [18], MicroPilot [19], Pixhawk Cube Flight Controller [20] and so on. In this research, the Pixhawk Cube controller board is used. The reason why the Pixhawk Cube is chosen and detailed information is given in Section 2.1.1.

Complex and high load algorithms can be run on with the new age microprocessor and electronic cards. **Autopilot algorithms** are developed to help pilots during all flight phases, such as take-off, cruise, and landing. The algorithms also reject disturbances such as wind and gust. This need implies some controller and disturbance rejection algorithms such as PID, LQR, sliding mode control, back-stepping, feedback linearization, adaptive control, robust control, optimal control, active disturbance rejection controller (ADRC), L_1, H_∞, fuzzy logic, artificial neural networks, and so on [21–23]. PID controller has a wide range of applications and is widely used in the industry. Crucial advantages of this controller are that gains can be adjusted quickly. Design of the controller is simple, and robustness is good. The mathematical model of this controller is insufficient but straightforward because some system dynamics are unmodelled or inaccurate modelling [24, 25]. Performance of the PID controller is limited due to the uncertainties. Another controller type is sliding mode control (SMC) which is nonlinear. In this method, a discontinuous signal is applied to the system to slide along a predetermined path. System dynamics are not simplified by making linearization in the sliding mode control whose tracking performance is

good [21, 26]. The back-stepping control algorithm is a kind of recursive method. The primary advantage of this method is the fast convergence. Disturbances can be handled well. Nevertheless, the robustness of this method is not good [27]. Feedback linearization converts the nonlinear system to the linear system by making a change of variables. The major limitation of this method is a precision loss because of linearity. This method requires an exact model for implementation but has an excellent tracking ability. However, its disturbance rejection ability is poor [21, 26]. There are also some intelligent control algorithms which are fuzzy logic, neural networks, machine learning and genetic algorithms. There are pretty much uncertainty and mathematical complexity in these algorithms. Because of this complexity, they have substantial computational budgets [26].

In many applications [21–32], physical systems are modelled in the computer environment experimentally to get results as close as possible to the actual system. However, it is a harsh and inefficient way to model all system dynamics. Another disadvantage to model every part of the system is that even a minor change must be modelled in a computer environment that may be expensive and time-consuming. Discrepancies occur among simulation and system output. To get rid of the exact modelling need and observing uncertainties, ADRC can be used. Active Disturbance Rejection Control (**ADRC**) is a well-known controller and proposed by Han [33]. ADRC is composed of a tracking differentiator, a PD controller, and an Extended State Observer (ESO). ADRC is applied to a wide range of military and civil applications [34–37]. Effects of uncertainties, disturbances, and unmodelled dynamics to the system are estimated [38]. Detailed information about design and implementation of ADRC are given in Section 5.2. Thanks to the advances in that are stated above, unconventional air vehicles are developed. **Fixed wing VTOL air vehicles** become popular and it has various types according to the orientation and motion of its actuators. Tilt rotors, quadrotor-fixed wings, tail sitters, ducted fans-fixed wings are some types of fixed wing VTOL air vehicles. Researchers focus on performance and efficiency of air vehicles related to different geometries, algorithms, and configurations. Besides the research area, lots of feasible solutions are found with using fixed wing VTOL air vehicles. Search and rescue, photometry, mapping, surveillance, transportation, and combat are some areas that fixed wing VTOL air vehicles are used.

Examples of the fixed wing VTOL air vehicle types are given in Table 1.2.

Table 1.2: Fixed wing VTOL air vehicle examples

Picture	Air vehicle name	Type
	UGS-TUM [39]	Tiltrotor - fixed wing
	M1-M4 [40]	Tiltrotor - fixed wing
	Twin engine flying wing [41]	Tail sitter - fixed wing
	Leha [42]	Quadrotor - fixed wing
	Hybrid UAV [43]	Quadrotor - fixed wing
	Arcturus T-20 [44] (Commercial)	Quadrotor - delta wing
	Ascent, Transition, Reach [45] (Commercial)	Quadrotor - fixed wing
	CGT50 [46] (Commercial)	Quadrotor - fixed wing

1.3 Proposed Methods and Models

A fixed air vehicle is modified such that vertical take-off and landing skills are built, so a fixed wing VTOL air vehicle is obtained. Since the final platform is a combination of a rotary wing and a fixed wing air vehicle, each platform is investigated individually.

- A **rotary wing air vehicle** is modelled in a computer environment with identification of mass moment of inertias and thrust units, experimentally.
- 2^{nd} and 3^{rd} order ADRC controllers are designed and applied to the rotary wing air vehicle model to control *translational and rotational dynamics*.
- Outdoor flight tests are carried out for 20m. and 40m. flight ranges with 2^{nd} and 3^{rd} order ADRC controllers under different load conditions such as unloaded, asymmetrically loaded stationary and slung load cases.
- A **fixed wing air vehicle** is modelled in a computer environment with identification of mass moment of inertias, thrust units, and control surfaces, experimentally.
- PID controller is designed and applied to the fixed wing air vehicle model to control translational and rotational dynamics.
- Outdoor flight tests are carried out with fixed wing air vehicle.
- A **fixed wing VTOL air vehicle** is modelled in a computer environment with identification of mass moment of inertias, thrust units, and control surfaces, experimentally.
- 2^{nd} and 3^{rd} order ADRC controllers are designed and applied to the fixed wing VTOL air vehicle model to control translational and rotational dynamics.
- **Control allocation** algorithms are investigated to distribute required forces and moments to the available set of actuators during different flight phases.
- Designed controllers and control allocation algorithm are merged in an operational scenario.

1.4 Contributions and Novelties

Our contributions are as follows:

- A method is developed for designing an autopilot and guidance algorithms which can stand for flights under different loads and disturbances. The rotary wing air vehicle is modelled experimentally. Dynamics and disturbances, which are hard to model, are estimated to be rejected during the flight test with the same controller and observer gains.

- Different control allocation algorithms are designed and applied to tilt-rotor and tail-sitter type air vehicles. Energy-efficient control allocation algorithm is investigated for fixed wing VTOL type air vehicles.

- Performance of the Active Disturbance Rejection Controller is increased with taking into account the actuator dynamics which gives freedom to increase the controller and observer bandwidths that output better controller and estimation performances,
  and, in addition to the [38];

- Performance of the ADRC is investigated and proved under disturbances that are changing stochastically in magnitude and direction caused by an asymmetric placed slung load besides gust and wind.

- Performance of the trajectory tracking and attitude control of the rotary wing air vehicle is improved with enhanced ADRC structure.

- An optimization is done for energy consumption without waiving the performance of the controllers.

- Contributions are proved by the outdoor flight tests with unloaded, asymmetrically located static loaded, and slung loaded cases for the rotary wing air vehicle.

- An energy optimized guidance, autopilot, and control algorithm is developed for fixed wing VTOL air vehicle.

1.5 The Outline of the Thesis

Current technologies, algorithms, and improvements about rotary, fixed, and fixed wing VTOL air vehicles are given in Section 1. Detailed information about physical properties, analysis and experiments done during the modelling of the rotary wing, fixed wing, and fixed wing VTOL air vehicles are given in Sections 2, 3, and 4, respectively. Designed control algorithms to control the translational-rotational states and control allocation algorithms to distribute the desired forces/moments to an available set of actuators are given in Section 5. Obtained results during the simulations and flight tests are given and discussed in Section 6. The research is concluded with Section 7 containing the contributions and discussions.

CHAPTER 2

ROTARY WING AIR VEHICLE

The rotary wing air vehicle is used to develop controllers for vertical motion that will be done in take-off and landing stages. In this chapter, information about the rotary wing air vehicle, system identification tests, and mathematical modelling are stated. Developed guidance and autopilot algorithms are deployed to a controller board. Some **important** steps about deployment and related to the operation are also given in the chapter.

2.1 Physical System

As a rotary wing air vehicle, low cost and off-the-shelf products are chosen. Components of the rotary wing air vehicle are given in Table 2.1. Assembled rotary wing air vehicle is given in Figure 2.1.

Table 2.1: Components of the rotary wing air vehicle

Property	**Description**
Frame	Tarot F450
Electronic Speed Controllers	Skywalker ESC 30A
Propellers	8x4.5 (CW-CCW)
Controller board	Pixhawk Cube
Battery	11.1V - 3200mAh
Brushless Direct Current Motors	Emax XA2212 980KV
Total weight	$\approx$1kg

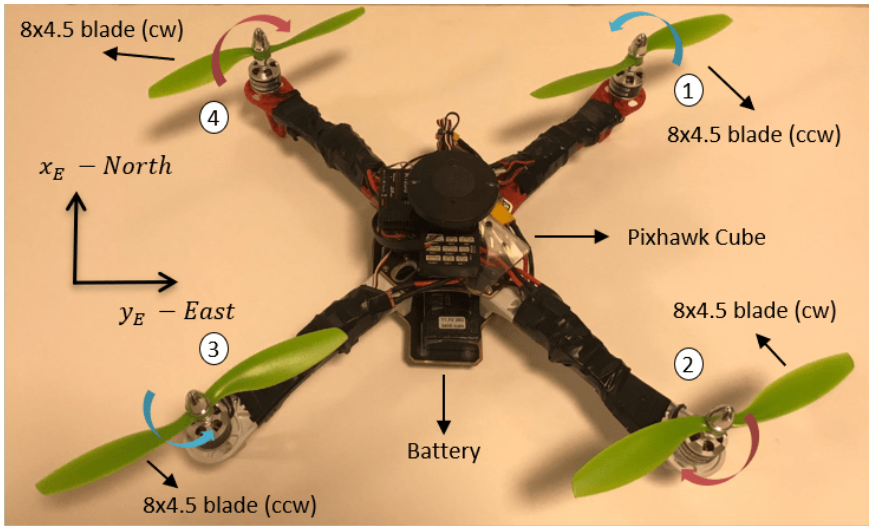

Figure 2.1: Assembled rotary wing air vehicle

2.1.1 Controller board

Pixhawk Cube controller board is a well-known autopilot board [47,48], which is used to control for the different ground and air vehicles. It has analogue and digital input ports to acquire data from different sensors or remote controllers and output ports to use actuators such as servo motors and brushless direct current (BLDC) motors. There are built-in gyroscopes, accelerometers, magnetometers, and barometers. Latitude, longitude, and altitude of the rotary wing air vehicle are obtained with the Global Positioning System (GPS) module of the Pixhawk Cube controller board.

In this study, the built-in firmware is **erased**, and the developed guidance and autopilot algorithms are **deployed** into the cube controller. Matlab®/Simulink®environment is used to develop the guidance and autopilot algorithm. Matlab®(2018b) converts the developed algorithm from the Simulink environment to a C code using the hardware support package for Pixhawk Cube. Then, the algorithm runs in the Pixhawk Cube controller board in real-time. In this study, the sampling frequency is set to 250 Hz. Vehicle attitude, GPS global/local coordinates, remote control sources of info and battery voltage/current data can be acquired by using the Pixhawk Cube controller board library. PWM ports can be controlled with the same library too.

Ready to fly firmware for rotary wing air vehicle can be downloaded and deployed to Pixhawk Cube controller board using either Mission Planner [49] or QGroundControl [50] software. **In this research, not ready to fly firmware is used. Guidance and autopilot algorithms are developed and deployed to the Pixhawk Cube control board. So, just sensors, processor, inputs, and outputs of the board are used.** Some issues mentioned in remarks below are encountered with Pixhawk Cube controller board in Matlab®/Simulink®. These issues may not be seen in ready to fly firmware.

Remark 1: After the code is deployed to the Pixhawk Cube controller board, the measured and estimated Euler angles are not constant. Angles are settled after at least 60 seconds.

Remark 2: Although the Pixhawk Cube controller board is on a horizontal surface, roll and pitch angles are not zero. There is always drift in angle measurements due to the sensor bias. Therefore, these angles must be reset to zero. In our application, one channel from the remote controller is dedicated to resetting the angles to zero.

The issues that are stated in *Remark 1* and *Remark 2* can be seen in Figure 2.2. Arrow represents the time of the reset.

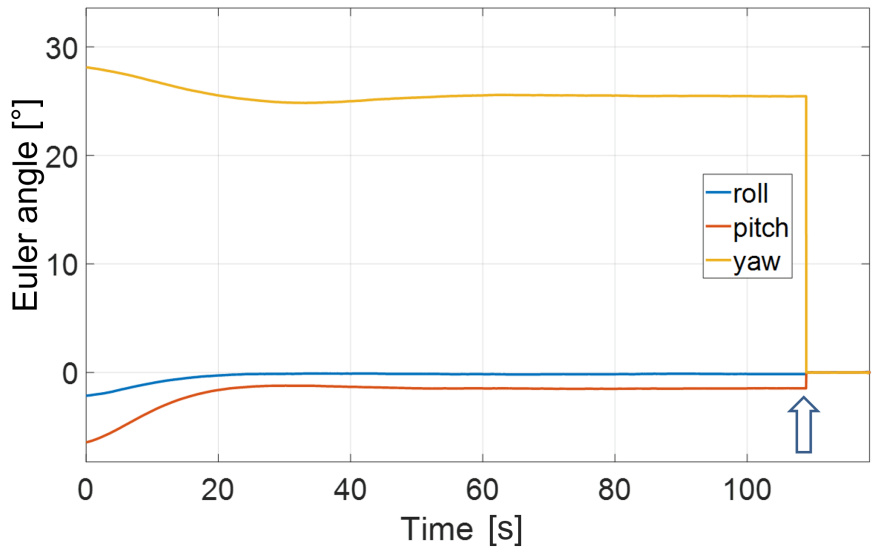

Figure 2.2: Pixhawk Cube measured Euler angles

Remark 3: Pixhawk Cube controller board has an SD card that is used for logging the telemetry data during the flight tests. In Figure 2.3, a sample timestamp difference data can be seen. Usually, Pixhawk Cube controller board is set to run at $4ms$ ($250Hz$) period. The timestamp is the time measured by the processor of the controller board at each cycle. Timestamp difference of the board can be seen in Figure 2.3. Till about second 86, except a little jump at about second 40 which is shown with the solid line arrow timestamp difference is $4ms$. At about second 86, the timestamp difference is about $200ms$ depicted with a dashed line arrow. It means that no sensor data is acquired from the board during $200ms$, which makes the rotary wing air vehicle unstable. This problem is solved after changing the SD card which comes with the Pixhawk Cube controller board with a SanDisk Extreme U3 32GB [51].

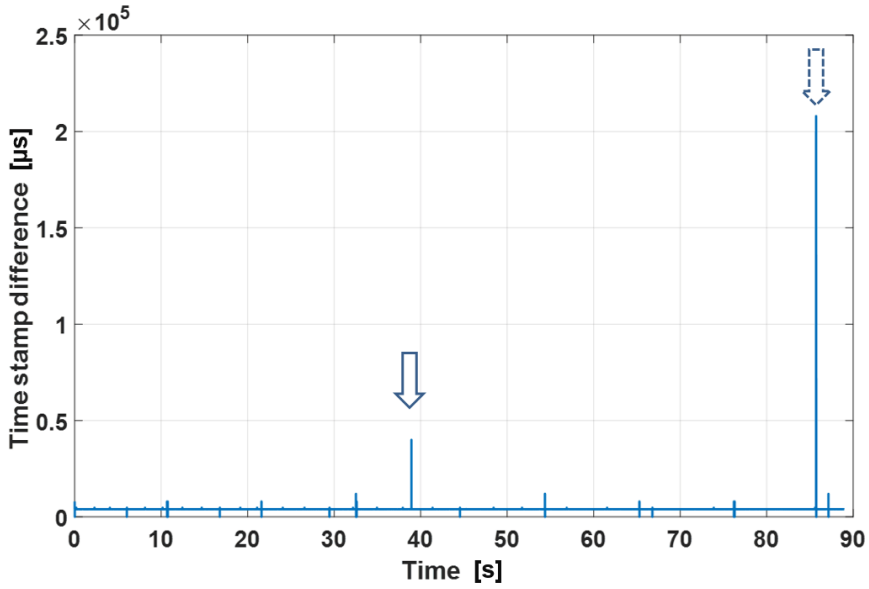

Figure 2.3: Pixhawk Cube data loss

2.1.2 Thrust unit

Thrust unit is composed of an electronic speed controller, a brushless DC motor, and a propeller. The rotary wing air vehicle has four thrust units. Pixhawk Cube controller board gives output signals that are determined by the guidance and control algorithms run in the board. The control signal is a pulse-width-modulation (PWM) signal. The electronic speed controller converts the PWM signal into three phase-

shifted sinus signals. The rotational velocity of the brushless DC motor and propeller pair is adjusted by the sinus signal. The process is depicted in Figure 2.4.

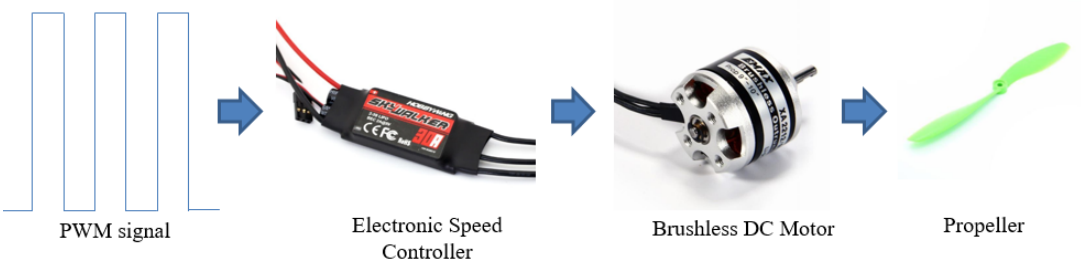

Figure 2.4: Thrust unit

2.2 System Identification

Experimental identification tests have been carried out to have a mathematical model of the rotary wing air vehicle as close as possible to the real system. Reducing the discrepancy among the real system and the system model gives closer results among them.

2.2.1 Bifilar pendulum test for rotary wing air vehicle

Bifilar pendulum test is an innovative way to obtain the mass moments of inertia of an object [52, 53]. In this study, the bifilar pendulum test is performed to rotary wing air vehicle to get its mass moments of inertia around roll, pitch, and yaw axes that are given in Figure 2.5. In these tests, the air vehicle is hanged and oscillated freely around its roll, pitch, and yaw axes. During its oscillation, angular rates are acquired with the Pixhawk Cube autopilot card. Test parameters, which are summarized in Table 2.2, are substituted in Equation 2.1 and the mass moment of inertia for roll, pitch, and yaw axes are found experimentally.

The rotary wing air vehicle is symmetric around the roll and pitch axes, so it is assumed that the mass moment of inertia values around the roll and pitch axes are equal or very close to each other. Oscillation data for roll and yaw axes can be found in Figures 2.6a and 2.6b, respectively.

Table 2.2: Parameters of bifilar pendulum test

Property	**unit**	**roll and pitch axes**	**yaw axis**
Length of the ropes, ℓ	m	0.46	0.46
Distance between ropes, R	m	0.31	0.31
Mass of the system, m	kg	1	1
Gravitational acceleration, g	m/sec^2	9.81	9.81
Oscillation period, T_n	s	1.04	1.52

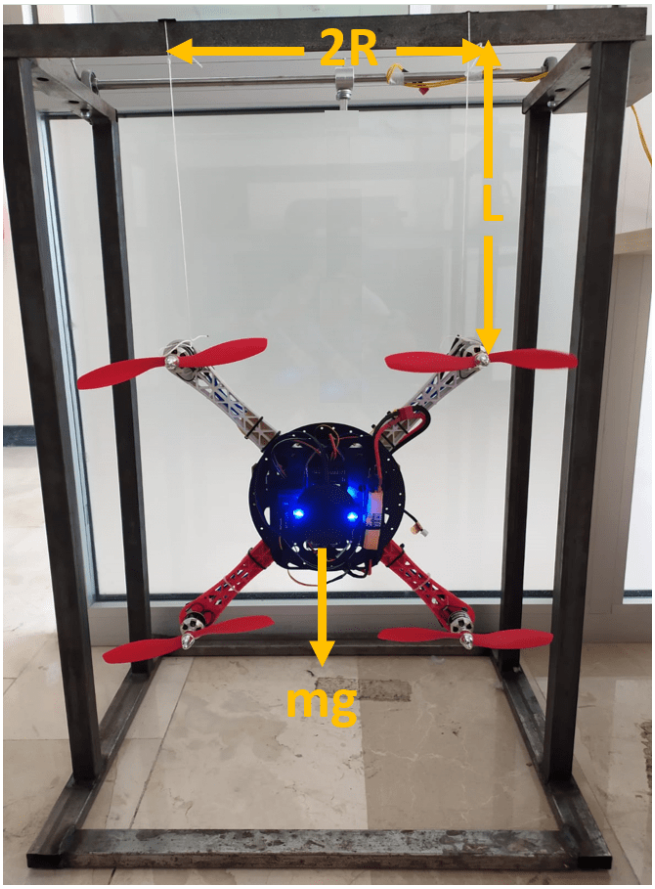

Figure 2.5: Bifilar pendulum experiment

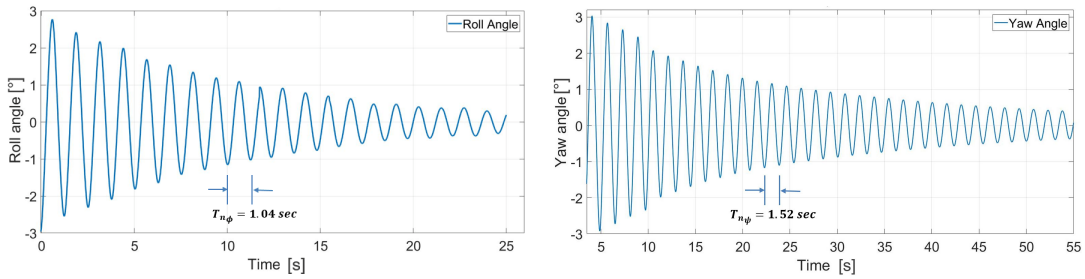

(a) Roll axis

(b) Yaw axis

Figure 2.6: Bifilar pendulum experiment of the rotary wing air vehicle for $roll$ and yaw axes

$$I = \left[\frac{T_n}{2\pi}\right]^2 \frac{mgR^2}{\ell} \tag{2.1}$$

After substituting the parameters, which are given in Table 2.2, in Equation 2.1, mass moment of inertias of the rotary wing air vehicle around three body axes are found and given in Table 2.3 and Equation 2.2.

Table 2.3: Mass moment of inertias of the rotary wing air vehicle

Property	**unit**	**inertia value**
Inertia around x-body axis, I_x	kg.m^2	0.1402
Inertia around y-body axis, I_y	kg.m^2	0.1402
Inertia around z-body axis, I_z	kg.m^2	0.3267

$$\mathbf{I} = \begin{bmatrix} I_x & 0 & 0 \\ 0 & I_y & 0 \\ 0 & 0 & I_z \end{bmatrix} = \begin{bmatrix} 0.1402 & 0 & 0 \\ 0 & 0.1402 & 0 \\ 0 & 0 & 0.3267 \end{bmatrix} \tag{2.2}$$

2.2.2 Thrust measurement for rotary wing air vehicle

The thrust test is an innovative way to identify the thrust force, which is produced by the motor and propeller pair. Each BLDC (brushless direct current) motor has to

be tested with a propeller and an electronic speed controller (ESC) in their direction of rotation, particularly. Different BLDC motors do not rotate at the same rotational velocity for the same PWM input signal even if they are the same brand. In this study, components which are used to generate thrust force are named as a thrust unit that is composed of an ESC, a BLDC, and a propeller. Thrust units that are used in rotary wing air vehicle are tested in a thrust measurement setup. The scheme is represented in Figure 2.7. During the experiment, reference PWM signals are sent to the ESCs which are used to convert PWM signals to three sinusoidal signals and motor-propeller pair rotates. The rotational velocity of the motor-propeller pair is directly proportional with the duty ratio of the PWM signal. Generated thrust force and drag moment are measured by a six axes force and torque sensor. Besides, the rotational velocity of the motor-propeller pair is measured by an infrared sensor.

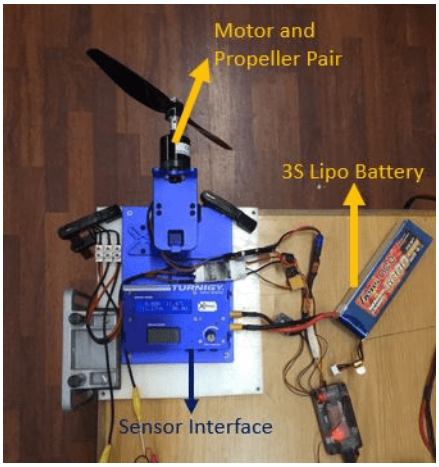

Figure 2.7: Thrust measurement setup

The thrust test is carried out for each thrust unit to get the transfer function of the actuators. Stair step-shaped input reference PWM signal is sent to the thrust unit. Generated thrust force is logged using a force sensor. Measured thrust force and rotational velocities of each thrust unit are given in Figures 2.8 and 2.9, respectively.

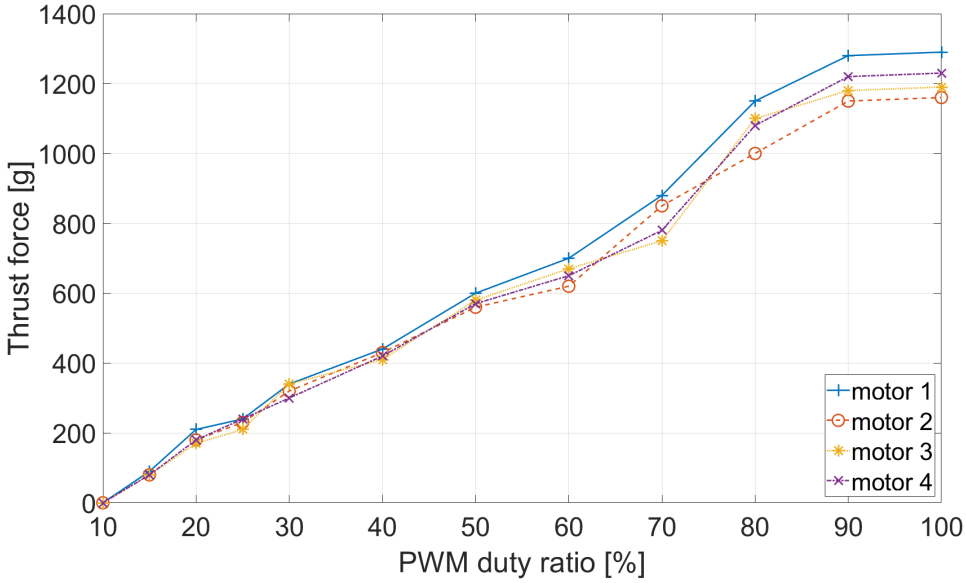

Figure 2.8: Measured thrust forces

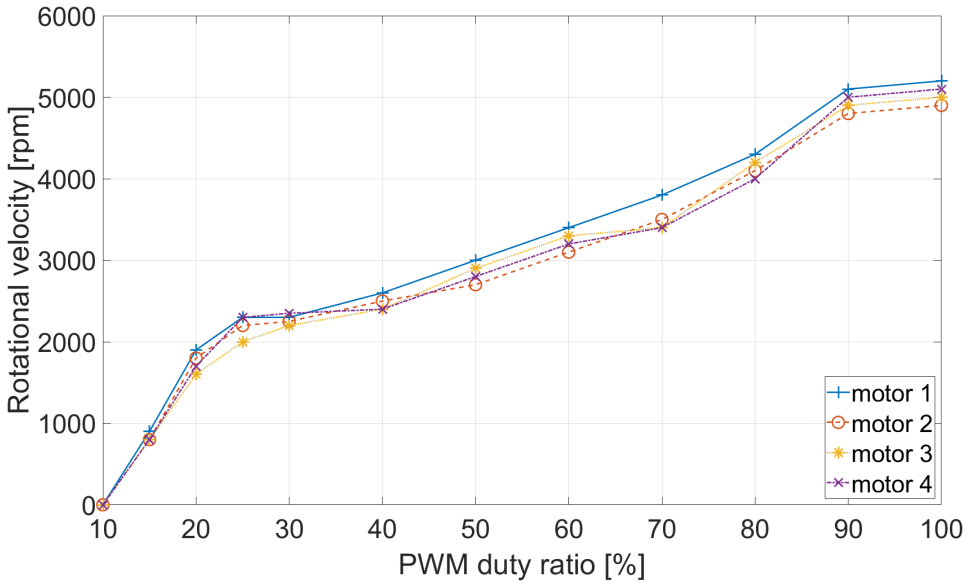

Figure 2.9: Measured rotational velocities

Obtained transfer functions using the input and output signals for each thrust unit are given in Table 2.4. In transfer function, $V(s)$ is the input and $\Omega(s)$ is the output which is reference voltage signals and rotational speed of the motors, respectively.

Table 2.4: BLDCs transfer functions

Transfer Function	Motor 1	Motor 2	Motor 3	Motor 4
$\frac{\Omega(s)}{V(s)}$	$\frac{0.98}{0.0625s+1}$	$\frac{0.975}{0.0622s+1}$	$\frac{0.983}{0.0626s+1}$	$\frac{0.91}{0.0627s+1}$

2.3 Mathematical Modelling of the Rotary Wing Air Vehicle

Scheme of the rotary wing air vehicle, which is used in this study is given in Figure 2.10. Each brushless DC motor and propeller has a contribution in rotational and translational dynamics in the X shaped rotary wing air vehicle. Propeller directions of rotations are depicted as green and red curved arrows. Rotary wing air vehicle is stationary if thrust units generate equal thrust forces, which are shown as $\mathbf{F_i}$ where $i = 1, 2, 3, 4$. The thrust forces are obtained with the rotational speed of propellers, which are represented by $\mathbf{\Omega_i}$ where $i = 1, 2, 3, 4$. Rotary wing air vehicle rotates and translates because of the moments and forces generated by the thrust units. Rotational motion around the body x, y, and z axes are named as $roll, pitch$, and yaw and symbolized as ϕ, θ, and ψ, respectively.

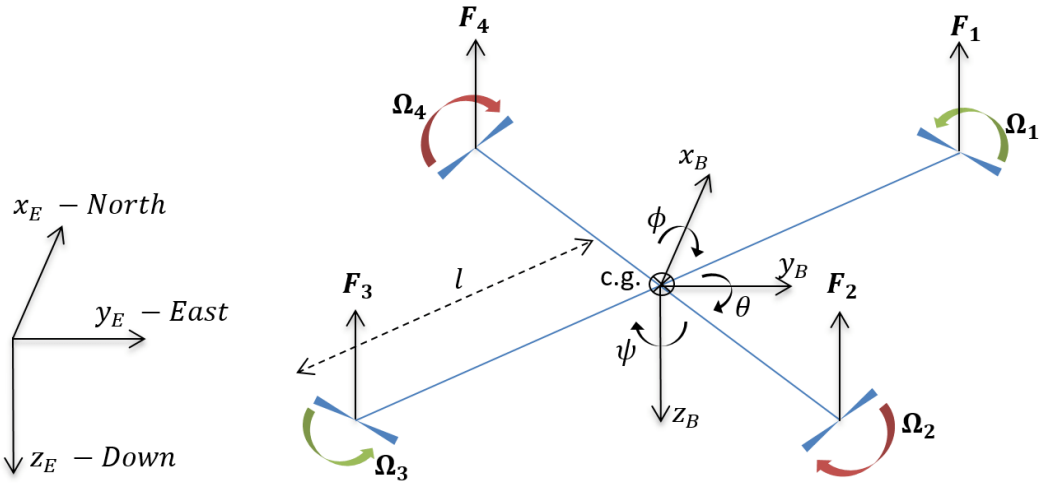

Figure 2.10: Rotary wing air vehicle scheme

To have a positive roll moment, the generated aerodynamic moments from the third and the fourth propellers must be higher than the first and the second ones. Similarly, to have a positive pitch moment generated aerodynamic moments from the first and the fourth propellers must be higher than the second and the third ones. The yaw dynamic of the rotary wing air vehicle is controlled by the drag moments which are generated by propeller rotations. Each propeller generates a drag moment to the opposite direction of rotation [54, 55]. Thrust force and aerodynamic moments which are generated with the thrust units are calculated as given in Equation 2.3.

$$\begin{aligned}
\mathbf{U}_1 &= \sum_{i=1}^{4} \mathbf{F}_i = b_1 {\mathbf{\Omega_1}}^2 + b_2 {\mathbf{\Omega_2}}^2 + b_3 {\mathbf{\Omega_3}}^2 + b_4 {\mathbf{\Omega_4}}^2 \\
\mathbf{U}_2 &= l\left(b_3 {\mathbf{\Omega_3}}^2 + b_4 {\mathbf{\Omega_4}}^2 - b_1 {\mathbf{\Omega_1}}^2 - b_2 {\mathbf{\Omega_2}}^2\right) \\
\mathbf{U}_3 &= l\left(b_2 {\mathbf{\Omega_2}}^2 + b_3 {\mathbf{\Omega_3}}^2 - b_1 {\mathbf{\Omega_1}}^2 - b_4 {\mathbf{\Omega_4}}^2\right) \\
\mathbf{U}_4 &= d_1 {\mathbf{\Omega_1}}^2 - d_2 {\mathbf{\Omega_2}}^2 + d_3 {\mathbf{\Omega_3}}^2 - d_4 {\mathbf{\Omega_4}}^2
\end{aligned} \tag{2.3}$$

where:

U_1 : Generated lift force
U_2 : Roll moment
U_3 : Pitch moment
U_4 : Yaw moment
$\Omega_{1,2,3,4}$: Rotational velocity of the rotary wings
l : Distance of rotary axes and center of gravity of the rotary wing air vehicle
$b_{1,2,3,4}$: Thrust coefficient of thrust units
$d_{1,2,3,4}$: Drag coefficient of thrust units

Translational and rotational equations of motion in body-fixed frame for the rotary wing air vehicle are given in Equations 2.4 and 2.5. External forces acting on the rotary wing air vehicle are composed of gravitational, propulsive, and aerodynamic forces. Since the translational velocities of the rotary wing air vehicle are low, aero-

dynamic forces are neglected [56].

$$
\begin{aligned}
\sum \mathbf{F}_{ext} &= \mathbf{F}_{grav,B} + \mathbf{F}_{prop,B} \\
\mathbf{F}_{grav,B} &= \mathbf{L_{BE}} m \begin{bmatrix} 0 \\ 0 \\ g \end{bmatrix} \\
\mathbf{F}_{prop,B} &= - \begin{bmatrix} 0 \\ 0 \\ U_1 \end{bmatrix} \\
\sum \mathbf{F}_{ext} &= \mathbf{L_{BE}} m \begin{bmatrix} 0 \\ 0 \\ g \end{bmatrix} - \begin{bmatrix} 0 \\ 0 \\ U_1 \end{bmatrix} \\
\begin{bmatrix} \ddot{x} \\ \ddot{y} \\ \ddot{z} \end{bmatrix} &= \begin{bmatrix} 0 \\ 0 \\ g \end{bmatrix} - \mathbf{L_{EB}} \begin{bmatrix} 0 \\ U_1/m \end{bmatrix}
\end{aligned}
\tag{2.4}
$$

$$
\sum \mathbf{M}_{ext} = \begin{bmatrix} U_2 \\ U_3 \\ U_4 \end{bmatrix} \tag{2.5}
$$

where L_{BE} is the transformation matrix converting F_E (force defined in the Earth-fixed frame) to F_B (force defined in the body-fixed frame).

$$
\mathbf{L_{BE}} = \begin{bmatrix} c(\theta)c(\psi) & c(\theta)s(\psi) & -s(\theta) \\ s(\phi)s(\theta)c(\psi) - c(\phi)s(\psi) & s(\phi)s(\theta)s(\psi) + c(\phi)c(\psi) & s(\phi)c(\theta) \\ c(\phi)s(\theta)c(\psi) + s(\phi)s(\psi) & c(\phi)s(\theta)s(\psi) - s(\phi)c(\psi) & c(\phi)c(\theta) \end{bmatrix} \tag{2.6}
$$

where:

c : cosine function

s : sine function

Moreover, all the transformation matrices are orthogonal, then L_{BE} transformation matrix converting F_E to F_B can be expressed as in Equation 2.7.

$$\mathbf{L_{EB}} = \mathbf{L_{BE}}^{-1} = \mathbf{L_{BE}}^{T} \tag{2.7}$$

Since there are four inputs and six outputs, the rotary wing air vehicle is underactuated. Inputs are the rotational velocities of the thrust units and outputs are translational and rotational dynamics of the rotary wing air vehicle. Translational and rotational equations are driven by Newton-Euler equations given in Equations 2.8, 2.9 and 2.10.

$$\begin{aligned} \sum \mathbf{F}_{ext} &= m_B \ddot{\mathbf{x}}_B \\ \sum \mathbf{M}_{ext} &= \mathbf{I_B}\dot{\boldsymbol{\omega}}_B + \boldsymbol{\omega}_B \times \mathbf{I_B}\boldsymbol{\omega}_B \end{aligned} \tag{2.8}$$

$$\begin{aligned} \ddot{x} &= (\sin\psi \sin\phi + \cos\psi \sin\theta \cos\phi)\frac{U_1}{m} \\ \ddot{y} &= (-\cos\psi \sin\phi + \sin\psi \sin\theta \cos\phi)\frac{U_1}{m} \\ \ddot{z} &= -g + (\cos\theta \cos\phi)\frac{U_1}{m} \end{aligned} \tag{2.9}$$

$$\begin{aligned} \dot{p} &= \frac{I_y - I_z}{I_x} qr + \frac{U_2}{I_x} \\ \dot{q} &= \frac{I_z - I_x}{I_y} pr + \frac{U_3}{I_y} \\ \dot{r} &= \frac{I_x - I_y}{I_z} pq + \frac{U_4}{I_z} \end{aligned} \tag{2.10}$$

In Equations 2.9 and 2.10, m is the mass, x, y, z and p, q, r are the translational position and angular velocity of the rotary wing air vehicle. ϕ, θ, and ψ represent the Euler angles, I_x, I_y, and I_z are the mass moment of inertia about x, y, and z axes. To simplify the system, the attitude dynamics of the rotary wing air vehicle in roll, pitch, and yaw axes can be written as in Equations 2.11 and 2.12 where U_2, U_3, and U_4 are

the roll, pitch, and yaw moments, respectively [38].

$$\begin{aligned} I_x\ddot{\boldsymbol{\phi}} &= \mathbf{U}_2 \\ I_y\ddot{\boldsymbol{\theta}} &= \mathbf{U}_3 \\ I_z\ddot{\boldsymbol{\psi}} &= \mathbf{U}_4 \end{aligned} \tag{2.11}$$

$$\begin{aligned} \frac{\phi(s)}{U_2(s)} &= \frac{1}{I_x s^2} \\ \frac{\theta(s)}{U_3(s)} &= \frac{1}{I_y s^2} \\ \frac{\psi(s)}{U_4(s)} &= \frac{1}{I_z s^2} \end{aligned} \tag{2.12}$$

CHAPTER 3

FIXED WING AIR VEHICLE

The fixed wing air vehicle is used to develop controllers for horizontal motion that will be done level flight and manoeuvrers. In this chapter, information about the fixed wing air vehicle, system identification tests, and mathematical modelling are stated. Developed guidance and autopilot algorithms are deployed to the Pixhawk Cube controller board (see Section 2.1.1).

3.1 Physical System

As a fixed wing air vehicle, an E-flite Apprentice model plane is used which is depicted in Figure 3.1. The plane comes with its safe controller. In the study's scope, the built-in controller is removed, and the Pixhawk Cube controller board is used to control the fixed wing air vehicle. Guidance and control algorithms are developed in Matlab/Simulink environment and deployed to the Pixhawk Cube controller board (see Section 2.1.1). Specifications of the fixed wing air vehicle are given in Table 3.1.

3.2 System Identification

3.2.1 Bifilar pendulum test for fixed wing air vehicle

Mass moment of inertia of the fixed wing air vehicle is found with the same method as done in Section 2.2.1. The experiment is done for all rotation axes which are roll, pitch, and yaw. Calculated mass moment of inertia values are given in Table 3.2.

Figure 3.1: Fixed wing air vehicle

Table 3.1: Specifications of the fixed wing air vehicle

Property	Value
Wing span	$1.5m$
Overall length	$1.08m$
Wing area	$33.2dm^2$
Motor size	$940Kv$
Battery	$3S$ $3200mAh$
Servos	4 $Savox$
Wing loading	$4.087kg/m^2$
Total weight	$1.4kg$

Table 3.2: Mass moment of inertias of the fixed wing air vehicle

Property	unit	inertia value
Inertia around x-body axis, I_x	kg.m^2	1.6589
Inertia around y-body axis, I_y	kg.m^2	1.5125
Inertia around z-body axis, I_z	kg.m^2	0.8124

3.2.2 Thrust measurement for fixed wing air vehicle

Horizontal thrust force of the fixed wing air vehicle is generated by a puller BLDC motor. Thrust measurement test is carried out with the same test bench (see Figure 2.7) to identify the generated thrust force relative to the PWM duty ratio. Relations obtained among PWM duty ratio and thrust force are given in Equations 3.1 and 3.2 which are implemented in Matlab®/Simulink®.

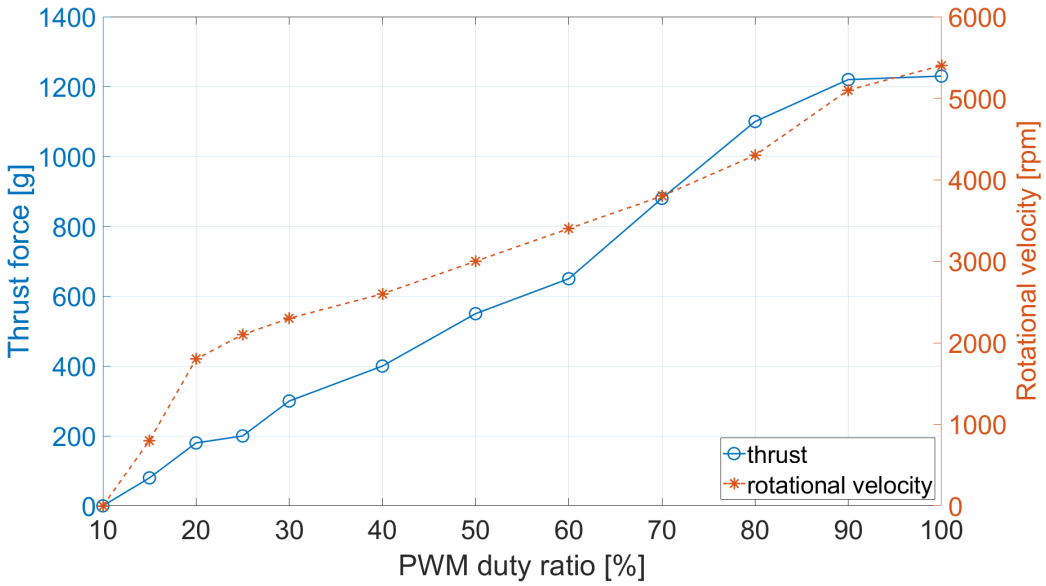

Figure 3.2: Thrust force and rotational velocity due to PWM duty ratio

$$F_x = -0.0017 \cdot dt^3 + 0.2993 \cdot dt^2 + 0.6369 \cdot dt + 2.7543 \tag{3.1}$$

$$\Omega_x = 0.0116 \cdot dt^3 - 2.0605 \cdot dt^2 + 155.5409 \cdot dt - 899.4160 \tag{3.2}$$

3.2.3 Control surface identification for fixed wing air vehicle

Control surfaces of the fixed wing air vehicle are actuated by servo motors. Each servo motor is connected to the angle measurement apparatus that is given in Figure 3.3. Relations are obtained among PWM duty ratio and control surface angles given in Table 3.3.

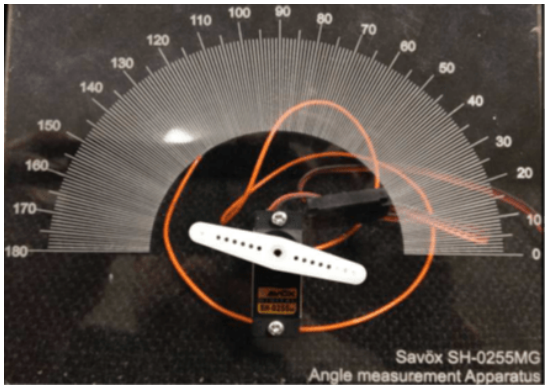

Figure 3.3: Angle measurement apparatus

Table 3.3: PWM signal and control surface position relations

Control surface	Position range [deg]	dt range (%)	Relation
Aileron	$\pm$28	0-100	cs_a=0.56.dt-28
Elevator	$\pm$22		cs_e=0.43.dt-22
Rudder	$\pm$15		cs_r=0.30.dt-15

In Table 3.3, rotational positions of control surfaces which are aileron, elevator, and rudder are represented as cs_a, cs_e, and cs_r, respectively. dt is the duty ratio of the PWM signal.

3.2.4 Aerodynamic analysis for fixed wing air vehicle

XFLR5 software [57] is used to analyse the fixed wing air vehicle aerodynamically. Airfoil is drawn to a graph paper, and coordinates are obtained. Airfoil coordinates are imported to XFLR5 software via a file whose extension is dat. Control surfaces on the main wing, horizontal, and vertical tails (ailerons, elevators, and rudder, respectively) are measured and implemented to the software. Then, flapped airfoils are created according to the percentage size of the control surfaces. Flapped airfoils are designed with $0°$ angle. The deflection is given during the stability analysis. A batch analysis is performed to investigate these airfoils. The analysis is made for a range of Re number (50.000-500.000) and angle of attack ($-7°$ to $10°$), and an incompress-

ible solution is selected for the results. After the design and analysis stages of the airfoils, the stage of the wing and plane design is started. When designing the main wing, horizontal and vertical tail, information of the span, span-wise chord, airfoil type, twist angle, and dihedral angle are needed. For the analysis, adding the body of the aircraft is not recommended. Therefore, the weight of the fuselage is given as a point mass. The weights of all electronics and motor are also given as point masses. Pressure distributions are shown in Figure 3.4a. changing of lift coefficient C_L and pitch moment coefficient C_M are given in Figure 3.4b and 3.4d, respectively. Relation among drag coefficient C_D and lift coefficient C_L is given in Figure 3.4c. All data are implemented in Matlab®/Simulink®and used during simulations.

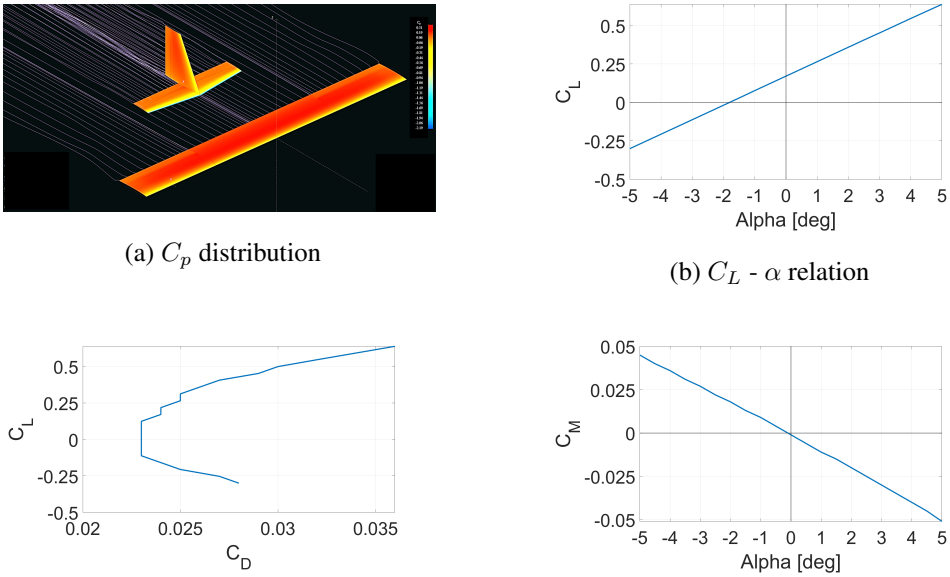

(a) C_p distribution

(b) C_L - α relation

(c) C_L - C_D relation

(d) C_M - α relation

Figure 3.4: Aerodynamic analysis of fixed wing air vehicle

Aerodynamic forces and moments generated by the control surfaces and wings are analysed. Forces in the x, y and z directions are obtained from their translational and rotational velocity derivatives which can be seen from the left columns of the Tables 3.5 and 3.6. Non-dimensional counterparts are obtained from the ratio of the dynamic pressure, q, times area, Equation 3.4. Pitching moment derivatives can be non-dimensionalized from the ratio of the dynamic pressure times area times mean aerodynamic chord, Equation 3.5. Rolling and yawing moment derivatives can be

non-dimensionalized from the ratio of the dynamic pressure times area times mean span, Equation 3.6. Aerodynamic and geometric properties of the fixed wing air vehicle are given in Table 3.4. Longitudinal and lateral stability derivatives are found by the aerodynamic analysis and given in right columns of Tables 3.5 and 3.6, respectively. Center of gravity of the fixed wing air vehicle is selected as a reference point during the XFLR5 software analyses.

$$q = 1/2 * \rho * V^2 \tag{3.3}$$

$$C_{X_{(u,a)}}, C_{Z_u}, C_{L_{(\alpha,q)}}, C_{Y_{(\beta,p,r)}} = \frac{X_{(u,w)}, Y_{(v,p,r)}, Z_{(u,w,q)}}{q * S} \tag{3.4}$$

$$C_{M_{(u,\alpha,q)}} = \frac{M_{(u,w,q)}}{q * S * \overline{c}} \tag{3.5}$$

$$C_{L_{(\beta,p,r)}}, C_{N_{(\beta,p)}} = \frac{L_{(v,p,r)}, N_{(v,p)}}{q * S * b} \tag{3.6}$$

Table 3.4: Fixed wing air vehicle properties

q, dynamic pressure	15 kg/ms^2
S, area	0.27 m^2
b, span	1.5 m
$\overline{c}$, mean aerodynamic chord	0.18 m

Table 3.5: Fixed wing air vehicle longitudinal derivatives

Longitudinal Derivatives			
X_u	-0.0091172	C_{X_u}	-0.0022521
X_w	0.35811	C_{X_α}	0.088457
Z_u	-1.1223	C_{Z_u}	-5.6611e-05
Z_w	-21.865	C_{L_α}	5.401
Z_q	-2.934	C_{L_q}	8.052
M_u	3.2871e-09	C_{M_u}	4.5109e-09
M_w	-0.38513	C_{M_α}	-0.52851
M_q	-0.88843	C_{M_q}	-13.547

Table 3.6: Fixed wing air vehicle lateral derivatives

Lateral Derivatives			
Y_v	-1.5638	C_{Y_β}	-0.38628
Y_p	0.10488	C_{Y_p}	0.034542
Y_r	0.92831	C_{Y_r}	0.30574
L_v	-0.13316	C_{L_β}	-0.021928
L_p	-2.5604	C_{L_p}	-0.56219
L_r	0.26436	C_{L_r}	0.058045
N_v	0.80234	C_{N_β}	0.13213
N_p	-0.1479	C_{N_p}	-0.032475

3.3 Mathematical Modelling of the Fixed Wing Air Vehicle

Fixed wing air vehicle body forces, moments, translational and rotational velocities are shown in Figure 3.5.

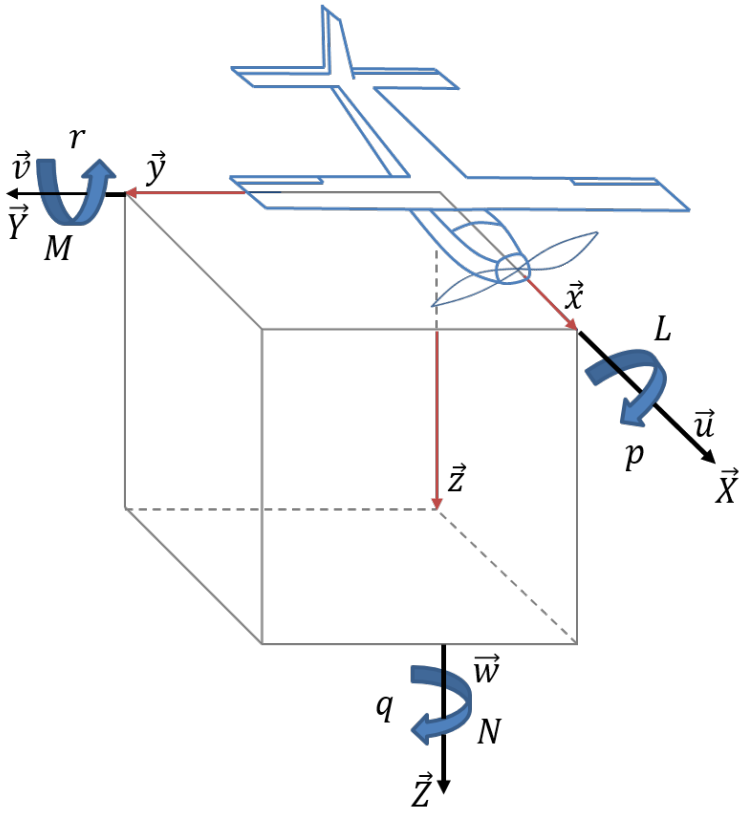

Figure 3.5: Fixed wing air vehicle scheme

In Figure 3.5, u,v,w are forward, side, yaw velocities, L,M,N are roll, pitch, yaw moments, p,q,r are angular velocities in roll, pitch, yaw axes, ϕ, θ, and ψ are roll, pitch, and yaw angles. X,Y,Z are forces in longitudinal, transverse, vertical force, and L,M,N are roll, pitch, yaw moments. Forces acting on the body are found by Newton's equations in addition, since the body rotates Coriolis effect has to be taken into account [58]. Forces on the body, rotational and translational velocities in a fixed frame are represented in Equations 3.7, 3.10, and 3.11, respectively [59, 60].

$$F_B = \begin{bmatrix} X & Y & Z \end{bmatrix}^T \tag{3.7}$$

$$F_B = m(\dot{V}_B + \omega_B \times V_B) \tag{3.8}$$

$$
\begin{aligned}
X - mgsin\theta &= m(\dot{u} + qw - rv) \\
Y + mgcos\theta sin\phi &= m(\dot{v} + ru - pw) \\
Z + mgcos\theta cos\phi &= m(\dot{w} + pv - qu)
\end{aligned} \tag{3.9}
$$

$$
\omega_B = \begin{bmatrix} p & q & r \end{bmatrix}^T \tag{3.10}
$$

$$
V_B = \begin{bmatrix} u & v & w \end{bmatrix}^T \tag{3.11}
$$

External body moments are represented as in Equation 3.12 [59, 60].

$$
\begin{aligned}
L &= I_{xx}\dot{p} + I_{xy}(\dot{q} - pr) + I_{xz}(\dot{r} + pq) + I_{yz}(q^2 - r^2) - (I_{yy} - I_{zz})qr \\
M &= I_{yy}\dot{q} + I_{yz}(\dot{r} - pq) + I_{yx}(\dot{p} + qr) + I_{zx}(r^2 - p^2) - (I_{zz} - I_{xx})pr \\
N &= I_{zz}\dot{r} + I_{zx}(\dot{p} - qr) + I_{zy}(\dot{q} + pr) + I_{xy}(p^2 - q^2) - (I_{xx} - I_{yy})pq
\end{aligned} \tag{3.12}
$$

Because xz plane is the symmetry plane of the fixed wing air vehicle, $I_{xy} = I_{yz} = I_{yx} = I_{zy} = 0$, then Equation 3.12 is turned out to be Equation 3.13 [59, 60].

$$
\begin{aligned}
L &= I_{xx}\dot{p} + I_{xz}(\dot{r} + pq) - (I_{yy} - I_{zz})qr \\
M &= I_{yy}\dot{q} + I_{zx}(r^2 - p^2) - (I_{zz} - I_{xx})pr \\
N &= I_{zz}\dot{r} + I_{zx}(\dot{p} - qr) - (I_{xx} - I_{yy})pq
\end{aligned} \tag{3.13}
$$

CHAPTER 4

FIXED WING VTOL AIR VEHICLE

Fixed wing VTOL air vehicle is the last and the most important system of the study. It is composed of a rotary wing and a fixed wing air vehicle whose scheme is given in Figure 4.1. Since the number of actuators is greater than the states, fixed wing VTOL air vehicle is an over actuated system [61, 62].

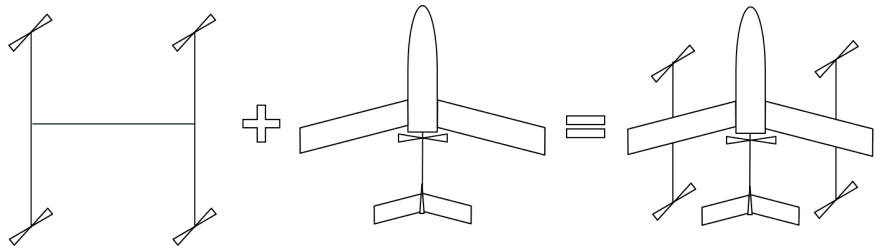

Figure 4.1: Fixed wing VTOL air vehicle scheme

Fixed wing VTOL air vehicle takes off vertically up to a pre-defined altitude. Then, the transition from rotary to fixed wing stage begins with rotating the motor that is used to generate horizontal thrust. After the stall speed of the fixed wing VTOL air vehicle is passed, rotary wings stop and level flight begins. The fixed wing VTOL air vehicle passes to the phase of transient from fixed to rotary wing flight with slowing down to a safe speed which is faster than the stall speed then rotary wings rotate to land. Eventually, fixed wing VTOL air vehicle lands by rotary wings vertically. All flight phases are depicted in Figure 4.2. **In the study, transition phases have essential importance. Since the fixed wing VTOL air vehicle is an over actuated system, desired force and moment values can be generated by a different set of actuators. Developing control allocation algorithm (Section 5.3) with minimizing the energy consumption and state errors are principal focuses of the study.**

Detailed information about the physical system, system identification tests, analysis, results, and mathematical modelling is in the chapter's scope.

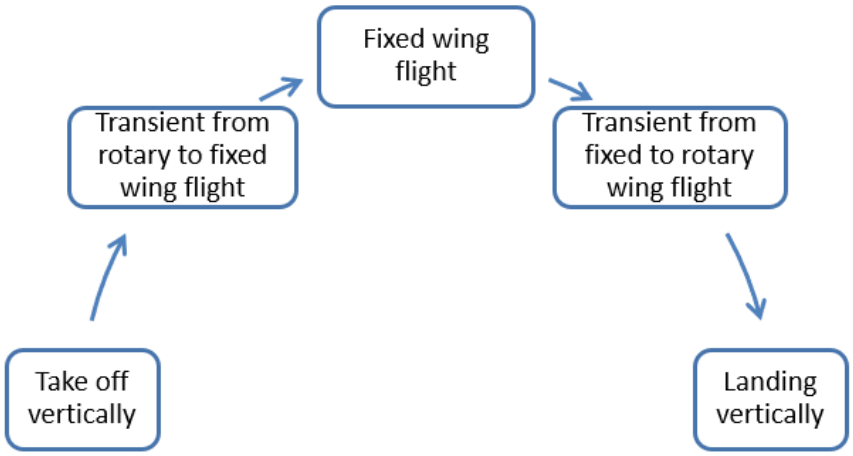

Figure 4.2: Fixed wing VTOL air vehicle flight phases

4.1 Physical System

As stated before, fixed wing VTOL air vehicle is a combination of a fixed wing and a rotary wing air vehicle. As a fixed wing air vehicle Ranger EX Volantex RC is chosen. For the rotary wing part, not a ready to fly rotary wing air vehicle is used. The fixed wing air vehicle is modified such that two rods are fixed to the main wing from underneath. Actuators are showed as numbers in Figure 4.3 and some electronics like controller board, battery, electronic speed controller which are stated in Table 4.1. The motors numbered from 1 to 4 are used during take-off, landing, and transition phases. Propellers generate a thrust force in the axis of rotation and a drag moment in the opposite direction of rotation. The motor and propeller pairs, which are used to take-off and landing, rotate at different directions to balance the generated drag moment [63]. Motor numbered as 5 is used to generate horizontal thrust force that is used to generate the lift force required for the fixed wing VTOL air vehicle. The motors numbered from 6 to 9 are servo motors to actuate the control surfaces, which are ailerons, elevator and rudder.

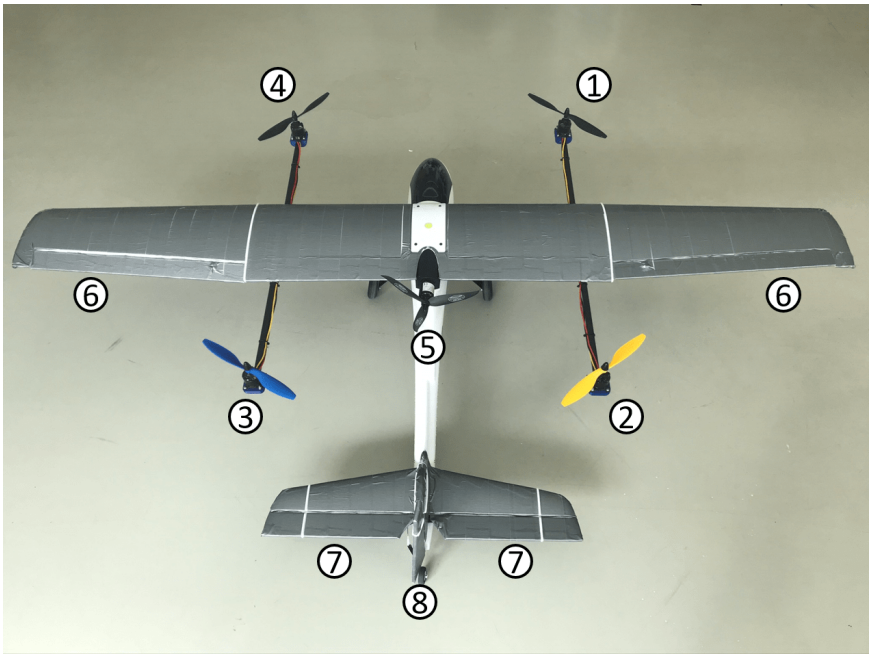

Figure 4.3: Fixed wing VTOL air vehicle scheme

Table 4.1: Fixed wing VTOL air vehicle parts

No.	Type	Brand
1-4	Vertical thrusters	Sunny Sky V2814-11 KV:700
5	Horizontal thruster	Sunny Sky X2826 KV:740
6	Ailerons	Servo motors
7	Elevator	Servo motors
8	Rudder	Servo motors
inside	Controller board	Pixhawk Cube
inside	Electronic speed controller	BLHeliSuite32 4-in-1 ESC (for vertical thrusters)
inside	Electronic speed controller	YEP 60A (2-6S) (for horizontal thruster)
inside	Battery	Zippy Compact 5800 mAh 5S 25C

4.2 System Identification

The fixed wing VTOL air vehicle is identified experimentally to lessen the discrepancies among mathematical model and real system. In this scope, mass moments of

inertias, vertical and horizontal thrusters are identified experimentally. Besides, the fixed wing air vehicle is modelled in XFLR5 software, and aerodynamic analysis is carried out to found lift-drag coefficients related to various angles of attack, longitudinal and lateral derivatives.

4.2.1 Bifilar pendulum test for fixed wing VTOL air vehicle

Mass moments of inertia of the fixed wing air vehicle are found by the bifilar pendulum method as done in Sections 2.2.1 and 3.2.1. Hanged fixed wing air vehicle is given in Figure 4.4.

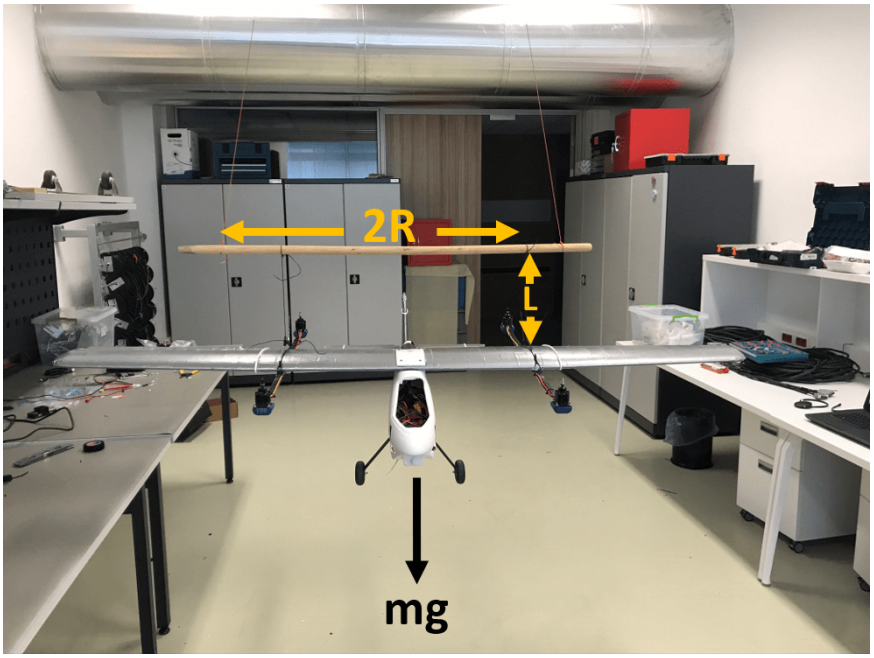

Figure 4.4: Bifilar pendulum experiment of fixed wing VTOL air vehicle

Since the fixed wing air vehicle is symmetric around the xz plane, the mass moment of inertia of the roll axis is assumed to be the pitch axis. Angular velocities of the fixed wing VTOL air vehicle are in roll and yaw axes given in Figures 4.5 and 4.6.

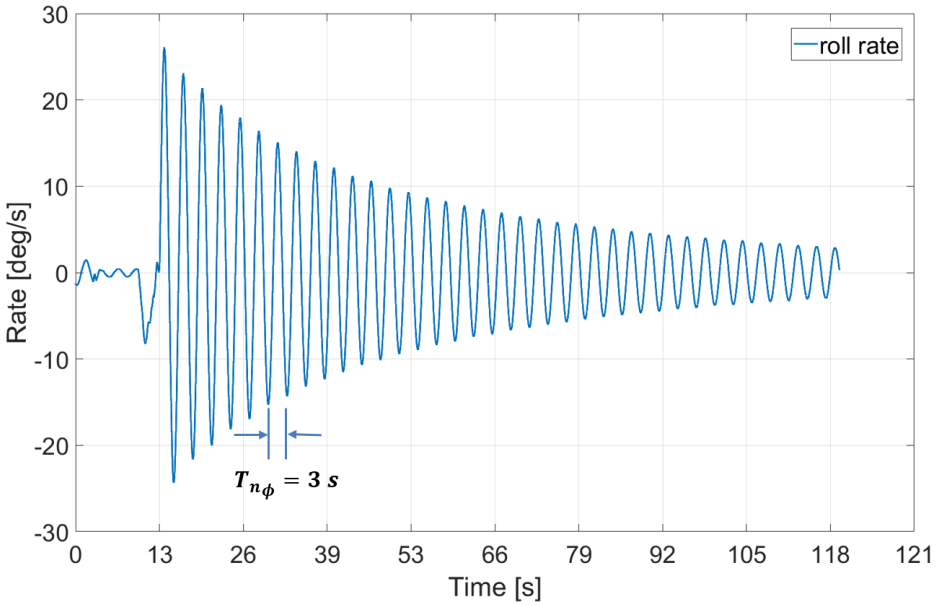

Figure 4.5: Oscillation data of fixed wing VTOL air vehicle in *roll* axis

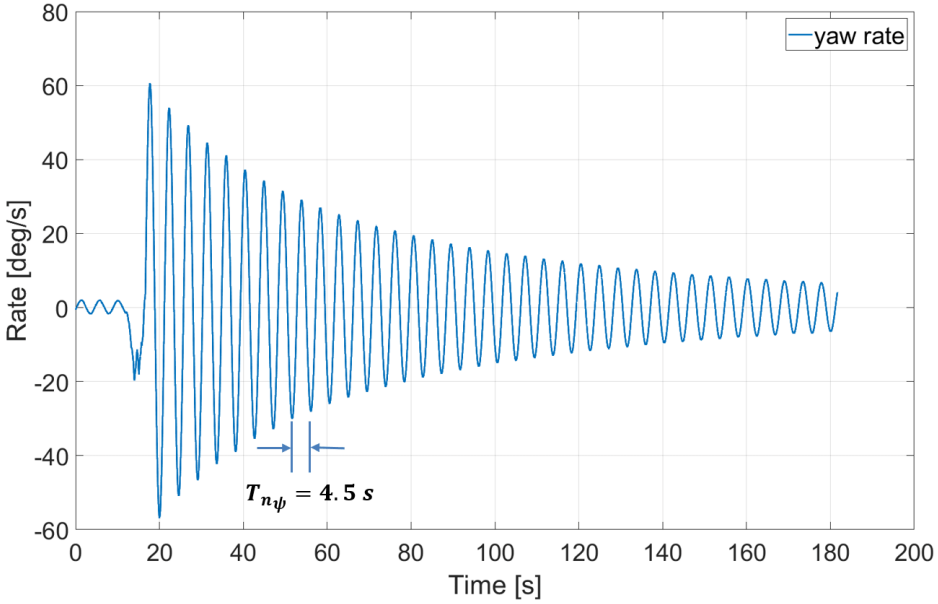

Figure 4.6: Oscillation data of fixed wing VTOL air vehicle in *yaw* axis

Table 4.2: Parameters of fixed wing VTOL air vehicle bifilar pendulum test

Property	**unit**	**roll and pitch axes**	**yaw axis**
Length of the ropes, ℓ	m	0.35	0.3
Distance between ropes, R	m	0.4	0.5
Mass of the system, m	kg	3	3
Gravitational acceleration, g	m/sec^2	9.81	9.81
Oscillation period, T_n	s	3	4.5

Test parameters and measured oscillation periods are given in Table 4.2 are substituted into Equation 2.1. Mass moments of inertia values of the fixed wing VTOL air vehicle are found and given in Table 4.3.

Table 4.3: Mass moment of inertias of the fixed wing VTOL air vehicle

Property	**unit**	**inertia value**
Inertia around x-body axis, I_x	kg.m^2	3.0671
Inertia around y-body axis, I_y	kg.m^2	3.0671
Inertia around z-body axis, I_z	kg.m^2	12.5798

4.2.2 Thrust measurement for fixed wing VTOL air vehicle

To identify the relation among the PWM signals which are the output of the controllers and generated vertical and horizontal thrust values, same methodology is applied as done in Sections 2.2.2 and 3.2.2. Generated thrust and measured rotational velocities for the numbered 1-4 motors, which are used for the vertical motion of the fixed wing VTOL air vehicle in Figure 4.3, are given in Figures 4.7 and 4.8. Similarly, thrust force and rotational velocity of motor 5 are depicted in Figure 4.9.

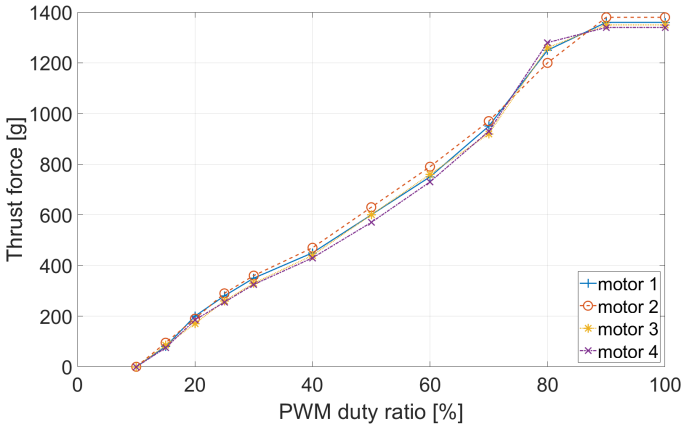

Figure 4.7: Vertical thrusts of *motors 1-4*

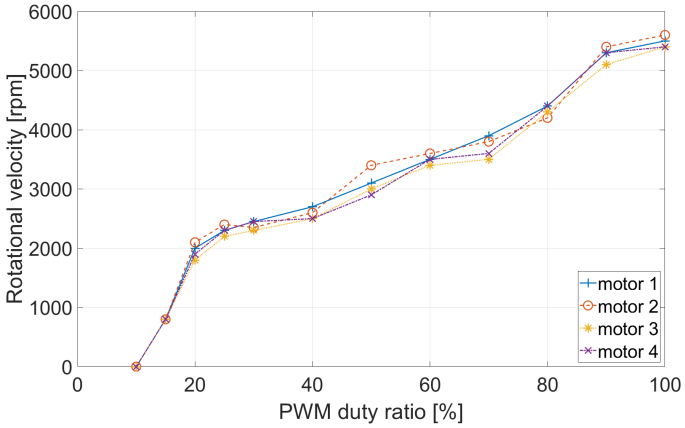

Figure 4.8: Rotational velocities of *motors 1-4*

Figure 4.9: Horizontal thrust and rotational velocity of *motor 5*

Relations among PWM duty ratio and lift force for the rotary wings are found and given in Equation 4.1 by means of the data in Figure 4.7. Relations between the PWM duty ratio and rotational velocity for the rotary wings are found and given in Equation 4.2. Relations among PWM duty ratio, thrust force, and rotational velocity for the fixed wing thruster are given in Equation 4.3. All found relations are implemented in Matlab®/Simulink®and used for simulations.

$$\begin{aligned} F_1 &= -0.0012 \cdot dt^3 + 0.2042 \cdot dt^2 + 6.4878 \cdot dt - 40.558 \\ F_2 &= -0.0008 \cdot dt^3 + 0.1302 \cdot dt^2 + 10.347 \cdot dt - 80.760 \\ F_3 &= -0.0015 \cdot dt^3 + 0.2531 \cdot dt^2 + 4.2808 \cdot dt - 28.866 \\ F_4 &= -0.0017 \cdot dt^3 + 0.3016 \cdot dt^2 + 1.7009 \cdot dt + 3.1724 \end{aligned} \tag{4.1}$$

$$\begin{aligned} \Omega_1 &= 0.0163 \cdot dt^3 - 2.9309 \cdot dt^2 + 201.5591 \cdot dt - 1463.0168 \\ \Omega_2 &= 0.0186 \cdot dt^3 - 3.2865 \cdot dt^2 + 217.3991 \cdot dt - 1612.1080 \\ \Omega_3 &= 0.0164 \cdot dt^3 - 2.8694 \cdot dt^2 + 193.6045 \cdot dt - 1413.9281 \\ \Omega_4 &= 0.0158 \cdot dt^3 - 2.7758 \cdot dt^2 + 190.0940 \cdot dt - 1336.1610 \end{aligned} \tag{4.2}$$

$$\begin{aligned} F_5 &= -0.0015 \cdot dt^3 + 0.2531 \cdot dt^2 + 4.2808 \cdot dt - 25.8663 \\ \Omega_5 &= 0.0158 \cdot dt^3 - 3.9768 \cdot dt^2 + 196.0260 \cdot dt - 1247.2720 \end{aligned} \tag{4.3}$$

where:

$F_{1,2,3,4}$: Lift force of the rotary wings
$\Omega_{1,2,3,4}$: Rotational velocity of the rotary wings
F_5 : Thrust force of the pusher
Ω_5 : Rotational velocity of the pusher

4.2.3 Aerodynamic analysis for fixed wing VTOL air vehicle

To analyse fixed wing VTOL air vehicle aerodynamically XFLR5 software [57] is used. The same procedure in Section 3.2.4 is applied. In addition to that, rotary

wing motors *numbered as 1-4* and main motor *numbered as 5* are added as point masses. Pressure distributions are shown in Figure 4.10a. changing of lift cofficient C_L and pitch moment coefficient C_M are given in Figure 4.10b and 4.10d, respectively. Relation among drag coefficient C_D and C_L is given in Figure 4.10c. All data are implemented in Matlab®/Simulink®and used during simulations.

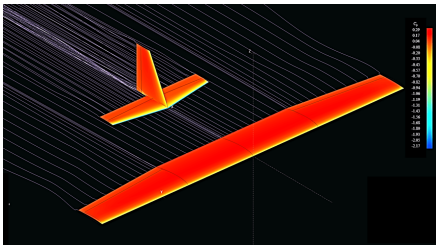

(a) C_p distribution

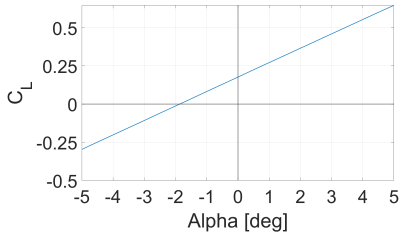

(b) C_L - α relation

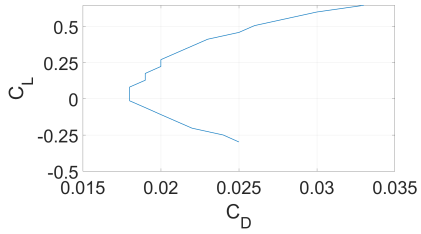

(c) C_L - C_D relation

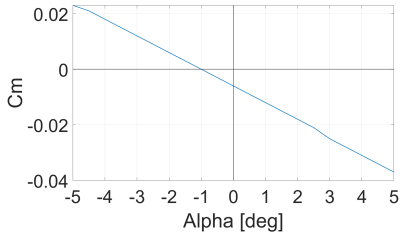

(d) C_M - α relation

Figure 4.10: Aerodynamic analysis of fixed wing VTOL air vehicle

Longitudinal and lateral stability derivatives are found by the aerodynamic analysis and given in Tables 4.5 and 4.6, respectively. The same non-dimensionalize procedure is applied given in Section 3.2.4. Equations used for non-dimensionaliziation are given Equations 4.5, 4.6, and 4.7. Aerodynamic and geometric properties for the fixed wing VTOL air vehicle are given in Table 4.4.

$$q = 1/2 * \rho * V^2 \tag{4.4}$$

$$C_{X_{(u,a)}}, C_{Z_u}, C_{L_{(\alpha,q)}}, C_{Y_{(\beta,p,r)}} = \frac{X_{(u,w)}, Y_{(v,p,r)}, Z_{(u,w,q)}}{q * S} \tag{4.5}$$

$$C_{M_{(u,\alpha,q)}} = \frac{M_{(u,w,q)}}{q * S * \overline{c}} \tag{4.6}$$

$$C_{L_{(\beta,p,r)}}, C_{N_{(\beta,p)}} = \frac{L_{(v,p,r)}, N_{(v,p)}}{q * S * b} \tag{4.7}$$

Table 4.4: Fixed wing VTOL air vehicle properties

q, dynamic pressure	15 kg/ms^2
S, area	0.45 m^2
b, span	2 m
$\overline{c}$, mean aerodynamic chord	0.225 m

Table 4.5: Fixed wing VTOL air vehicle longitudinal derivatives

Longitudinal Derivatives			
X_u	-0.0089672	C_{X_u}	-0.0007988
X_w	0.51747	C_{X_α}	0.046096
Z_u	-1.4319	C_{Z_u}	-1.5511e-05
Z_w	-60.956	C_{L_α}	5.43
Z_q	-9.2646	C_{L_q}	7.3472
M_u	7.7585e-08	C_{M_u}	3.0764e-08
M_w	-0.83833	C_{M_α}	-0.33241
M_q	-3.2457	C_{M_q}	-11.457

Table 4.6: Fixed wing VTOL air vehicle lateral derivatives

Lateral Derivatives			
Y_v	-2.9722	C_{Y_β}	-0.26476
Y_p	0.37118	C_{Y_p}	0.033065
Y_r	2.1595	C_{Y_r}	0.19237
L_v	-0.1709	C_{L_β}	-0.0076118
L_p	-12.745	C_{L_p}	-0.56767
L_r	0.66712	C_{L_r}	0.029714
N_v	1.9186	C_{N_β}	0.085454
N_p	-0.44201	C_{N_p}	-0.019687

4.3 Mathematical Modelling of the Fixed Wing VTOL Air Vehicle

The fixed wing VTOL air vehicle is given in Figure 4.11. Notations given in Figure 4.11 are explained in Table 4.7.

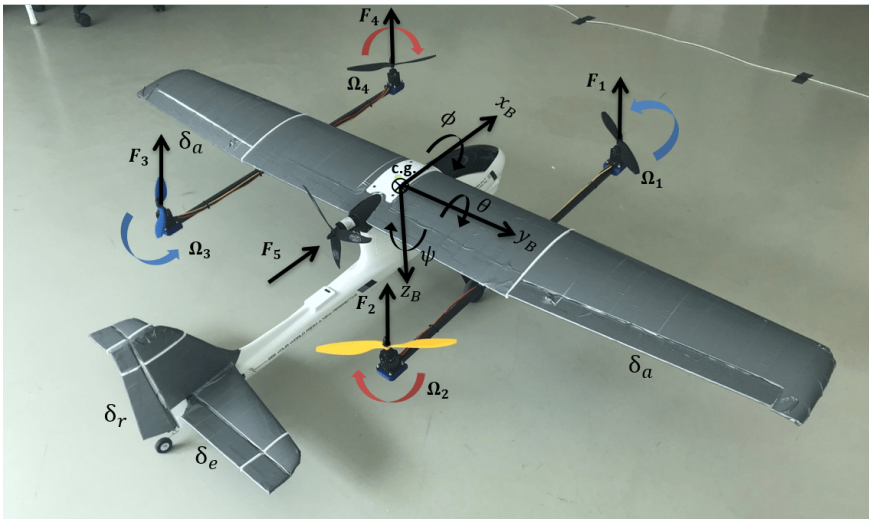

Figure 4.11: Fixed wing VTOL air vehicle

Table 4.7: Fixed wing VTOL air vehicle notations

Notations	Unit	Description
$F_{1,2,3,4}$	N	Generated lift forces from rotary wings
F_5	N	Generated thrust force of pusher of fixed wing
$\Omega_{1,2,3,4}$	rad/s	Rotational velocities of rotary wings
δ_a	rad	Rotational position of ailerons
δ_e	rad	Rotational position of elevator
δ_r	rad	Rotational position of rudder
x_b, y_b, z_b	-	Body fixed coordinate system

The fixed wing VTOL air vehicle has six inputs, three forces **X**,**Y**, and **Z** and moments **L**,**M**, and **N** in body x,y, and z axes. Translational and rotational accelerations are calculated as given in Equation 4.8.

$$
\begin{aligned}
\dot{u} &= \frac{\mathbf{X} - mg\sin\theta}{m} - qw + rv \\
\dot{v} &= \frac{\mathbf{Y} + mg\cos\theta\sin\phi}{m} - ru + pw \\
\dot{w} &= \frac{\mathbf{Z} + mg\cos\theta\cos\phi}{m} - pv + qu \\
\dot{p} &= \frac{\mathbf{L}I_z - qr(I_z^2 - I_z I_y)}{I_x I_z} \\
\dot{q} &= \frac{\mathbf{M} - rp(I_x - I_z)}{I_y} \\
\dot{r} &= \frac{\mathbf{N}I_x - pq(I_y I_x)}{I_x I_z}
\end{aligned}
\tag{4.8}
$$

where:

$\dot{u}, \dot{v}, \dot{w}$: translational accelerations in body x,y, and z directions

$\dot{p}, \dot{q}, \dot{r}$: rotational accelerations around body x,y, and z directions

$\mathbf{X}, \mathbf{Y}, \mathbf{Z}$: forces acting on the in body x,y, and z directions

$\mathbf{L}, \mathbf{M}, \mathbf{N}$: moments acting on the around body x,y, and z directions

I_x, I_y, I_z : mass moment of inertias around body x,y, and z directions

m : mass of the fixed wing VTOL air vehicle

ϕ, θ, ψ : Euler angles

u, v, w : translational velocities in body x,y, and z directions

p, q, r : rotational velocities around body x,y, and z directions

Forces and moments acting on the fixed wing VTOL air vehicle are given in Equations 4.9 and 4.10, respectively.

$$\begin{aligned}
\mathbf{X} &= \mathbf{X_{prop}} + \mathbf{X_{aero}} \\
&= \mathbf{F_5} + \mathbf{X_{aero}} \\
\mathbf{Y} &= \mathbf{Y_{prop}} + \mathbf{Y_{aero}} \\
&= \mathbf{Y_{aero}} \\
\mathbf{Z} &= \mathbf{Z_{prop}} + \mathbf{Z_{aero}} \\
&= \mathbf{F_1} + \mathbf{F_2} + \mathbf{F_3} + \mathbf{F_4} + \mathbf{Z_{aero}}
\end{aligned} \tag{4.9}$$

$$\begin{aligned}
\mathbf{L} &= (-\mathbf{F_1} - \mathbf{F_2} + \mathbf{F_3} + \mathbf{F_4})l + \mathbf{L_5} + \mathbf{L_{aero}} \\
\mathbf{M} &= (+\mathbf{F_1} - \mathbf{F_2} - \mathbf{F_3} + \mathbf{F_4})l + \mathbf{M_{aero}} \\
\mathbf{N} &= (+\mathbf{N_1} - \mathbf{N_2} + \mathbf{N_3} - \mathbf{N_4}) + \mathbf{N_{aero}}
\end{aligned} \tag{4.10}$$

where:

$(\mathbf{X}, \mathbf{Y}, \mathbf{Z})_{\mathbf{prop}}$: Propulsive forces acting on the body in x, y, and z axes

$(\mathbf{X}, \mathbf{Y}, \mathbf{Z})_{\mathbf{aero}}$: Aerodynamic forces acting on the body in x, y, and z axes

l : moment arm (distance among propellers rotation axis and center of gravity)

$\mathbf{N_{1,2,3,4}}$: drag moments due to rotary wing propeller rotation

$\mathbf{L_5}$: drag moment due to fixed wing propeller rotation

Euler angle rates are obtained from the rotational velocities p, q, and r as given in Equation 4.11.

$$\begin{aligned}\dot{\phi} &= p + (q\sin\phi + r\cos\phi)\tan\theta \\ \dot{\theta} &= q\cos\phi - r\sin\phi \\ \dot{\psi} &= \frac{q\sin\phi + r\cos\phi}{\cos\theta}\end{aligned} \tag{4.11}$$

To obtain the position and velocity in the navigation frame transformation matrix, L_{EB}, is used given in Equation 4.12

$$\mathbf{L_{EB}} = \begin{bmatrix} \cos\psi\cos\theta & \cos\psi\sin\theta\sin\phi - \sin\psi\cos\phi & \cos\psi\sin\theta\cos\phi + \sin\psi\sin\phi \\ \sin\psi\cos\theta & \sin\psi\sin\theta\sin\phi + \cos\psi\cos\phi & \sin\psi\sin\theta\cos\phi - \cos\psi\sin\phi \\ -\sin\theta & \cos\theta\sin\phi & \cos\theta\cos\phi \end{bmatrix} \tag{4.12}$$

Velocities in the navigation frame are obtained as given in Equation 4.13.

$$\begin{bmatrix} V_N \\ V_E \\ V_D \end{bmatrix} = \begin{bmatrix} c\psi c\theta & c\psi s\theta s\phi - s\psi c\phi & c\psi s\theta c\phi + s\psi s\phi \\ s\psi c\theta & s\psi s\theta s\phi + c\psi c\phi & s\psi s\theta c\phi - c\psi s\phi \\ -s\theta & c\theta s\phi & c\theta c\phi \end{bmatrix} \begin{bmatrix} u \\ v \\ w \end{bmatrix} \tag{4.13}$$

where:

V_N, V_E, V_D : velocities in navigation frame
s : sine function
c : cosine function

CHAPTER 5

CONTROLLER DESIGN

In this study, PID and ADRC controllers are focused. Both controllers are designed in Matlab®/Simulink®environment and deployed to Pixhawk Cube controller card for real-time control on physical systems. Physical systems are controlled in a closed-loop. Sensor measurements like Euler angles, rotational velocities, accelerations, and GPS positions are feedbacks to the control system. The difference among the actual variable and the sensor measurements are fed to the controllers which decide the desired forces and moments to make the difference zero. The output of the controllers are sent to the actuators and physical system moves and rotates accordingly. This process is called **closed loop control**. Rotary wing, fixed wing, and fixed wing VTOL air vehicles are controlled in a closed-loop. As stated in Section 4, fixed wing VTOL air vehicle is an over actuated system. The output of the controller, which are desired forces and moments, can be generated by a different set of actuators which yields an important and well-known topic which is control allocation. Detailed information about the PID controller, ADRC, and control allocation is given in this chapter.

5.1 PID controller

PID controller is composed of three components which are proportional, integral, and derivative. Each component has an idiosyncratic effect on system response. The **proportional** component is directly related to the error. Increasing the proportional gain increases the speed of the control response. However, increasing the proportional gain too many oscillations observed in the system output. If the proportional gain

is increased further, the system becomes unstable. The **integral** component sums the error. Although the error is small, integral component increases slowly. So, the integral component is used to make steady-state error zero. The **derivative** term is used to decrease the output so the overshoot. In industry, derivative terms are chosen as minimal values because the derivative response is highly sensitive to the noises and error changes. The structure of the unity feedback closed-loop system with a PID controller is given in Figure 5.1. Detailed information about application of PID controller to a fixed air vehicle is given in Section 6.2.

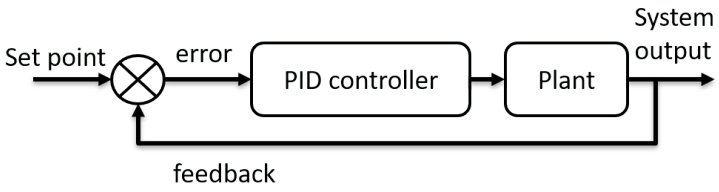

Figure 5.1: Closed loop system with a PID controller

5.2 Linear Active Disturbance Rejection Controller (LADRC)

In this research, it is aimed to design a guidance and control algorithm that can reject unknown disturbances such as gust, asymmetric and slung loads. An active disturbance rejection controller (ADRC) is designed to control the translational and rotational dynamics of the rotary wing air vehicle. ADRC is proposed by Han to deal with nonlinear systems with mixed uncertainty and external disturbance [33]. ADRC estimates the states and the disturbances through the extended state observer (ESO) and compensates for the total disturbances in real-time [38,64,65]. ADRC is composed of a linear tracking differentiator (LTD), a proportional-derivative (PD) controller, and an extended state observer (ESO). LTD is used to send a smoother input signal to the controller to avoid big errors [66, 67]. LTD is not used in the research to push the limit of the controller and the rotary wing air vehicle.

Observers are used to replacing or augmenting the sensors in a control system theory. Some sensors used to estimate states are not very reliable, and some state dynamics are complicated and hard to model. Therefore, state observers are used in a con-

trol system. They can be classified as deterministic and stochastic approaches. In the deterministic approach, observers can be an open loop and closed loop structure. Open-loop state observers are not satisfactory. Closed-loop state observers use observer gain using a feedback loop information which is more reliable. Examples for stochastic observers can be Kalman and Wiener Filter. State observers can be classified as linear and nonlinear. Linear state observers can be a discrete-time and continuous time. When the observer gain is high, then the observer (linear closed-loop Luenberger observer) quickly converges to the state values. Then, the peaking phenomenon occurs, and nonlinear state observers can be used. For example, in the high gain observers, a sliding mode observer can be used. Nevertheless, if the nonlinear system is not linearized, then a nonlinear state observer method, such as sliding mode observer is used [68,69]. In this work, linear deterministic closed loop structure is used in the discrete-time.

Actuator dynamics that are obtained in Sections 2.2.2 and 4.2.2 are taken into account after observing the performance of 2^{nd} order ADRC that increases the order of the ADRC to a 3^{rd} order. Structure of the ADRC, which is composed of a PD controller and an ESO is given in this section. Performance comparisons of the 2^{nd} and the 3^{nd} order ADRCs are given in Section 6.1.3. Structures stated in this section are used to control for one state of the rotary wing air vehicle. During modelling and flight tests on the rotary wing air vehicle, six district ADRCs are designed and implemented to control the translational and rotational dynamics of the rotary wing air vehicle.

The fixed wing VTOL air vehicle has complex dynamics at each axis, including the dynamics of control surfaces and thrust units. So, each axis is expressed by a third order dynamical system that can be described as given in Equation 5.1 where t, y, $\dot{y}$, $\ddot{y}$ are the time, measured output and, first and second time derivatives. w is the external disturbance that acts on the axis. The nonlinear function $f(.)$ can be thought of as a lumped disturbance that includes uncertain dynamics, external disturbances, and plant's nonlinearity [70].

$$y = f(t, y, \dot{y}, \ddot{y}, w(t)) \tag{5.1}$$

Extended state observer (ESO) is used to estimate dynamics that are complex and ex-

pensive to model, plant uncertainties, and the external disturbances. These parameters exist in the system as a lumped disturbance, $f(.)$ which is assumed as an extended state [38].

5.2.1 Second Order ADRC (without actuator dynamic)

The second-order linear Active Disturbance Rejection Controller (ADRC) closed-loop system block diagram is shown in Figure 5.2.

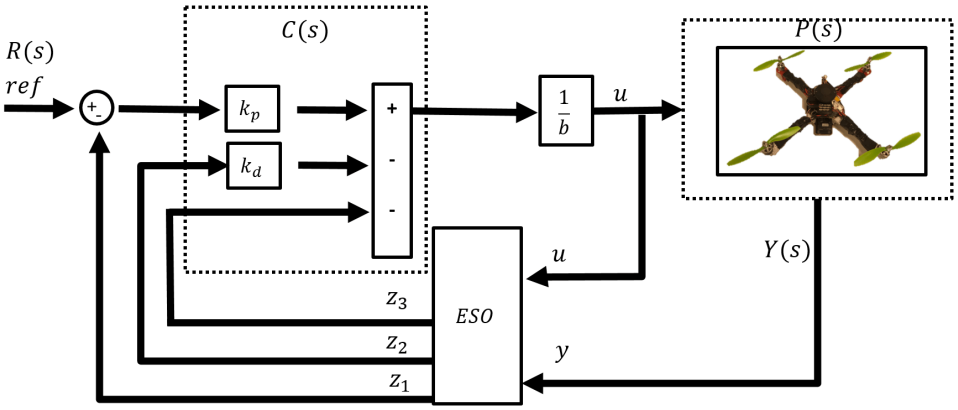

Figure 5.2: Block diagram of second order closed loop system

In Figure 5.2, $R(s)$, $C(s)$, $P(s)$, and $Y(s)$ are the reference input, controller, plant, and output of the system, respectively. Transfer functions of the controller, plant, and closed-loop transfer function of the system are given in Equations. 5.2, 5.3, and 5.4.

$$C(s) = k_p + sk_d \tag{5.2}$$

$$P(s) = \frac{1}{s^2 I_n} \tag{5.3}$$

$$\frac{Y(s)}{R(s)} = \frac{C(s)P(s)}{1 + C(s)P(s)} = \frac{s\frac{k_d}{I_n} + \frac{k_p}{I_n}}{s^2 + s\frac{k_d}{I_n} + \frac{k_p}{I_n}} \tag{5.4}$$

where:

k_p, k_d : Proportional and derivative gains

$Y(s)$: system output

$R(s)$: reference input

$C(s)$: transfer function of the controller

$P(s)$: transfer function of the plant

I_n : mass moment of inertia about rotation axis x,y,and z

Controller gains (k_p and k_d) are calculated by equating the coefficients of corresponding terms of the system closed-loop transfer function and 2^{nd} order desired closed-loop transfer function (G_{CL}) that are given in Equation 5.5 [38]. With this technique, controller gains (k_p and k_d) are calculated with one parameter ω_c that is desired controller bandwidth of the closed-loop system depicted in Equation 5.6. The output of the controller, u, is the desired moment if the state to be controlled is rotational. The desired moment is divided by the inertia of the rotary wing air vehicle, $I_n \cong b$, so the input of the plant is obtained. I_n is the mass moment of inertia which is calculated in Section 2.2.1 and Equation 5.23 where $n = x, y, z$. For roll, pitch, and yaw axes, n can be substituted as x, y and z, respectively. If the state to be controlled is translational, the output of the controller, u, is the desired force which is divided by the mass of the rotary wing air vehicle, m.

$$\frac{Y(s)}{R(s)} = \frac{s\frac{k_d}{I_n} + \frac{k_p}{I_n}}{s^2 + s\frac{k_d}{I_n} + \frac{k_p}{I_n}} \Leftrightarrow G_{CL}(s) = \frac{\omega_c^2}{(s + \omega_c^2)} = \frac{\omega_c^2}{s^2 + 2\omega_c s + \omega_c^2} \tag{5.5}$$

$$\begin{aligned} k_p &= \omega_c^2 \\ k_d &= 2\omega_c \end{aligned} \tag{5.6}$$

An extended state observer is designed to estimate state variables, disturbances, uncertainties, and unmodeled dynamics. z_1, z_2, and z_3 are the estimations of state, y, first time derivative of the state, $\dot{y}$, and the estimation of disturbances, uncertainties, and unmodeled dynamics exist as a lumped dynamic, f, given in Equation 5.7. β_1, β_2, and β_3 are the observer gains, L, to estimate the z_1, z_2, and z_3, respectively. u is the output of the controller and b is the $1/I_n$. State space representation of the observer

is given in Equations 5.7-5.10.

$$z = [z_1\ z_2\ z_3\ ]^T = [y\ \dot{y}\ f]^T \tag{5.7}$$

$$\dot{z} = A_z z + B_z u + L\,(y - \hat{y}) \tag{5.8}$$

$$\begin{bmatrix} \dot{z_1} \\ \dot{z_2} \\ \dot{z_3} \end{bmatrix} = \begin{bmatrix} -\beta_1 & 1 & 0 \\ -\beta_2 & 0 & 1 \\ -\beta_3 & 0 & 0 \end{bmatrix} \begin{bmatrix} z_1 \\ z_2 \\ z_3 \end{bmatrix} + \begin{bmatrix} 0 \\ b \\ 0 \end{bmatrix} u + \begin{bmatrix} \beta_1 \\ \beta_2 \\ \beta_3 \end{bmatrix} (y - \hat{y}) \tag{5.9}$$

$$\hat{y} = C_z z = \begin{bmatrix} 1 & 0 & 0 \end{bmatrix} \begin{bmatrix} z_1 \\ z_2 \\ z_3 \end{bmatrix} = z_1 \tag{5.10}$$

Expanding Equation 5.9, z_1, z_2, and z_3 are obtained as in Equations 5.11-5.13. Substituting Equation 5.13 into Equations 5.12 and 5.11, Equation 5.14 is obtained. The observer gains, L, can be found by equating the characteristic equation of the observer and the desired polynomial (Equation 5.15). Three observer gains β_1, β_2, and β_3 are calculated with one parameter, w_o, that is desired observer bandwidth of the closed loop system.

$$z_1 = \frac{(y - z_1)\beta_1 + z_2}{s} \tag{5.11}$$

$$z_2 = \frac{(y - z_1)\beta_2 + bu + z_3}{s} \tag{5.12}$$

$$z_3 = \frac{(y - z_1)\beta_3}{s} \tag{5.13}$$

$$z_1 = \frac{y(\beta_1 s^2 + \beta_2 s + \beta_3) + sbu}{s^3 + \beta_1 s^2 + \beta_2 s + \beta_3} \tag{5.14}$$

$$(\lambda + \omega_o)^3 = |\lambda I_{3x3} - (A_z - LC_z)| \tag{5.15}$$

$$z_1 = \frac{f(u,y)}{s^3 + \beta_1 s^2 + \beta_2 s + \beta_3} \Leftrightarrow \frac{\omega_o^3}{s^3 + 3\omega_o s^2 + 3\omega_o^2 s + \omega_o^3} \tag{5.16}$$

$$L = \begin{bmatrix} \beta_1 & \beta_2 & \beta_3 \end{bmatrix}^T = \begin{bmatrix} 3\omega_o & 3\omega_o^2 & \omega_o^3 \end{bmatrix}^T \tag{5.17}$$

5.2.2 Third Order ADRC (with actuator dynamic)

In the 2^{nd} order ADRC, all the actuators are assumed as an ideal which means, generated actual moment is equal to the desired moment that is the output of the controller. This is not valid in real life because of the dynamics of the brushless DC motors such as rotor inertia and friction. The dynamics of the actuators are identified in Section 2.2.2 experimentally. The actuator mathematical models are the first order that yields the overall closed-loop system becomes 3^{rd} order. Third-order linear ADRC closed-loop system block diagram is shown in Figure 5.3.

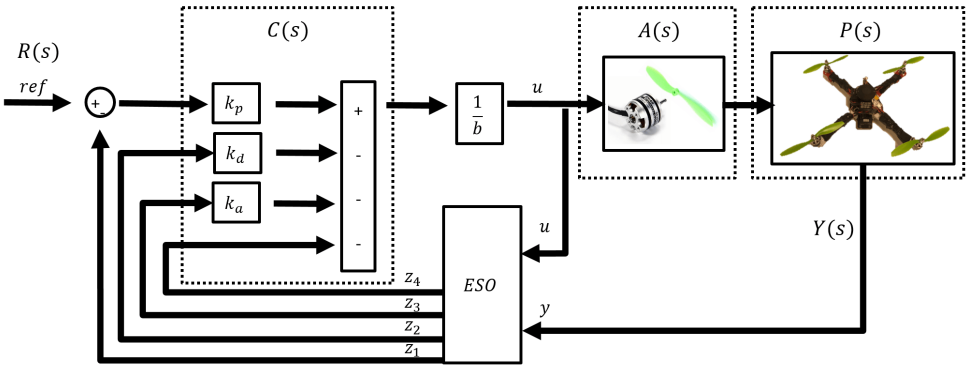

Figure 5.3: Block diagram of third order closed loop system

In Figure 5.3, $R(s)$, $C(s)$, $A(s)$, $P(s)$, and $Y(s)$ are the reference input, controller, actuator, plant, and output of the system. Transfer functions of the controller, actuator, plant, and closed loop transfer function of the system are given in Equations 5.18, 5.19, 5.20, and 5.21, respectively. Equation 5.22 is obtained by substituting the $C(s)$,

$A(s)$ and $P(s)$ into Equation 5.21.

$$C(s) = k_p + sk_d + s^2k_a \tag{5.18}$$

$$A(s) = \frac{K_m}{Ts + 1} \tag{5.19}$$

$$P(s) = \frac{1}{s^2 I_n} \tag{5.20}$$

$$\frac{Y(s)}{R(s)} = \frac{C(s)A(s)P(s)}{1 + C(s)A(s)P(s)} \tag{5.21}$$

$$\frac{Y(s)}{R(s)} = \frac{\frac{(k_p + sk_d + s^2k_a)K_m}{TI_n}}{s^3 + s^2\frac{(k_aK_m + I_n)}{TI_n} + s\frac{k_dK_m}{TI_n} + \frac{k_pK_m}{TI_n}} \tag{5.22}$$

where K_m and T are the motor torque and time constant which are found in Section 2.2.2. All the parameters are known in Equation 5.22 except k_p, k_d, and k_a which are proportional, derivative, and acceleration gains of the controller. To select the controller gains, characteristic equation of the closed loop transfer function of the system is equated to a third order polynomial. Controller gains are calculated with equating the coefficients of like terms of the system closed loop transfer function and the 3^{rd} order desired closed loop transfer function that is given in Equation 5.23. Three controller gains (k_p, k_d, and k_a) are calculated by adjusting one parameter, ω_c, that is the desired controller bandwidth of the closed loop system in Equation 5.24.

$$\frac{Y(s)}{R(s)} = \frac{\frac{(k_p + sk_d + s^2k_a)K_m}{TI_n}}{s^3 + s^2\frac{(k_aK_m + I)}{TI_n} + s\frac{k_dK_m}{TI_n} + \frac{k_pK_m}{TI_n}} \Leftrightarrow \frac{\omega_c^3}{s^3 + 3\omega_c s^2 + 3\omega_c^2 s + \omega_c^3} = G_{CL}(s) \tag{5.23}$$

$$\begin{aligned} k_p &= \omega_c^3 \\ k_d &= 3\omega_c^2 \\ k_a &= 3\omega_c \end{aligned} \tag{5.24}$$

An extended state observer is designed to estimate state variables, uncertainties, and unmodeled dynamics. z_1, z_2, z_3, and z_4 are the estimations of state, y, first time derivative of the state, $\dot{y}$, the second time derivative of the state, $\ddot{y}$, and the estimation of disturbances, uncertainties, and unmodeled dynamics exist as a lumped dynamic, f, given in Equation 5.25. β_1, β_2, β_3, and β_4 are the observer gains, L, to estimate the z_1, z_2, z_3, and z_4 respectively. u is the output of the controller and b is the output coefficient. State space representation of the observer is given in Equations 5.25-5.28.

$$z = [z_1 \; z_2 \; z_3 \; z_4]^T = [y \; \dot{y} \; \ddot{y} \; f]^T \tag{5.25}$$

$$\dot{z} = A_z z + B_z u + L\,(y - \hat{y}) \tag{5.26}$$

$$\begin{bmatrix} \dot{z_1} \\ \dot{z_2} \\ \dot{z_3} \\ \dot{z_4} \end{bmatrix} = \begin{bmatrix} -\beta_1 & 1 & 0 & 0 \\ -\beta_2 & 0 & 1 & 0 \\ -\beta_3 & 0 & 0 & 1 \\ -\beta_4 & 0 & 0 & 0 \end{bmatrix} \begin{bmatrix} z_1 \\ z_2 \\ z_3 \\ z_4 \end{bmatrix} + \begin{bmatrix} \beta_1 \\ \beta_2 \\ \beta_3 \\ \beta_4 \end{bmatrix} y + \begin{bmatrix} 0 \\ 0 \\ b \\ 0 \end{bmatrix} u \tag{5.27}$$

$$\hat{y} = C_z z = \begin{bmatrix} 1 & 0 & 0 & 0 \end{bmatrix} \begin{bmatrix} z_1 \\ z_2 \\ z_3 \\ z_4 \end{bmatrix} = z_1 \tag{5.28}$$

Expanding Equation 5.27, z_1, z_2, z_3 and z_4 are obtained as in Equations 5.29-5.32. z_1 can be found by substituting Equation 5.32 into Equations 5.31, 5.30, and 5.29 yields Equation 5.33. The observer gains, L, can be found by equating the characteristic equation of the observer and the desired polynomial, Equation 5.34. Four observer gains β_1, β_2, β_3 and β_4 are calculated with one parameter, w_o, which is desired observer bandwidth of the closed loop system. I_{4x4} in Equation 5.34 is a four-dimensional identity matrix.

$$z_1 = \frac{\beta_1(y - z_1) + z_2}{s} \tag{5.29}$$

$$z_2 = \frac{\beta_2(y - z_1) + z_3}{s} \tag{5.30}$$

$$z_3 = \frac{\beta_3(y - z_1) + z_4 + bu}{s} \tag{5.31}$$

$$z_4 = \frac{\beta_4(y - z_1)}{s} \tag{5.32}$$

$$z_1 = \frac{y(s^3\beta_1 + s^2\beta_2 + s\beta_3 + s\beta_4) + sbu}{s^4 + s^3\beta_1 + s^2\beta_2 + s\beta_3} \tag{5.33}$$

$$(\lambda + \omega_o)^4 = |\lambda I_{4x4} - (A_z - LC_z)| \tag{5.34}$$

$$z_1 = \frac{f(u,y)}{s^4 + \beta_1 s^3 + \beta_2 s^2 + \beta_3 s + \beta_4} \Leftrightarrow \frac{\omega_o^3}{s^4 + 4\omega_o s^3 + 6\omega_o^2 s^2 + 4\omega_o^3 s + \omega_o^4} \tag{5.35}$$

$$L = \begin{bmatrix} \beta_1 & \beta_2 & \beta_3 & \beta_4 \end{bmatrix}^T = \begin{bmatrix} 4\omega_o & 6\omega_o^2 & 4\omega_o^3 & \omega_o^4 \end{bmatrix}^T \tag{5.36}$$

5.2.3 n^{th} order ADRC

As stated in Section 5.2, ADRC is includes an extended state observer. The convergence of the Luenberger observer increases as the observer gain increases, which may lead to a peaking phenomenon in the initial error, which can be amplified by the high gain [71, 72]. A system with the order of n can be described as given in Equation 5.37.

$$\begin{cases} \dot{x_1} = x_2 \\ \dot{x_2} = x_3 \\ \vdots \\ \dot{x_n} = f\left(x_1, \ldots, x_n, w\left(t\right), t\right) + bu \\ y = x_1 \end{cases} \tag{5.37}$$

where:

$x_1, \ldots, x_n$	: states
u	: control input
y	: output
$w(t)$	: external disturbance
b	: system parameter
$f(x_1, \ldots, x_n, w(t), t)$	: uncertain function (*lumped parameter*)

The word *extended* comes from adding an augmented variable as given in Equation 5.38.

$$x_{n+1} = f\left(x_1, \ldots, x_n, w\left(t\right), t\right) \tag{5.38}$$

Combining Equation 5.37 and 5.38 yields Equation 5.39

$$\begin{cases} \dot{x_1} = x_2 \\ \dot{x_2} = x_3 \\ \vdots \\ \dot{x}_n = x_{n+1} + bu \\ \dot{x}_{n+1} = h(t) \\ y = x_1 \end{cases} \tag{5.39}$$

where:

$$h(t) = \dot{f}(x_1, \ldots, x_n, w(t), t)$$

To estimate the states, a linear ESO is designed as;

$$\begin{cases} \dot{z_1} = z_2 - \beta_1(z_1 - y) \\ \dot{z_2} = z_3 - \beta_2(z_1 - y) \\ \vdots \\ \dot{z_n} = z_{n+1} - \beta_n(z_1 - y) + bu \\ \dot{z}_{n+1} = -\beta_{n+1}(z_1 - y) \end{cases} \tag{5.40}$$

where:

$z_1, z_2, \ldots, z_n, z_{n+1}$: estimates of states $x_1, x_2, \ldots, x_n, x_{n+1}$
$\beta_1, \beta_2, \ldots, \beta_{n+1}$: observer gains

ESO differs from "extended high-gain observers" in such a way that estimation of total disturbance in addition to the state variables. Then, the total disturbances can be rejected in the control loop.

5.3 Control Allocation

A system, which has a redundant set of actuators, is called an over actuated system. Control allocation algorithms arrange the effectors to produce the desired forces and moments. A set of actuators is chosen because of cost, size, standardization, accuracy, dynamic response and flexibility concerns. Some effectors may be used for different control systems with different purposes. Moreover, effectors have hardware limits such as input saturation and rate constraints [73, 74].

Control allocation algorithms can be used in different application areas. Some of these areas are shown in Figure 5.4.

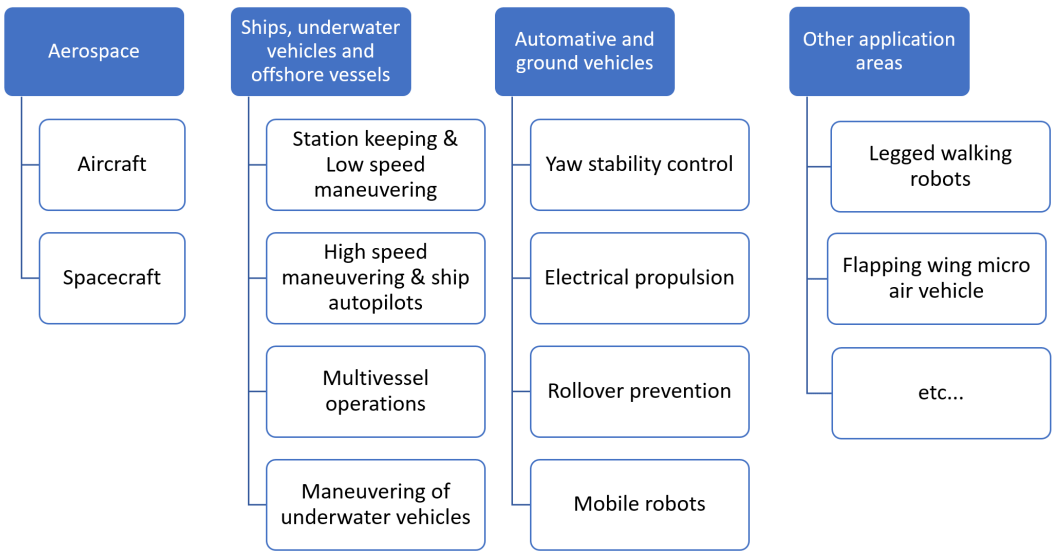

Figure 5.4: Control allocation application areas

Traditional aircraft have two ailerons for roll control, two elevators for pitch control and one rudder for yaw control. Therefore, it can be said that any control allocation algorithm is not needed. Conventional aircrafts have control surfaces represented in Figure 5.5.

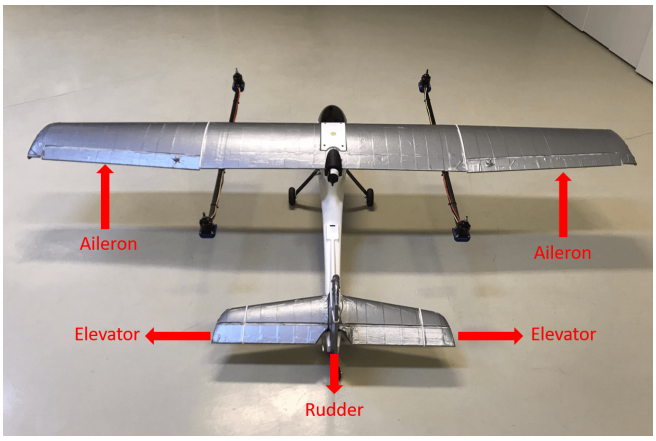

Figure 5.5: Conventional aircraft control surfaces

Having many control surfaces is a reason for applying control allocation algorithms. The reason for having many control surfaces can be due to actuator failures and unconventional aircrafts such as VTOL, V-tails (coupled lateral and longitudinal forces), tiltable propellers and thrust vector jets. Furthermore, control surfaces like a spoiler, flaps can be used for the same purposes with different control surfaces.

Control allocation algorithm architecture is shown in Figure 5.6. In this figure, high-level motion control computes forces and moments. Control allocation maps the virtual input to individual actuators in the physical limits of the actuators. Low-level motion control controls the actuators to achieve the desired forces and moments. The purposes of the control allocation algorithms may be minimizing the power/fuel consumption, actuator tear and wear and many more [73].

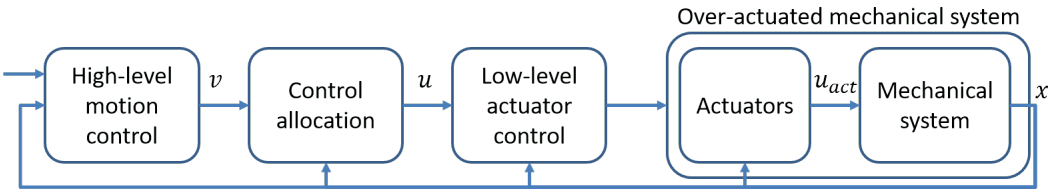

Figure 5.6: Control allocation algorithm architecture

where:

v : virtual input

u : control input

u_{act} : input to mechanical system that are forces and/or moments

x : state of the mechanical system

Besides, control allocation can be applied to air vehicles for different purposes such as **minimum wing loading, minimum control surface deflection, minimum radar signature, minimum drag, maximum lift, minimum energy consumption, and so on**. Types of control allocation algorithms can be classified according to the linear and nonlinear actuator types. Moreover, the linear algorithms can be investigated into two groups, such as unconstrained/constrained related to the actuator types. The classification is represented in Figure 5.7.

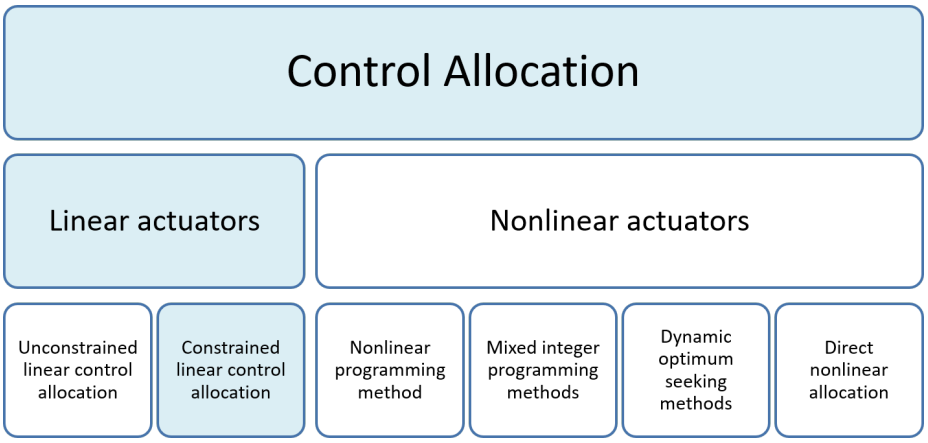

Figure 5.7: Types of the control allocation algorithms

Actuators used in the fixed wing VTOL air vehicle are identified experimentally as

stated in Section 4.2.2. As seen in Figure 4.7, actuators that are used for vertical thrust have some linear and nonlinear regimes. However, actuators behave linearly for the thrust regime that is needed for vertical motion. That is why the blue shaded control allocation path is followed in Figure 5.7.

Redistributed pseudo-inverse and daisy-chaining, direct allocation, error minimization using linear programming and error minimization using quadratic programming methods are used in constrained linear allocation methods [73]. Control allocation is used in aerospace for various applications for different aims such as fault-tolerant [75–79], transition among vertical and horizontal flight phases [80–86]. Allocation efficiency is a crucial performance index to decide the quality of the control allocation algorithms.

5.3.1 Constrained linear control allocation methods

5.3.1.1 Redistributed pseudo-inverse

Generalized inverse method is very simple for implementation and cannot solve the allocation problem for the attainable moment subset, so the allocation efficiency is low. To solve this problem, redistributed pseudo-inverse method is proposed [87]. With the method, control inputs that exceeds the hardware limits removed from the solution set. Then, control allocation problem solved with the available set of solutions.

Step 1: Distribution of desired moment using pseudo-inverse method

$$u = Pv \tag{5.41}$$

where:

v : desired moments
u : distribution results
P : Pseudo-inverse distribution matrix

Step 2: If the control distributed desired moments exceeds the hardware limits, control variables are divided into two. The first group is u_1 which is beyond hardware

limit. The second group u_2 which is in the limits of hardware. So, the control efficiency matrix B is composed of two parts as B_1 and B_2.

Step 3: Control variable u_1 is set to limits. So, maximum generated moment from u_1 becomes $v_1 = B_1 u_1$. Since the desired moment is v, and v_1 amount of moment is generated because of the hardware limits, v_2 is missing desired moment $v_2 = v - v_1$.

Step 4: Solving the $v_2 = B_2 u_2$ with generalized inverse method, final solution is $v = Bu$ where $u = [u_1 u_2]^T$.

The redistribution procedure is done repeatedly till finding a feasible solution which is in limits of the hardware. *This method does not guarantee to have the optimal solution and minimization about the control allocation error [88].*

5.3.1.2 Daisy chaining

The daisy-chaining algorithm is straightforward and less effective control allocation algorithm [80]. Actuators and effectors are grouped into two or more. The groups have priorities. Even if one actuator is saturated, for example, in the first group, is disabled. Then, the second group is allocated to fill the gap among allocated and required forces and moments.For example, suppose daisy chaining algorithm was used for the fixed wing VTOL air vehicle. In that case, actuators can be grouped into two which are fixed wing control u_1 and rotary wing control u_2. Desired forces/moments v can be generated with partitioning the control effectiveness matrix as given in Equation 5.42.

$$v = Bu = \begin{bmatrix} B_r & B_f \end{bmatrix} \begin{bmatrix} u_r \\ u_f \end{bmatrix} = B_r u_r + B_f u_f \tag{5.42}$$

where:

v : desired moments

B : control effectiveness matrix

B_r : control effectiveness matrix for rotary wing

B_f : control effectiveness matrix for fixed wing

u : distribution results

u_r : distribution result for rotary wing

u_f : distribution result for fixed wing

5.3.1.3 Direct allocation

The direct control allocation method is a kind of constrained control allocation method, by [81], aims to find a real number, ρ, and a vector, δ_1, such that

$$\mathbf{B}\delta_1 = \rho \mathbf{d}_{des} \tag{5.43}$$

and

$$\delta_{min} \leq \delta \leq \delta_{max} \tag{5.44}$$

δ depends on the ρ, which represents the amount of control power to touch the limit of attainable moment set (AMS). If $\rho \leq 1$, the demanded moment is within the range of AMS can be generated. If $\rho > 1$, demand moment exceeded the AMS limits and scaled back to touch the boundary of the AMS. If $\rho > 1$, then $\delta = \delta_1/\rho$. If $\rho \leq 1$, then $\delta = \delta_1$.

5.3.2 Linear and Quadratic Programming Optimization Methods

First requirement is to satisfy the demand (error minimization problem) then selecting the effector positions or rotational velocities to satisfy the demand (control minimization problem). The objective of **error minimization** is to find a vector δ, given $\mathbf{B}$ and $\mathbf{d}_{des}$, such that

$$J = \|\mathbf{B}\delta - \mathbf{d}_{des}\|_p \tag{5.45}$$

is minimized, subject to

$$\delta^- \leq \delta \leq \delta^+ \tag{5.46}$$

where:

J : cost to be minimized

p : norm type 1,2,∞

δ^-, δ^+ : minimum and maximum limits of control surface

Norm type depends on the algorithm that is used to perform the minimization. For LP solvers, the norm becomes 1.

$$\min_{\delta} J = \|\mathbf{B}\delta - \mathbf{d}_{des}\|_1 \tag{5.47}$$

This is transformed into a standard LP problem [89],

$$\min_{\delta_s} J = \begin{bmatrix} 0 & ... & 0 & 1 & ... & 1 \end{bmatrix} \begin{bmatrix} \delta \\ \delta_s \end{bmatrix} \tag{5.48}$$

subject to

$$\begin{bmatrix} \delta_s \\ -\delta \\ \delta \\ -\mathbf{B}\delta + \delta_s \\ \mathbf{B}\delta + \delta_s \end{bmatrix} \geqslant \begin{bmatrix} 0 \\ -\delta^+ \\ \delta^- \\ -\mathbf{d}_{des} \\ \mathbf{d}_{des} \end{bmatrix} \tag{5.49}$$

where:

δ_s : vector of slack variables

Slack variables represent the amount of control power that exceeds the available power. The control law command is feasible if $J = 0$. Otherwise it is infeasible and control effectors cannot meet the demand. To add flexibility to the control deficiency problem weights may be added. In this case, error minimization problem becomes,

$$\min_{\delta_s} J = \begin{bmatrix} 0 & ... & 0 & \mathbf{W}_d^T \end{bmatrix} \begin{bmatrix} \delta \\ \delta_s \end{bmatrix} \tag{5.50}$$

where:

$\mathbf{W}_d^T$: weighting vector

The weights give flexibility to increase or decrease the power of effectors compared to the others. The solution of the problems either unweighted (Equation 5.48) or weighted (Equation 5.50) minimizes the 1-norm of the distance between $\mathbf{W}\delta$ and $\mathbf{d}_{des}$.

As stated before control minimization problem is the second optimization. If there are enough effectors to satisfy Equation 5.47 such that $J = 0$, then multiple solutions may exist which yields secondary objective is achieved. **The important thing is to find a direct and best solution for the over actuated system among multiple ones**. Then, the control minimization becomes,

$$\min_{\delta_s} J = \begin{bmatrix} 0 & ... & 0 & \mathbf{W}_u^T \end{bmatrix} \begin{bmatrix} \delta \\ \delta_s \end{bmatrix} \tag{5.51}$$

subject to

$$\begin{bmatrix} \delta_s \\ -\delta \\ \delta \\ -\delta + \delta_s \\ \delta + \delta_s \end{bmatrix} \geqslant \begin{bmatrix} 0 \\ -\delta^+ \\ \delta^- \\ -\delta_p \\ \delta_p \end{bmatrix} \tag{5.52}$$

where:

δ_p : preferred control effector position

Minimum control deflection, minimum wing loading, minimum drag, minimum actuator power can be an example of the secondary objective [90].

5.3.3 Solving the Linear Problem (LP) Problem

The simplex algorithm is a method to solve Linear Problems [91]. Since the algorithm is run in the Pixhawk Cube controller board, it is essential to be a simple process.

The frequency closed-loop control loop of the fixed wing VTOL air vehicle is $250Hz$ which means the algorithm must be solved within $4ms$. The simplex method moves from one feasible solution to another, in such a way that the value of the objective function decreases continuously till a minimum is reached.

5.3.4 Control allocation algorithm comparisons

Direct allocation and surface search methods, although they solve control allocation problem, they have a large amount of computing work, and good at real-time ability. The generalized inverse method cannot solve the allocation problem; efficiency is low, simplicity very high. Early surface saturation phenomenon often happens when it is used in practice. Pros and cons of the control allocation algorithms are given in Table 5.1. '+' used for the pro or much, 'o' is used for neutral, and '-' used for cons or less. The direct allocation method is proposed to solve the problem.

Table 5.1: Comparison of the control allocation algorithms

Control allocation algorithm	Computing work	Real-time ability	Efficiency	Simplicity
Redistributed pseudo-inverse	high	o	o	+
Daisy chaining	less	+	-	-
Direct allocation	+	+	+	+

CHAPTER 6

SIMULATION AND FLIGHT TESTS

Designed guidance and autopilot algorithms are deployed in the Pixhawk Cube controller board, and flight tests are carried out for rotary wing and fixed wing air vehicles. For **rotary wing air vehicle**, position and attitude control algorithms are designed. Flights are done with 2^{nd} and 3^{rd} order ADRCs for 20m and 40m flight ranges. Each flight is repeated with different load configurations like no-load, asymmetrically located constant and slung load cases. For the **fixed wing air vehicle**, PID controller is designed for roll and pitch axes. Since the fixed wing air vehicle is not the final system, control of yaw and altitude dynamics are out of scope. For **fixed wing VTOL air vehicle**, 3^{rd} order ADRCs are implemented to control the attitudes of the air vehicle during vertical motion. Control allocation algorithm is implemented for the flight phases, the transition from rotary to fixed wing and fixed to the rotary wing. States of the fixed wing VTOL air vehicle are also controlled by 3^{rd} order ADRCs for level flight.

6.1 Rotary wing air vehicle

6.1.1 Trajectory tracking

For trajectory tracking of the rotary wing air vehicle, translational and rotational dynamics of the rotary wing air vehicle are controlled by using the six distinct active disturbance rejection controllers.

Position control is made under the assumption that the attitude control has fast track ability. Therefore, small angle approximation assumption can be applied in Equations

2.9 and 2.10. Desired accelerations in x and y directions ($\ddot{x}_{des}$ and $\ddot{y}_{des}$) are calculated as in Equation 6.1. Moreover, trajectory tracking can be done along and/or cross the trajectory. In this study, the controller is not designed to make trajectory tracking for the curvature sense of trajectory. Under these assumptions, desired roll and pitch angles (ϕ_{des} and θ_{des}) are calculated as in Equation 6.1 [92].

$$\begin{aligned} \ddot{x}_{des} &= \frac{U_1}{m}\left(\theta cos\psi + \phi sin\psi\right) \\ \ddot{y}_{des} &= \frac{U_1}{m}\left(\theta sin\psi - \phi cos\psi\right) \\ \phi_{des} &= \frac{m}{U_1}\left(\ddot{x}_{des} sin\psi - \ddot{y}_{des} cos\psi\right) \\ \theta_{des} &= \frac{m}{U_1}\left(\ddot{x}_{des} cos\psi + \ddot{y}_{des} sin\psi\right) \end{aligned} \tag{6.1}$$

x and y positions of the rotary wing air vehicle are controlled by two distinct ADRCs. Reference values in x and y positions (x_{ref} and y_{ref}) are fed into the ADRCs and desired accelerations ($\ddot{x}_{des}$ and $\ddot{y}_{des}$) and external forces are calculated [93].

Then, ϕ_{des} and θ_{des} are obtained by using the desired acceleration on the body along x and y with using the current yaw angle as in Equation 6.1.

On the other hand, altitude control is made by using the total thrust value of U_1. Total thrust is altered wisely to control the altitude channel of the rotary wing air vehicle [93].

6.1.2 Attitude control

Attitude control is made by using three distinct ADRCs as well. ϕ_{des} and θ_{des} obtained from Equation 6.1 and ψ_{ref} are fed into the ADRC and external moments are calculated.

Finally, external forces and moments are given into the rotary wing air vehicle 6 DOF model and position, velocity and attitude in navigation frame are obtained.

Controller structure used in trajectory control is given in Figure 6.1. First of all, according to the reference x and y coordinates (x_{ref} and y_{ref}), desired accelerations ($\ddot{x}_{des}$ and $\ddot{y}_{des}$) in x and y directions are calculated in "X-Y Position ADRC" block.

Then, desired accelerations are fed into the "Desired Angle Calculation Block" and desired angles (ϕ_{des} and θ_{des}) are obtained. Meanwhile, required thrust value, U_1, to control the altitude of the rotary wing air vehicle is calculated in "Altitude ADRC" block with using the reference altitude value, z_{ref}, and current altitude value which is one of the rotary wing air vehicle states. Required roll, pitch, and yaw moments (U_2, U_3 and U_4) are calculated in "Attitude ADRC" block to control the translational and rotational dynamics except for the altitude. Then, all of the forces and moments are fed into the rotary wing air vehicle and states are obtained.

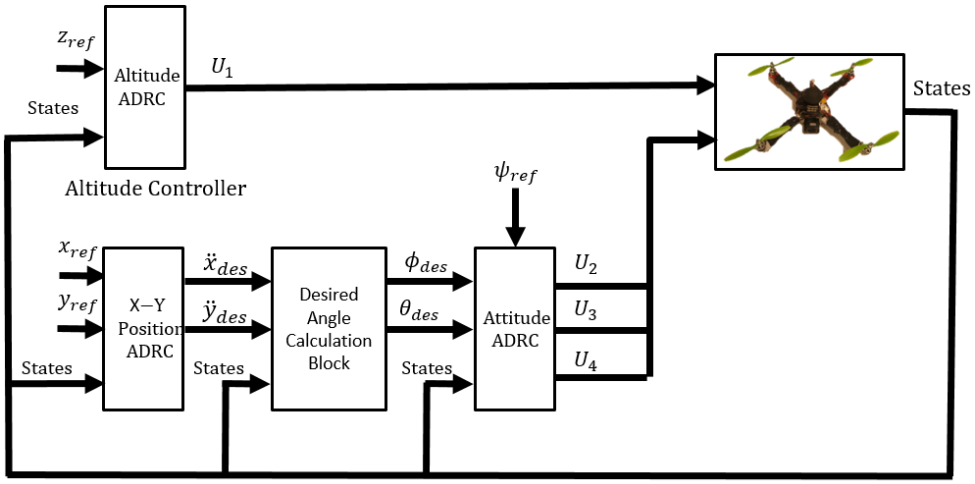

Figure 6.1: Tracking controller structure

6.1.3 Results

The rotary wing air vehicle is modelled experimentally to have a close result between simulations and flight tests. Translational and rotational dynamics of the rotary wing air vehicle is modelled in the Matlab®/Simulink®environment. Indoor flight tests are done in Mobile Robotics Research Laboratory of Mechanical Engineering Department of TEDU. Unloaded, static loaded and slung loaded flight tests are carried out with the same controller and observer gains. Test methodology of the study is given in Figure 6.2. Indoor and outdoor flight photos are depicted in Figures 6.3a and 6.3b, respectively.

In rotary wing air vehicle, translational dynamics are obtained using the GPS, and

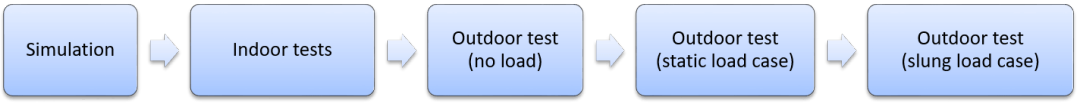

Figure 6.2: Test methodology

(a) Indoor flight

(b) Outdoor flight

Figure 6.3: Indoor and outdoor flights

the rotational dynamics are obtained from the gyroscopes and accelerometers of the Pixhawk Cube controller board. *All translational and rotational dynamics are controlled by six discrete active disturbance rejection type controllers. These controllers are designed as* 2^{nd} *and* 3^{rd} *order to investigate how adding the actuator dynamic affects the performance of the rotary wing air vehicle is under different disturbances like the gust, wind, an asymmetrically placed stationary and slung loads.* A 0.1kg weighted load is placed at one arm of the rotary wing air vehicle, which is shown in Figure 6.4 for the statically loaded case. *For the slung loaded case, the same load is hanged from the same location at the same arm with a rope whose length is 0.5m.*

Two scenarios are planned in such a way that the rotary wing air vehicle follows flight path from point zero to point six which are given in Figures 6.5a and 6.5b with a constant yaw angle of 0°to observe the performances of the designed controllers. Twelve different flight tests which are given in Table 6.1 are carried out with the rotary wing air vehicle to see the performances of the controllers. To measure the performances of the controllers, Integrated Squared Errors (ISE) are calculated as in Equation 6.2.

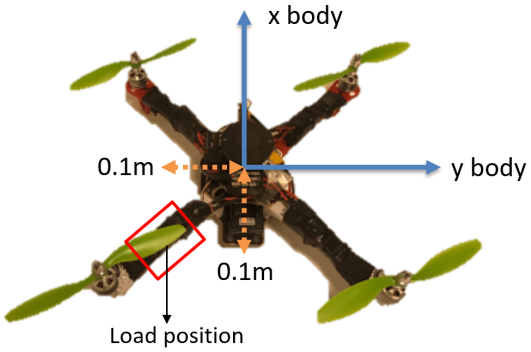

Figure 6.4: Load position

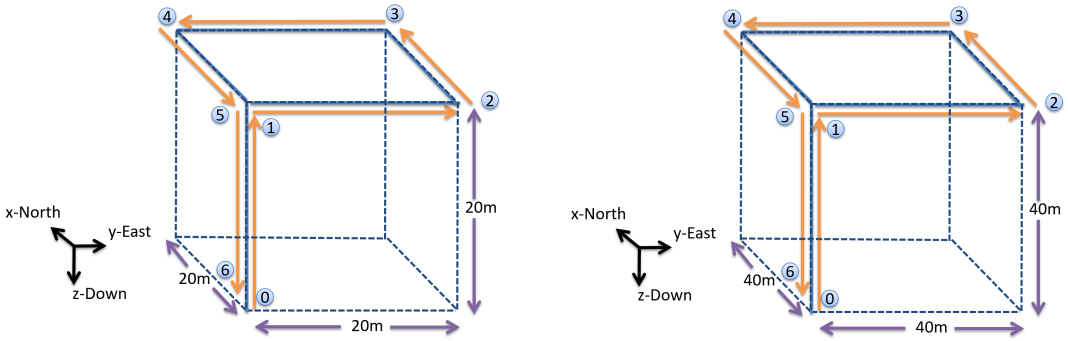

(a) 20 m flight path

(b) 40 m flight path

Figure 6.5: Flight trajectories

Table 6.1: Flight test types

20 m flight			**40 m flight**		
Flight No	**Load**	**ADRC order**	**Flight No**	**Load**	**ADRC order**
1	unloaded	2^{nd}	7	unloaded	2^{nd}
2	unloaded	3^{rd}	8	unloaded	3^{rd}
3	static load	2^{nd}	9	static load	2^{nd}
4	static load	3^{rd}	10	static load	3^{rd}
5	slung load	2^{nd}	11	slung load	2^{nd}
6	slung load	3^{rd}	12	slung load	3^{rd}

Table 6.2: Controller gains

Parameter	x	y	z	ϕ	θ	ψ
2^{nd} order ADRC controller bandwidth, w_c	0.4	0.4	0.4	0.7	0.7	0.7
2^{nd} order ADRC observer bandwidth, w_o	3.2	3.2	3.2	5.6	5.6	5.6
3^{rd} order ADRC controller bandwidth, w_c	2	2	2	2.7	2.7	2
3^{rd} order ADRC observer bandwidth, w_o	16	16	16	21.6	21.6	16

$$ISE = \int e^2(t)dt \tag{6.2}$$

Rotary wing air vehicle follows the trajectory commands with smaller errors at flight tests with 3^{rd} order ADRC compared to 2^{nd} order ADRC for all load cases. Higher controller and observer bandwidths can be achieved by adding the actuator dynamics to the off the design of the ADRC. Flight trajectories of 20m and 40m flights are given in Figure 6.6. 20m flight trajectories for unloaded, static loaded, and slung loaded cases are depicted in Figures 6.6a, 6.6c, and 6.6e, respectively. Similarly, 40m flight trajectories for unloaded, static loaded, and slung loaded cases are shown in Figures 6.6b, 6.6d, and 6.6f, respectively. Controller and observer gains for all cases can be seen in Table 6.2. As can be seen in Figure 6.6, for both 2^{nd} and 3^{rd} order ADRC flights, the best tracking performances are achieved in unloaded cases because not having any disturbances except the weather conditions. Due to the location of the load, external negative roll and positive pitch moments are applied to the rotary wing air vehicle during the flights. Drifts are observed in both negative x and y directions. In slung loaded case, disturbances are higher compared to the static loaded case because of the oscillation of the load. These disturbances are rejected with the active disturbance rejection controllers. Alternatively, flight trajectories of the rotary wing air vehicle are grouped as ADRC types and given in Figure 6.7. Trajectories of the rotary wing air vehicle for 20m and 40m flights with 2^{nd} order ADRC under different load cases are depicted in Figures 6.7a and 6.7b, respectively. Similarly, trajectories of the rotary wing air vehicle for 20m and 40m flights with 3^{rd} order ADRC under different load cases are shown in Figures 6.7c and 6.7d, respectively.

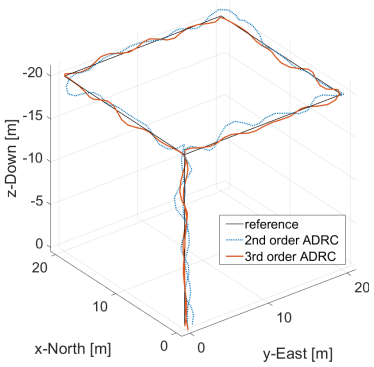

(a) Unloaded case for 20m flight

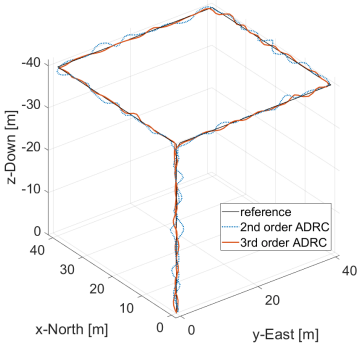

(b) Unloaded case for 40m flight

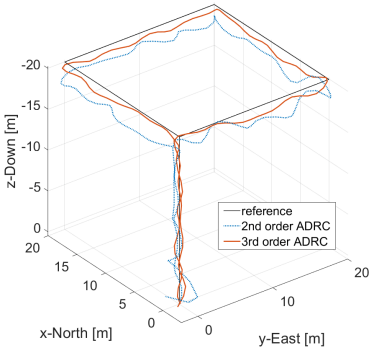

(c) Static load case for 20m flight

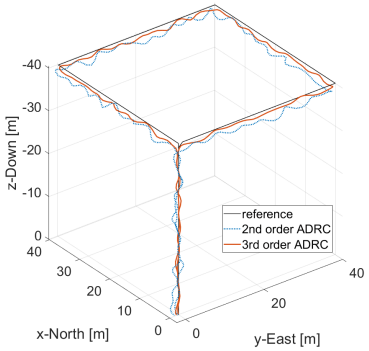

(d) Static load case for 40m flight

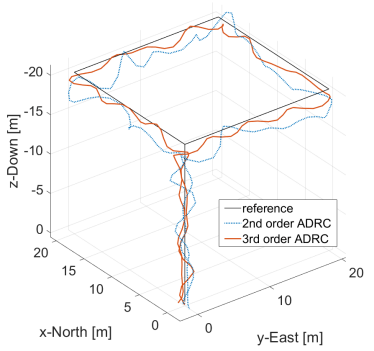

(e) Slung load case for 20m flight

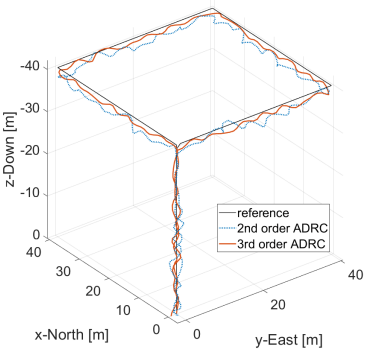

(f) Slung load case for 40m flight

Figure 6.6: Flight trajectories for different loads for 20m and 40m flights

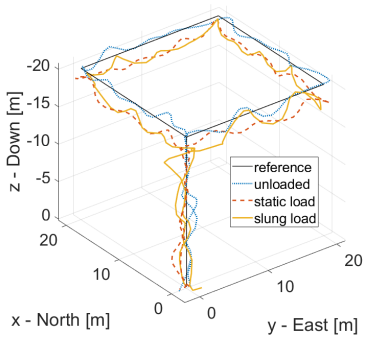

(a) Second Order ADRC results for 20m flight

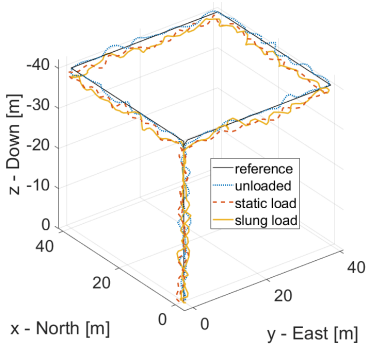

(b) Second Order ADRC results for 40m flight

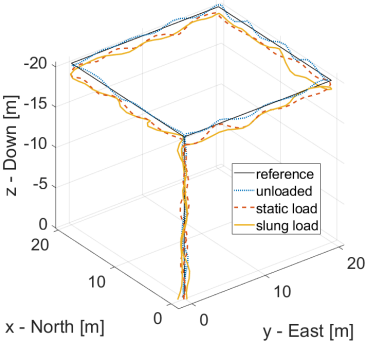

(c) Third Order ADRC results for 20m flight

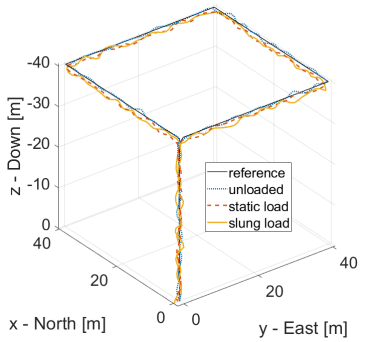

(d) Third Order ADRC results for 40m flight

Figure 6.7: Flight trajectories for different controllers for 20m and 40m flights

ISE values are scaled such that the maximum ISE value is assigned to 100. Scaled ISE values of the translational states for 20m and 40m flights with different load cases are given in Figures 6.8a and 6.8b, respectively. It can be clearly seen from Figure 6.8 that the performance of 3^{rd} order ADRC is better compared to 2^{nd} order ADRC in translational dynamics.

For unloaded case, 2^{nd} and 3^{rd} order ADRCs are applied to rotary wing air vehicle model in Matlab®/Simulink®environment for roll and pitch states. Simulation results of 2^{nd} and 3^{rd} order ADRCs for roll axis can be seen in Figures 6.9a-6.10a for 20m and 40m flights, respectively. Roll dynamics of the rotary wing air vehicle both for 2^{nd} and 3^{rd} order ADRCs are given in Figures 6.9b-6.9c for 20m flight and Figures 6.10b-6.10c for 40m flight. Simulation results of 2^{nd} and 3^{rd} order ADRCs for pitch

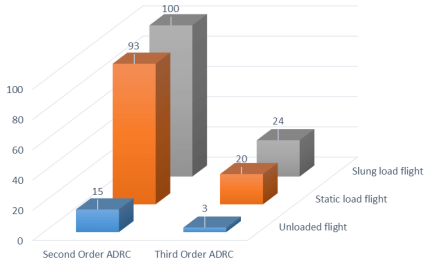

(a) Flight trajectory scaled ISE values for 20m flight

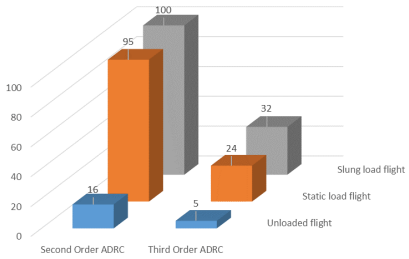

(b) Flight trajectory scaled ISE values for 40m flight

Figure 6.8: Scaled ISE values for different controllers and flight cases

axis can be seen in Figures 6.11a-6.12a for 20m and 40m flights, respectively. Pitch dynamics of the rotary wing air vehicle both for 2^{nd} and 3^{rd} order ADRCs are given in Figures 6.11b-6.11c for 20m flight and Figures 6.12b-6.12c for 40m flight. As can be seen in Figures from 6.9 to 6.12, roll and pitch dynamics are less oscillatory and peaks are relatively small with 3^{rd} order ADRC compared to 2^{nd} order ADRC for unloaded cases in 20m and 40m flights.

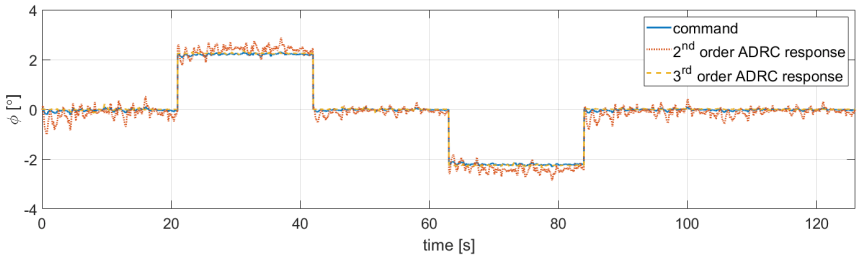

(a) Second and Third Order ADRC simulation results

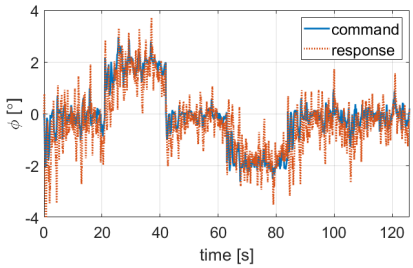

(b) Second Order ADRC results

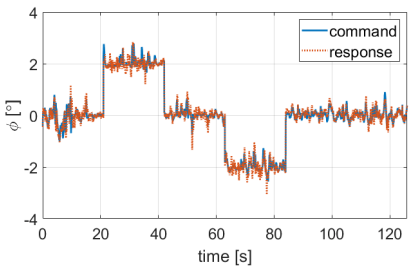

(c) Third Order ADRC results

Figure 6.9: Roll dynamics for unloaded case - 20m flight

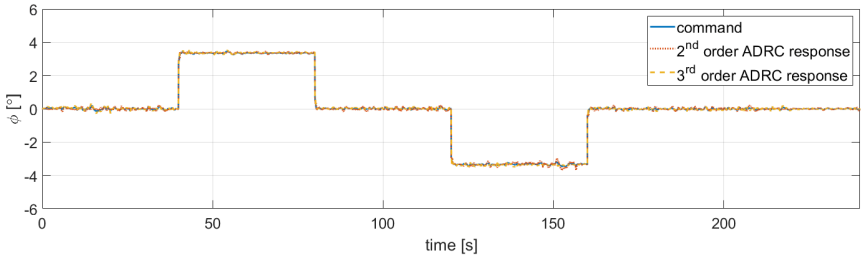

(a) Second and Third Order ADRC simulation results

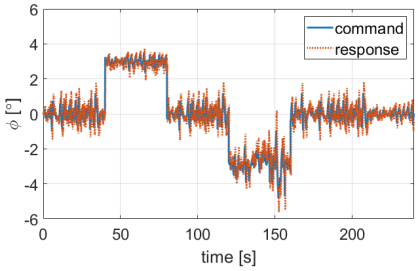

(b) Second Order ADRC results

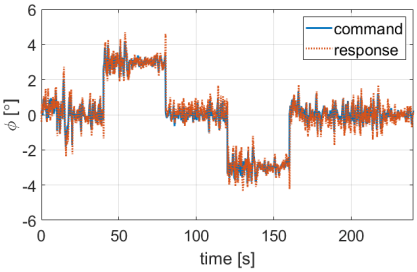

(c) Third Order ADRC results

Figure 6.10: Roll dynamics for unloaded case - 40m flight

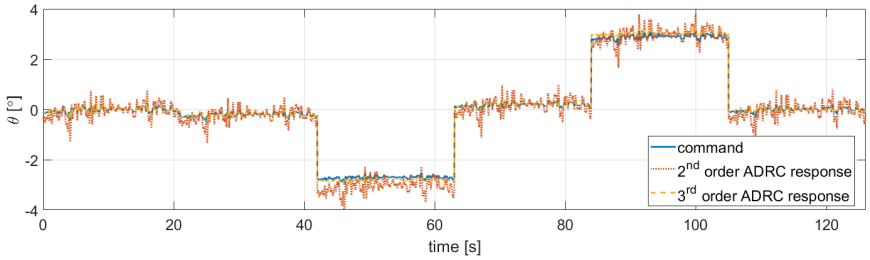

(a) Second and Third Order ADRC simulation results

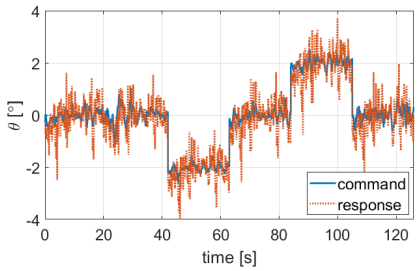

(b) Second Order ADRC results

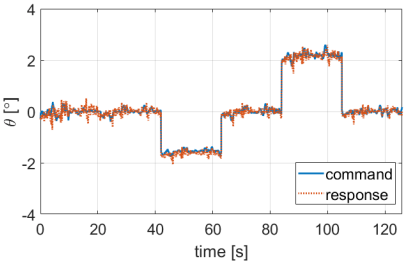

(c) Third Order ADRC results

Figure 6.11: Pitch dynamics for unloaded case - 20m flight

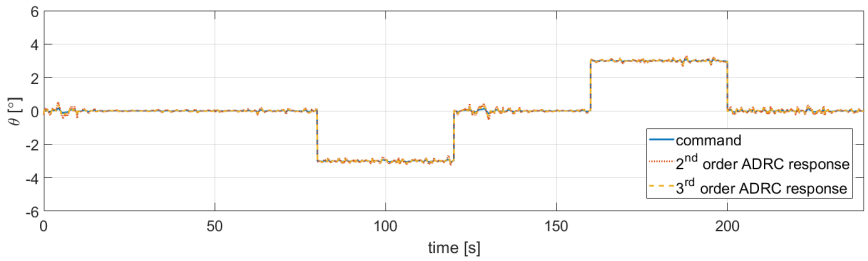

(a) Second and Third Order ADRC simulation results

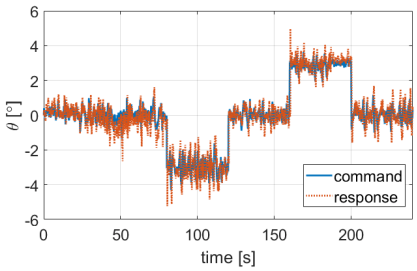

(b) Second Order ADRC results

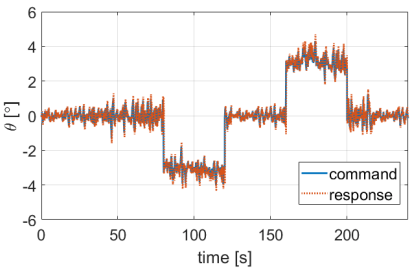

(c) Third Order ADRC results

Figure 6.12: Pitch dynamics for unloaded case - 40m flight

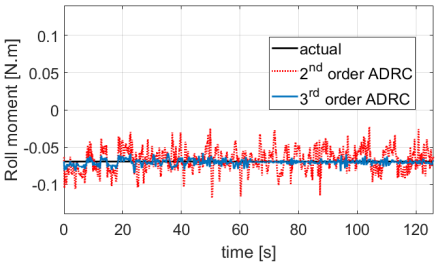

(a) Roll disturbance estimation

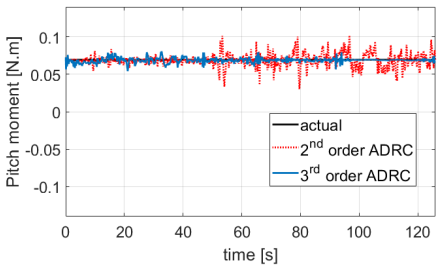

(b) Pitch disturbance estimation

Figure 6.13: Disturbance estimation for static loaded case - 20m flight

As in the unloaded case, explanations about the differences of the 2^{nd} and 3^{rd} order ADRC simulation and flight responses mentioned above are valid for the static load case. The load acts as a constant disturbance in the x and y body axes of the rotary wing air vehicle as a negative roll and positive pitch moment, respectively. Roll and pitch moment contributions of the load and estimated disturbances by the 2^{nd} and 3^{rd} order ADRCs during the 20m flight are given in Figures 6.13a and 6.13b, respectively. Estimated disturbance during the 40m flight are shown in Figures 6.14a

and 6.14b for roll and pitch axes, respectively. Disturbance estimation of 2^{nd} and 3^{rd} order ADRCs are proven with the flight tests as depicted in Figures 6.13 and 6.14. It is also shown that the estimation performance of the 3^{rd} order ADRC is superior to 2^{nd} order ADRC.

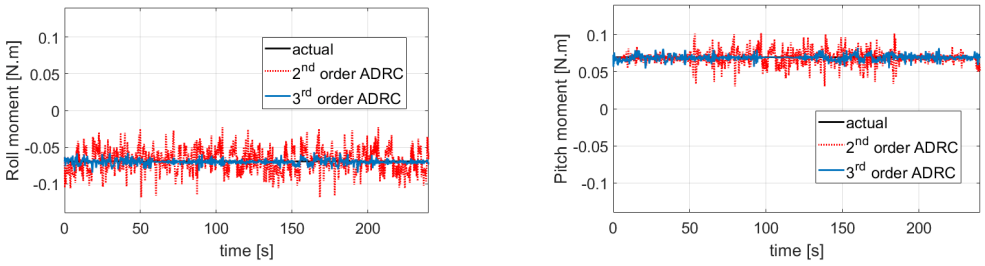

(a) Roll disturbance estimation

(b) Pitch disturbance estimation

Figure 6.14: Disturbance estimation for static loaded case - 40m flight

For static loaded case, 2^{nd} and 3^{rd} order ADRCs are applied to the rotary wing air vehicle model in Matlab®/Simulink®environment for roll and pitch states. Simulation results of 2^{nd} and 3^{rd} order ADRCs for roll axis can be seen in Figures 6.15a-6.16a for 20m and 40m flights, respectively. Roll dynamics of the rotary wing air vehicle both for 2^{nd} and 3^{rd} order ADRCs are given in Figures 6.15b-6.15c for 20m flight and Figures 6.16b-6.16c for 40m flight. Simulation results of 2^{nd} and 3^{rd} order ADRCs for pitch axis can be seen in Figures 6.17a-6.18a for 20m and 40m flights, respectively. Pitch dynamics of the rotary wing air vehicle both for 2^{nd} and 3^{rd} order ADRCs are given in Figures 6.17b-6.17c for the 20m flight and Figures 6.18b-6.18c for the 40m flight. As can be seen in Figures from 6.15 to 6.18, roll and pitch dynamics are less oscillatory and peaks are relatively small with 3^{rd} order ADRC compared to 2^{nd} order ADRC for static loaded case in 20m and 40m flights. There are steady-state errors during both 20m and 40m flights which are done with 2^{nd} order ADRC. These steady-state errors can be seen in Figures 6.15b and 6.17b for roll and pitch dynamics during the 20m flight and Figures 6.16b and 6.18b during the 40m flight, respectively. 3^{rd} order ADRC has also better performance in eliminating the steady-state errors and following the command under constant disturbances. Flight data with the 3^{rd} order ADRC are shown in Figures 6.15c and 6.17c for roll and pitch dynamics during the 20m flight and Figures 6.16c and 6.18c during the 40m flight, respectively.

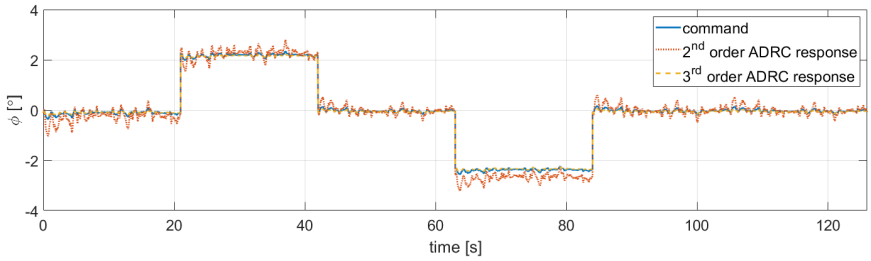

(a) Second and Third Order ADRC simulation results

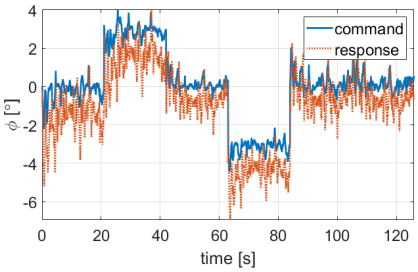

(b) Second Order ADRC results

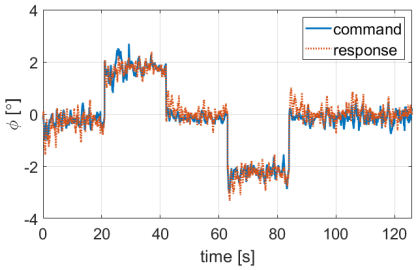

(c) Third Order ADRC results

Figure 6.15: Roll dynamics for static loaded case - 20m flight

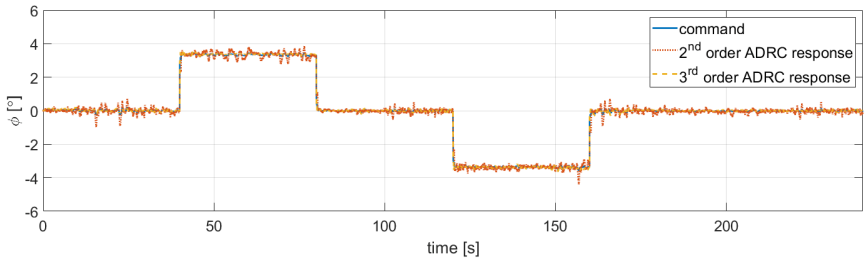

(a) Second and Third Order ADRC simulation results

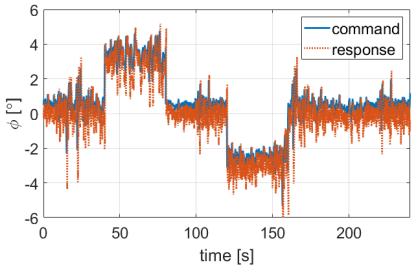

(b) Second Order ADRC results

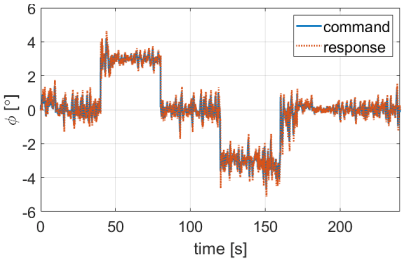

(c) Third Order ADRC results

Figure 6.16: Roll dynamics for static loaded case - 40m flight

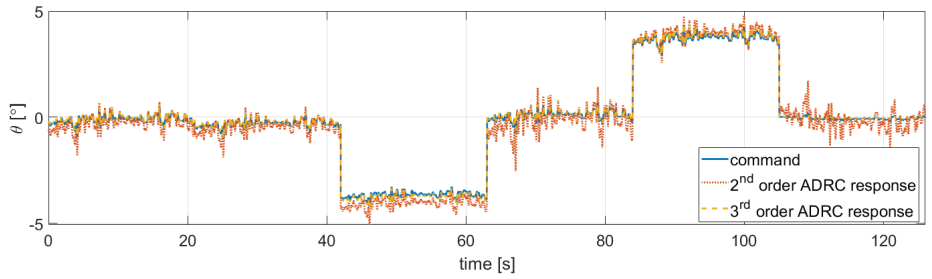

(a) Second and Third Order ADRC simulation results

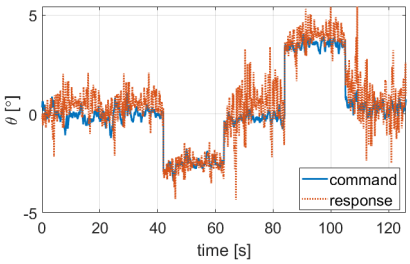

(b) Second Order ADRC results

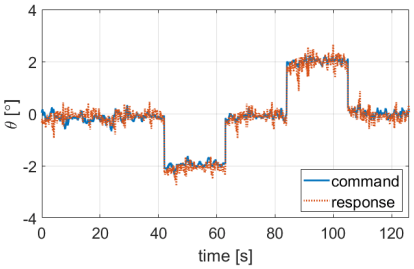

(c) Third Order ADRC results

Figure 6.17: Pitch dynamics for static loaded case - 20m flight

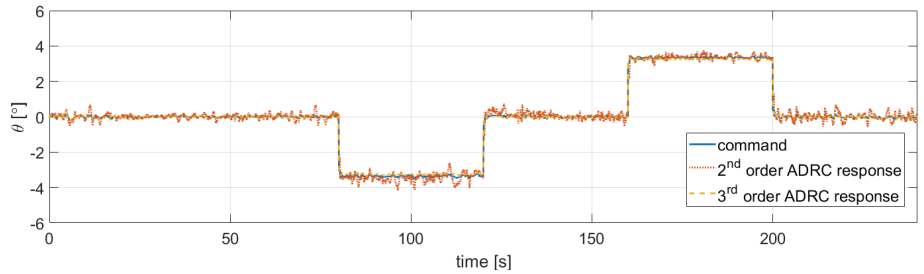

(a) Second and Third Order ADRC simulation results

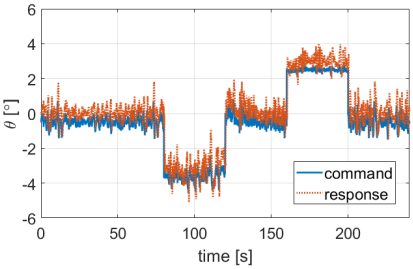

(b) Second Order ADRC results

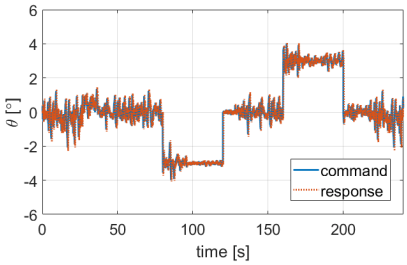

(c) Third Order ADRC results

Figure 6.18: Pitch dynamics for static loaded case - 40m flight

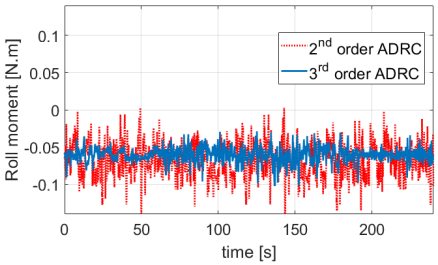

(a) Roll disturbance estimation

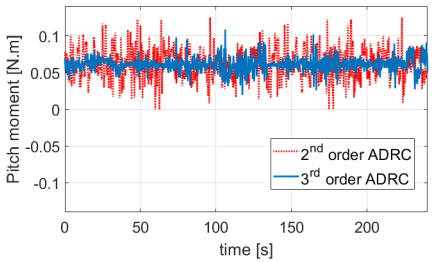

(b) Pitch disturbance estimation

Figure 6.20: Disturbance estimation for slung loaded case - 40m flight

In slung load case, it is hard to model the stochastic oscillation of the load so just flight test is carried out with the 2^{nd} and 3^{rd} order ADRCs. In-flight tests, disturbances caused by the oscillation of the load are estimated and given in Figures 6.19a and 6.19b during 20m flight and Figures 6.20a and 6.20b during 40m flight in roll and pitch axes, respectively.

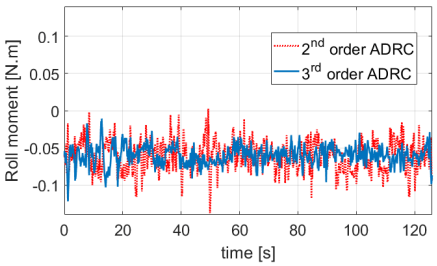

(a) Roll disturbance estimation

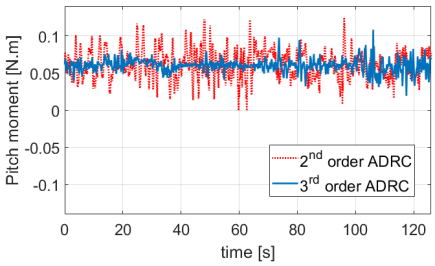

(b) Pitch disturbance estimation

Figure 6.19: Disturbance estimation for slung loaded case - 20m flight

In slung loaded case, roll dynamics of the rotary wing air vehicle both for 2^{nd} and 3^{rd} order ADRCs are given in Figures 6.21a and 6.21b for the 20m flights, respectively. Pitch dynamics of the rotary wing air vehicle both for 2^{nd} and 3^{rd} order ADRCs are given in Figures 6.23a-6.23b for the 20m flight and Figures 6.24a-6.24b for the 40m flight. As can be seen in Figures from 6.21 to 6.24, roll and pitch dynamics are less oscillatory and peaks are relatively small with 3^{rd} order ADRC compared to 2^{nd} order ADRC for slung loaded case in 20m and 40m flights. There are steady state errors during the both 20m and 40m flights which are done with 2^{nd} order ADRC. These

steady-state errors can be seen in Figures 6.21a and 6.23a for roll and pitch dynamics during the 20m flight and Figures 6.22a and 6.24a during the 40m flight, respectively. 3^{rd} order ADRC has also better performance in eliminating the steady-state errors and following the command under stochastic disturbances. Flight data with the 3^{rd} order ADRC are shown in Figures 6.21b and 6.23b for roll and pitch dynamics during the 20m flight and Figures 6.22b and 6.24b during the 40m flight, respectively.

In the unloaded case, the only disturbance is the weather. The other cases include static and slung load beside the weather. Desired angles are calculated according to the rejection of these disturbances. As can be seen in Figure 6.25, errors of the slung load cases are the highest because more disturbance is applied to the rotary wing air vehicle. Nevertheless, it can be observed that both in static and slung load cases as well; disturbances can be rejected using an active disturbance rejection controller. It can be said that the performance of 3^{rd} order ADRC is better than the 2^{nd} order ADRC counterparts.

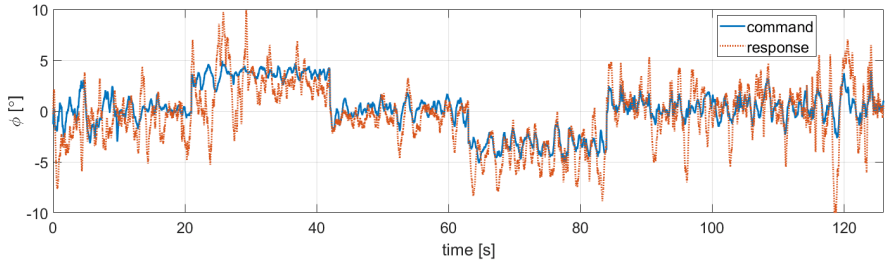

(a) Second Order ADRC results

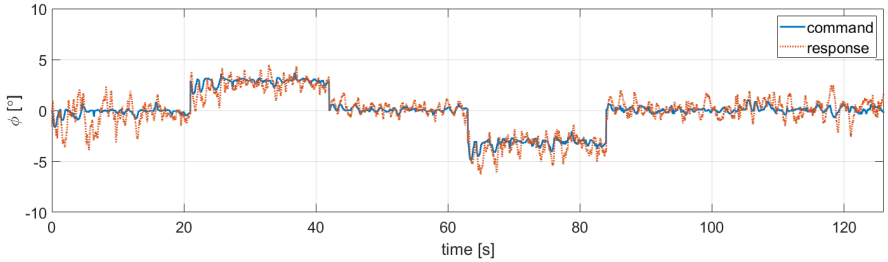

(b) Third Order ADRC results

Figure 6.21: Roll dynamics for slung loaded case - 20m flight

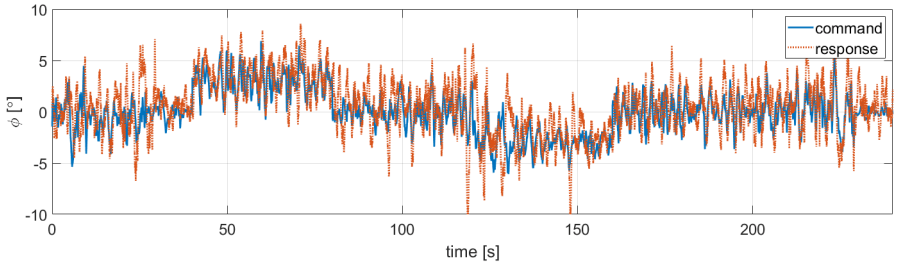

(a) Second Order ADRC results

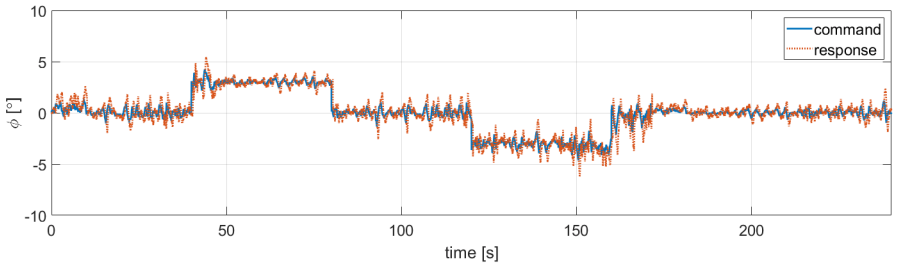

(b) Third Order ADRC results

Figure 6.22: Roll dynamics for slung loaded case - 40m flight

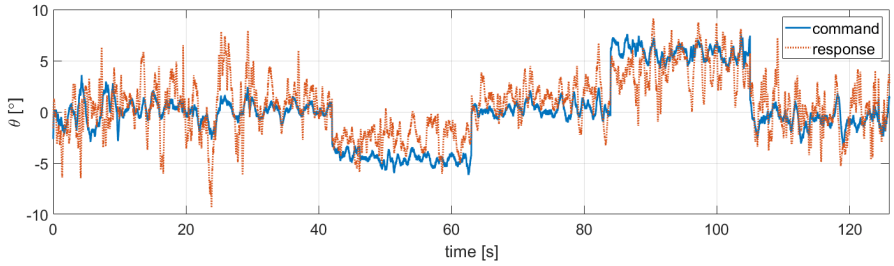

(a) Second Order ADRC results

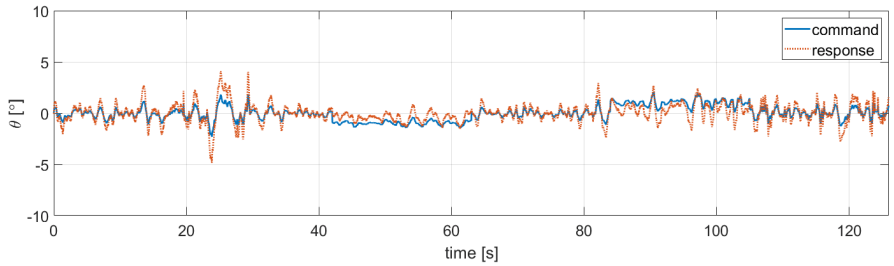

(b) Third Order ADRC results

Figure 6.23: Pitch dynamics for slung loaded case - 20m flight

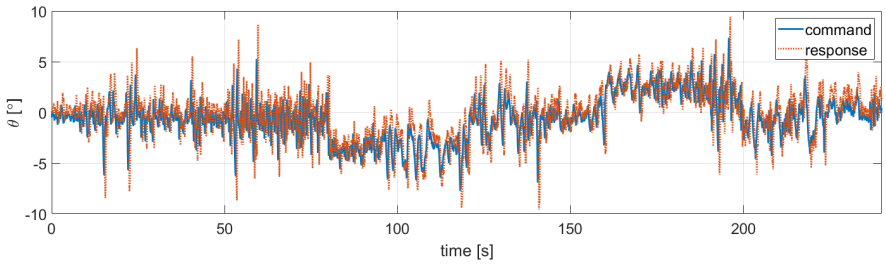

(a) Second Order ADRC results

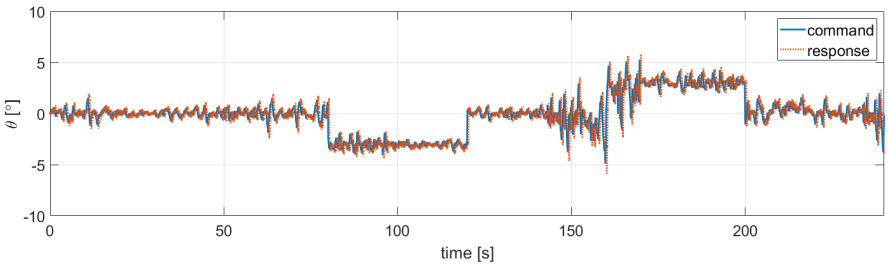

(b) Third Order ADRC results

Figure 6.24: Pitch dynamics for slung loaded case - 40m flight

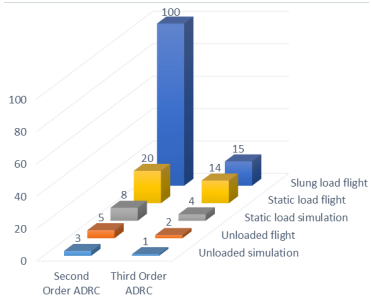

(a) Roll angle scaled ISE values for 20m flight

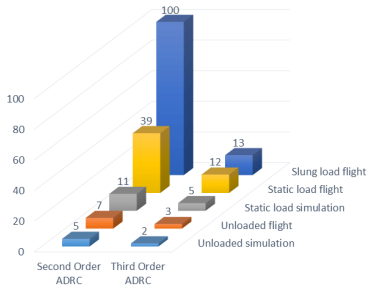

(b) Pitch angle scaled ISE values for 20m flight

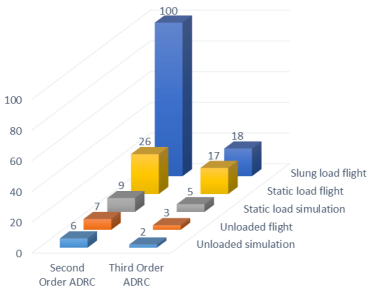

(c) Roll angle scaled ISE values for 40m flight

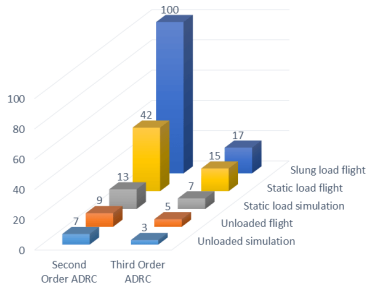

(d) Pitch angle scaled ISE values for 40m flight

Figure 6.25: Scaled ISE values for different controllers and flight cases

Table 6.3: Fixed wing air vehicle controller gains

Gain	**Roll**	**Pitch**
K_p	10	20
K_i	2	2
K_d	5	5

6.2 Fixed wing air vehicle

The fixed wing air vehicle is given in Figure 6.26. Roll and pitch dynamics of the fixed wing air vehicle are controller two separate PID controllers. **Aim of using fixed wing air vehicle** is to create the mainframe and a base for the **fixed wing VTOL air vehcile** in the sense of algorithms. Altitude and yaw angle are out of the scope of the test. PID controller gains can be seen in Table 6.3. Developed guidance and autopilot algorithm is developed in Matlab®/Simulink®environment and deployed to Pixhawk Cube controller card. The algorithm is developed such that the fixed wing air vehicle takes off from ground without an autopilot algorithm. During this part of the flight, the fixed wing air vehicle is controlled by the pilot from a remote controller on the ground. Controllers are activated when the fixed wing air vehicle is flying. Roll and pitch dynamic reference angle values adjusted from the remote controller as $\pm 10^{\circ}$ and $\pm 5^{\circ}$, respectively. Roll and pitch reference and system response values are seen in Figure 6.27 and Figure 6.28. At about 90^{th} second, autopilot is engaged, which is depicted as red lines. As can be seen, the controller performance of the pitch dynamic is better than the roll dynamic, which is caused by the gain parameters. Integral of the sum of squared errors is taken as given in Equation 6.2 to analyse the performance of the controller in roll and pitch axes of the fixed wing air vehicle. As can be seen in Table 6.4 performance of the pitch channel is better, smaller ISE value, than the roll channel that is caused by the controller gains.

Figure 6.26: Fixed wing air vehicle

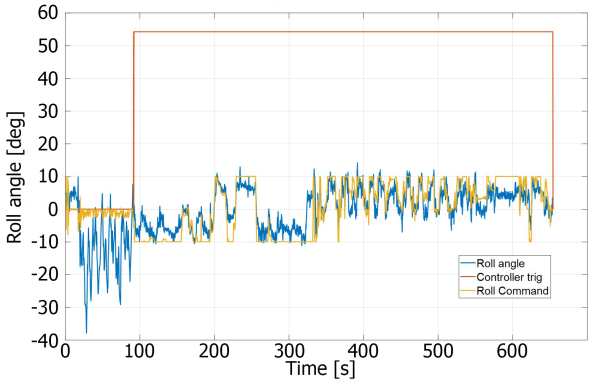

Figure 6.27: Flight test data - roll control

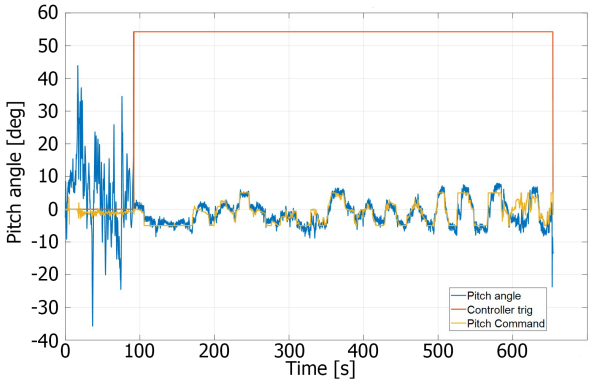

Figure 6.28: Flight test data - pitch control

Table 6.4: ISE values of the roll and pitch states

State	ISE value
Roll	15427
Pitch	8421

6.3 Fixed wing VTOL air vehicle

Since the fixed wing VTOL air vehicle is an over actuated system, using a control allocation algorithm is a must to have an efficient flight in terms of energy. As stated in Sections 4.2 and 4.3, fixed wing VTOL air vehicle is identified and modelled. The major step is to choose the control allocation algorithm. Fixed wing VTOL aircraft is simulated with the same scenario to investigate the performances of the control allocation algorithms. The flight is composed of five major phases which are take-off, the transition from rotary to fixed wing flight, level flight, transition from fixed wing to rotary wing flight, and landing. Control allocation algorithms are implemented in Matlab/Simulink environment, and performances of the algorithms are investigated. Obtained flight trajectories in XZ directions with different control allocation algorithms are given in Figure 6.32. Flight scenarios are ended when the fixed wing VTOL air vehicle touches the ground. Flowchart of the flight phases is given in Figure 6.29. Flight phases of the fixed wing VTOL air vehicle changes concerning comparisons of some values which are like if-else statement structure.

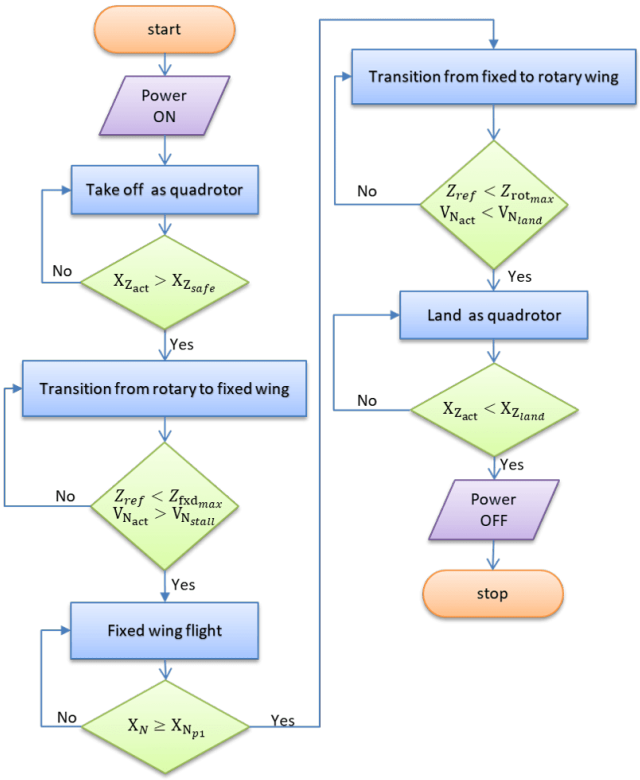

Figure 6.29: Flowchart of the flight phases

Algorithms run in transition phases are very important because the energy consumption of the fixed wing VTOL air vehicle is optimized in these phases. As stated in Section 5.3, control allocation algorithms distributes desired forces and moments to the available set of actuators which are brushless DC motors and servo motors. Each actuator has a position and rate limit. So, generated force/moments and generation speed is limited to hardware capabilities. Another critical point is the distribution of forces/moments at the steady-state. Inputs and outputs of the direct control allocation algorithm are given in Figure 6.30.

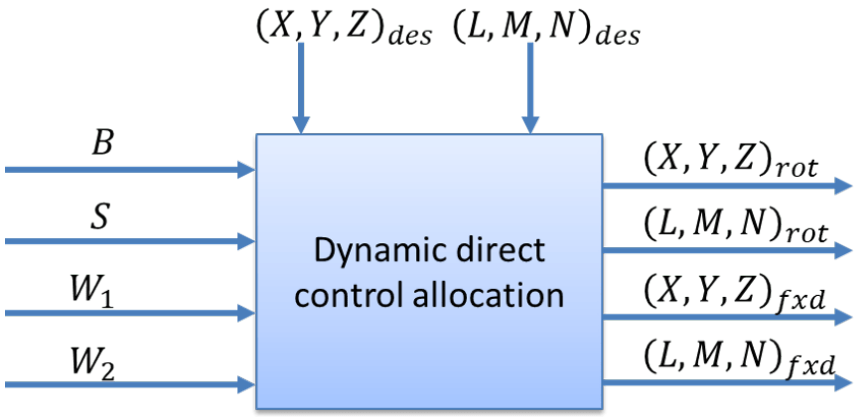

Figure 6.30: Dynamic control allocation inputs and outputs

where:

B	: control effectiveness matrix
S	: desired steady state distribution
W_1	: max/min position limits of actuators
W_2	: max/min rate limits of actuators
$(X,Y,Z)_{des}$	: desired forces from the controller
$(L,M,N)_{des}$	: desired moments from the controller
$(X,Y,Z)_{rot}$	: distribution of forces to the rotary wing
$(L,M,N)_{rot}$	: distribution of moments to the rotary wing
$(X,Y,Z)_{fxd}$	: distribution of forces to the fixed wing
$(L,M,N)_{rot}$	: distribution of moments to the fixed wing

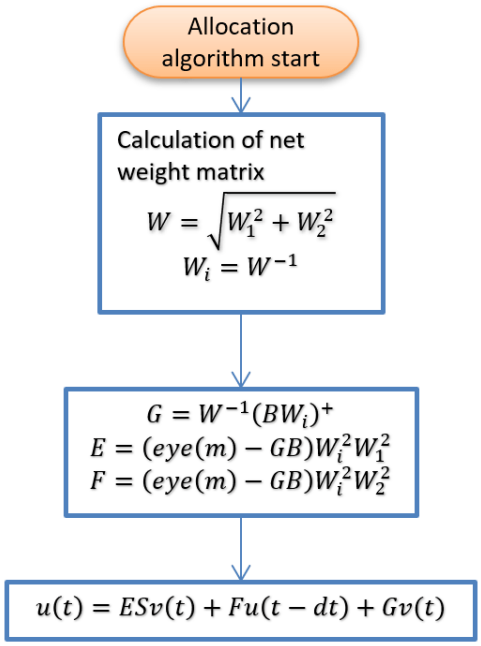

Figure 6.31: Architecture of direct control allocation algorithm

where:

W : net weighting matrix
W_i : inverse of net weighting matrix
$(.)^+$: Pseudo-inverse term
dt : sampling rate
m : number of inputs
$v(t)$: virtual input
$u(t)$: desired output

Flight times differ related to the control allocation algorithms. Positions and velocities of the fixed wing VTOL air vehicle are given in Figures 6.34 and 6.35 in the NED coordinate system, respectively. The same scenario and autopilot algorithms are used to see the performances and differences of the control allocation algorithms. As can be seen in Figure 6.32, different flight paths are obtained. Control allocation algorithm distributes the virtual input, which is the output of the controller to the available set of actuators in the limits of actuators. Distribution of the control allocation algorithms is different because of their speed of convergences and priorities

as given in Section 5.3. Power consumption of the fixed wing VTOL air vehicle is measured and compared to see the performance of the control allocation algorithms. Fixed wing VTOL air vehicle is composed of rotary and fixed wing parts.

Total consumed powers and their distributions to the rotary and the fixed wing parts are given in Figure 6.33. Flights phases are indicated as vertical dashed lines with numbers which are one is for take-off, two is for the transition from rotary wing to fixed wing flight, three is for level flight, four is for the transition from fixed wing to rotary wing flight, five is for landing. As can be seen in Figure 6.33, the least total consumed power for the fixed wing VTOL air vehicle is achieved with the dynamic direct allocation algorithm as given in Figure 6.33c.

There are two main advantages of using fixed wing VTOL air vehicles are that take-off and land in small areas with the rotary wing parts and longer flight ranges can be reached with the fixed wing parts. A scenario is designed to investigate the efficiency of the direct control allocation algorithm. There is a 0.2kg load attached underneath each wing. The fixed wing VTOL air vehicle carries and releases the left load at first, then takes off and carries the load that is under the right wing to the final point.

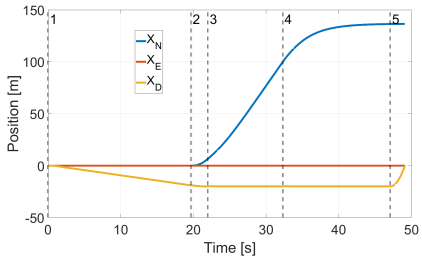

(a) Daisy chain

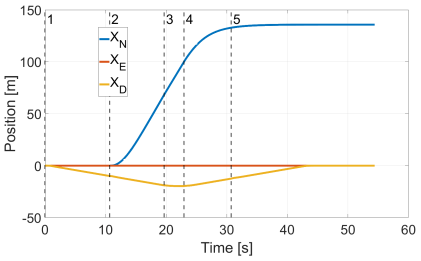

(b) Direct allocation

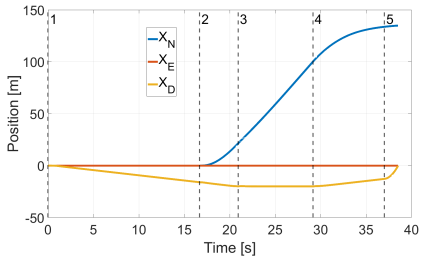

(c) Dynamic direct allocation

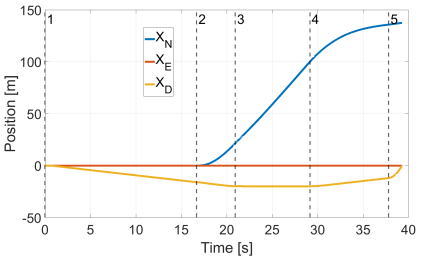

(d) Weighted least squared

Figure 6.34: Positions in NED coordinate system

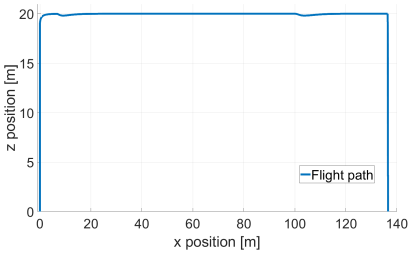

(a) Daisy chain

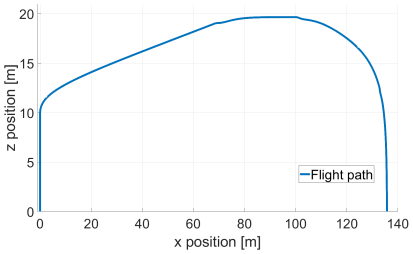

(b) Direct allocation

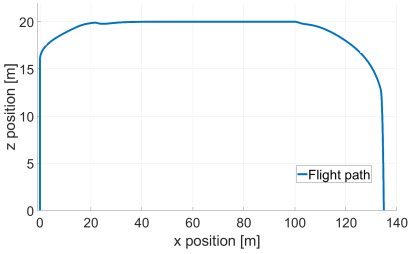

(c) Dynamic direct allocation

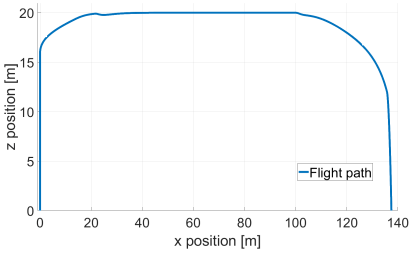

(d) Weighted least squared

Figure 6.32: XZ trajectories of different control allocation algorithms

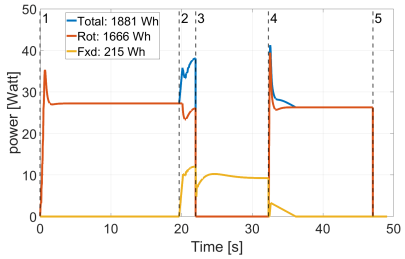

(a) Daisy chain

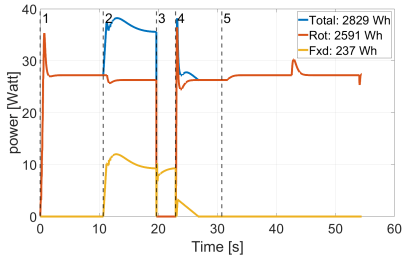

(b) Direct allocation

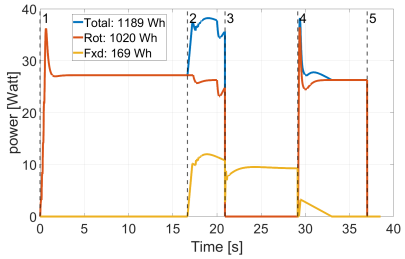

(c) Dynamic direct allocation

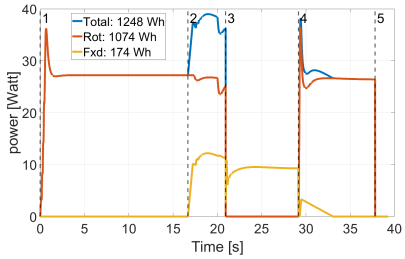

(d) Weighted least squared

Figure 6.33: Consumed powers of different control allocation algorithms

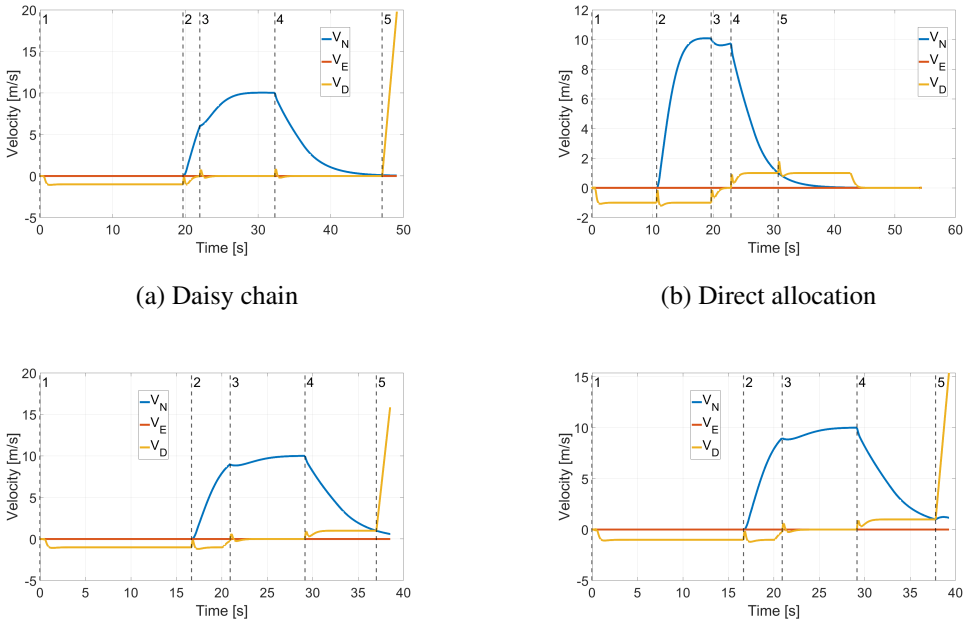

(a) Daisy chain

(b) Direct allocation

(c) Dynamic direct allocation

(d) Weighted least squared

Figure 6.35: Velocities in NED coordinate system

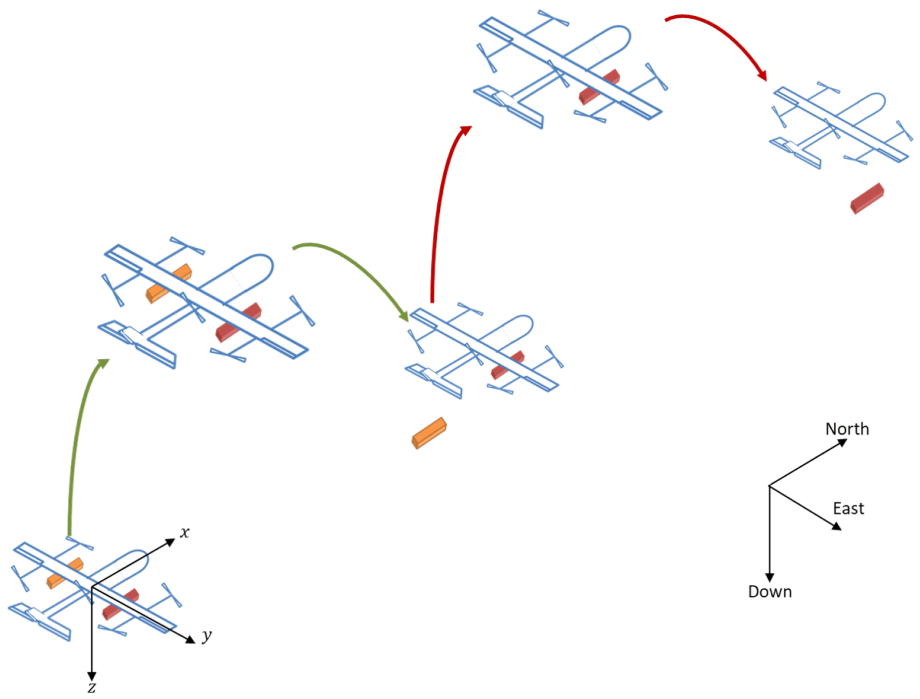

Figure 6.36: Fixed wing VTOL air vehicle flight scenario

Flight scenario of the fixed wing VTOL air vehicle is given in in Figure 6.36. Loads are represented as orange (left) and red (right) boxes. The fixed wing air vehicle completes the first flight section, which is represented as green arrows. Then, the left load (orange) is released. The mechanism and dynamic effects of the releasing process are not in the scope of this research. After the load is released, the second flight section starts, which are represented as red arrows. In the second flight section, fixed wing VTOL air vehicle is loaded with asymmetrically. In the scenario, reference altitude is 20m. and cruising speed is 10m/s. Flight trajectories in three dimensional space are given in Figure 6.37. Positions in the NED coordinate system are given in Figure 6.38. First and second flight sections are represented as numbered green dashed and red dotted vertical lines. In the NED coordinate system, negative Z direction is upwards, which means higher altitude. That is why the altitude of the fixed wing VTOL air vehicle, X_D, in Figure 6.34 is negative. In the first flight phase (green), the fixed wing VTOL air vehicle takes off vertically, so velocities in North and East directions are zero so the positions. Second flight phase is the transition from rotary wing to fixed wing, so the velocity in North direction increases to the cruising speed. After the stall speed is passed, the third flight phase started. At the same time, the reference altitude is reached. So, the horizontal speed V_N increases to the cruising speed as the vertical speed V_D approaches to zero.

Euler angles of the fixed wing VTOL air vehicle is given in Figure 6.40. Reference Euler angles during the whole flight are zero in roll, pitch, and yaw states. As can be seen in Figure 6.40, Euler angles are zero during the first flight section (green dashed lines). In the second flight section, the load under the right wing, given as a red box in Figure 6.36, behaves as a constant *disturbance* to the system. Similar case is investigated, simulated, and tested on rotary wing air vehicle which is given in Section 6.1.3, 4^{th} and 10^{th} flight numbers in Table 6.1. Effects of the load to the rotational dynamics of the fixed wing VTOL air vehicle can be seen in a second flight section whose sections are represented as red dotted vertical lines. In the first phase of the second flight section, fixed wing air vehicle takes off with one load underneath the right wing, as seen in Figure 6.36.

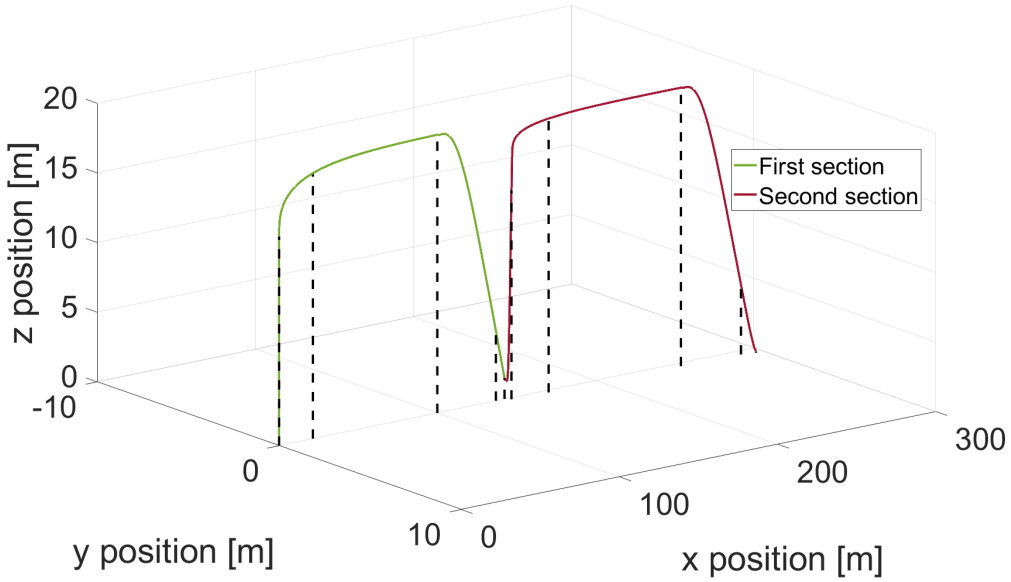

Figure 6.37: Fixed wing VTOL air vehicle flight path

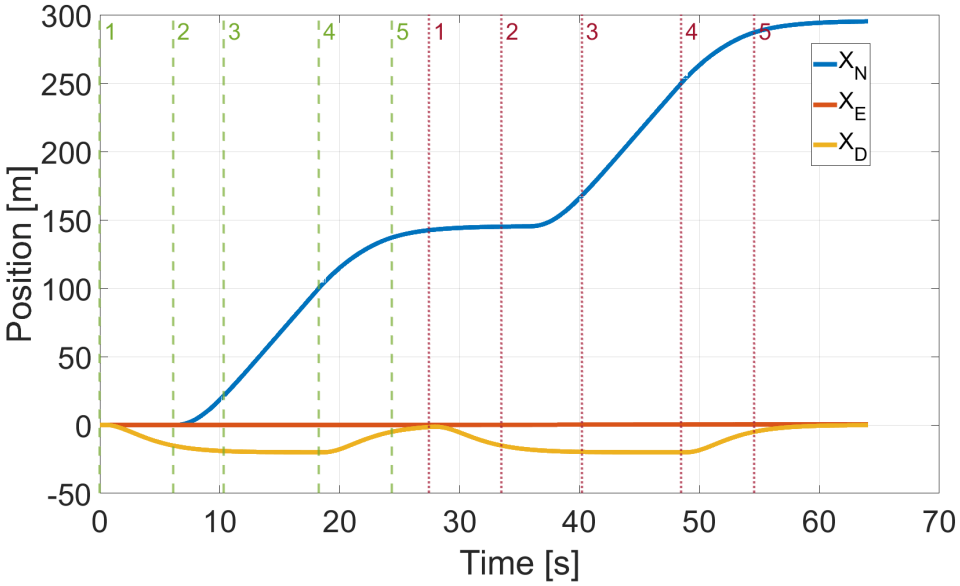

Figure 6.38: Fixed wing VTOL air vehicle positions in NED coordinate frame

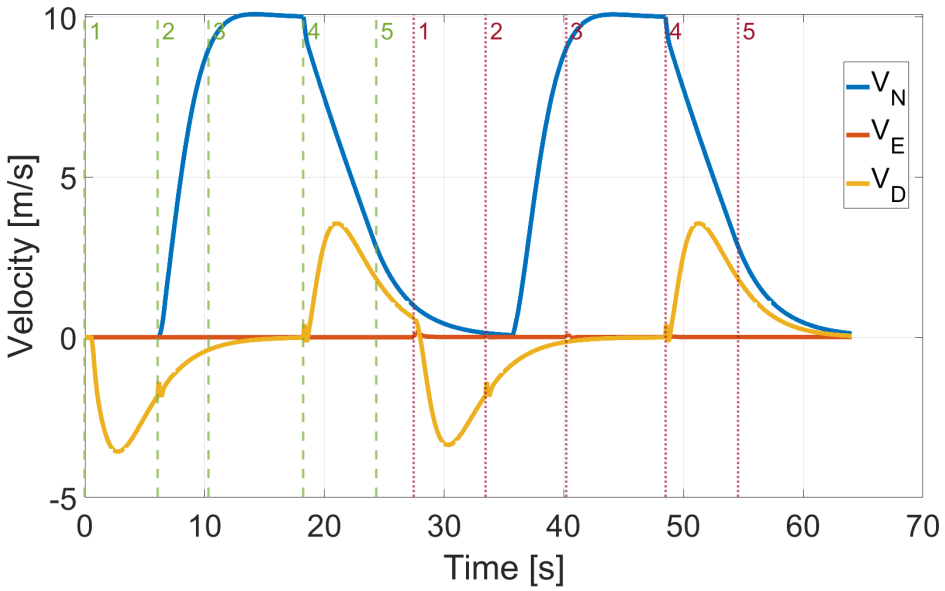

Figure 6.39: Fixed wing VTOL air vehicle velocities in NED coordinate frame

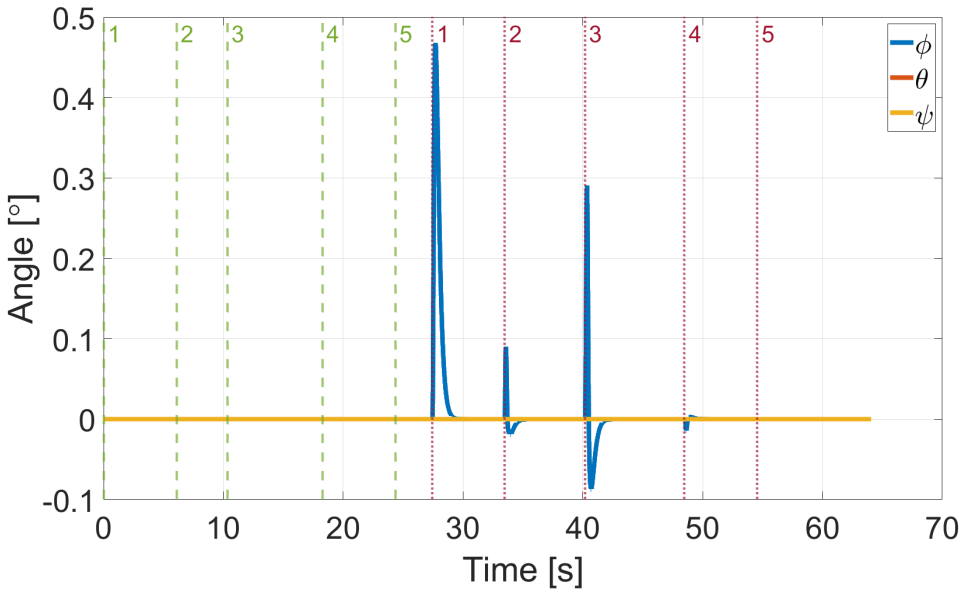

Figure 6.40: Fixed wing VTOL air vehicle Euler angles

Controllers generate desired forces and moments which are called as virtual commands to reject the disturbances and hold the states in reference values. Control allocation algorithm distributes the virtual commands to the available set of actuators as given in Figure 5.6. Distributed forces and moments after the control allocation

algorithm are seen in Figure 6.41.

Forces in x direction are given in Figure 6.41a. Required force in x direction is provided by fixed wing VTOL air vehicle. Since the take-off and landing are done vertically, required and distributed force in x direction are zero, which can be seen in first and fifth flight phases for both flight sections. Second flight phases, speed of the fixed wing VTOL air vehicle is increased to reach the cruising speed. After the stall speed is passed, required x force becomes constant. In the fourth state, the required force goes to zero since the reference speed is zero. Forces in y direction are zero during the flight because no lateral motion is taken into account, which is given in Figure 6.41c. In z direction, required forces are provided by rotary wing air vehicle in first flight phases. For the second flight phases, rotary wing allocation decreases while fixed wing increases. In the third phase, all lift force is generated by fixed wings. For landing, in state 4, most of the required force generated by rotary wings. In second and fourth phases, the allocation for the fixed wing part is limited because the speed of the fixed wing VTOL air vehicle is slower than the stall speed as can be seen in Figure 6.41e.

Roll moment is constant during the first flight section. After the load placed in the left wing is released, the load in the right wing contributes a constant positive roll moment. Fixed wing air vehicle generates a counter moment to balance the moment comes from the load in the right wing. In Figure 6.41b, generated counter moment is seen in the second flight phase. Required pitch and yaw moments are zero during the whole flight as given in Figures 6.41d and 6.41f.

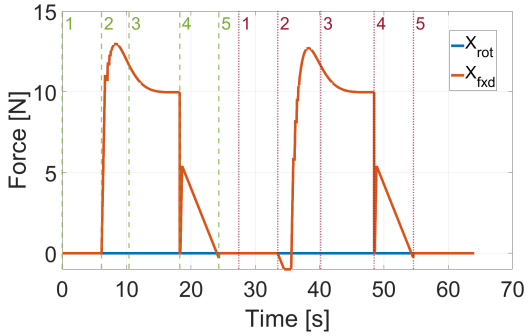

(a) Body force distribution in x direction

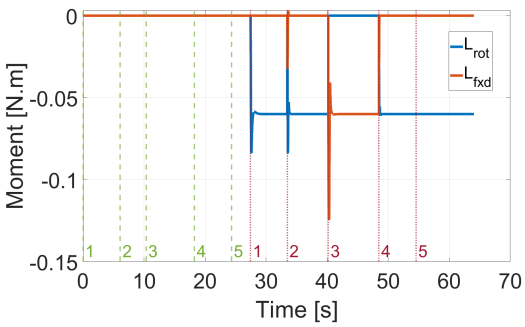

(b) Roll moment distribution

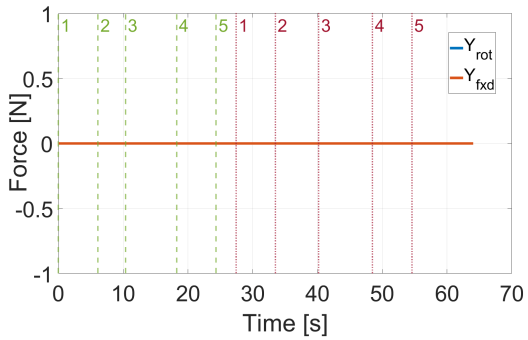

(c) Body force distribution in y direction

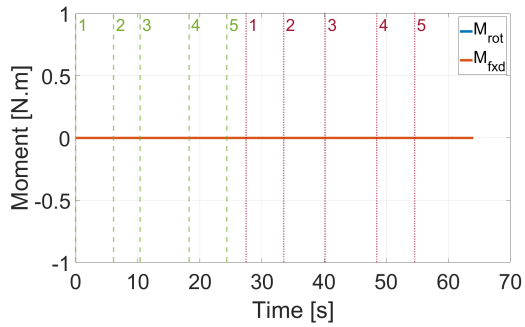

(d) Pitch moment distribution

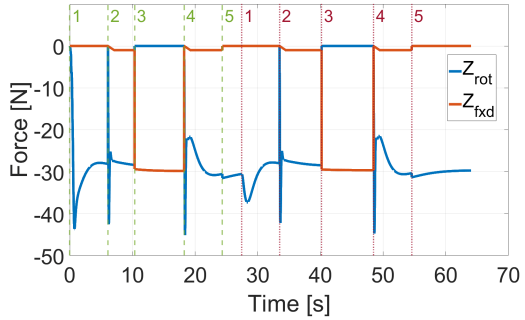

(e) Body force distribution in z direction

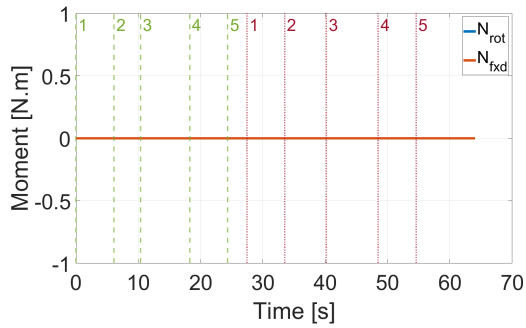

(f) Yaw moment distribution

Figure 6.41: Force and moment distributions

For the power consumption, rotary and fixed wing parts are investigated separately and then combined. Needed current to generate a certain amount of force is measured in Section 4.2.2 due to a constant voltage level.

Rotary wing parts of the fixed wing VTOL air vehicle is used to generate a lift force in the first flight section. So, each motor consumes the same amount of power. In the first

phase, they are used to generate a lift force to take off. In the second phase, generated lift force from the rotary wing parts decreased slightly, but still, it generates the most of the required lift force. The reason is, the speed of the fixed wing air vehicle is slower than the stall speed. In the third phase, rotary wings stop, and no power is consumed. In the phase from fixed wing to rotary wing, which is phase 4, they operate again. Landing is carried out with the rotary wing parts. In the second phase of the flight, because of the load placed underneath of the right wing, rotary wing motors do not rotate in the same speed to generate the counter moment to balance the fixed wing VTOL air vehicle. Power consumption of the rotary wing part is given in Figure 6.42.

Actuators of the fixed wing part are servo motors and a brushless DC motor. Servo motors are used to actuate the control surfaces, which are ailerons, elevator, and rudder. Power consumption of the servo motors is neglected because it is minimal relative to the brushless DC motor. Consumed power in motor numbered as 5 in Figure 4.3, which is used to generate horizontal thrust force is considered and given in Figure 6.43. As opposed to the rotary wings, motor 5 runs in state 2 and 3, which are transitions from rotary to fixed wing and level flights. In the fourth phase, it slows down and stops.

Power consumption of the fixed wing VTOL air vehicle is given in Figure 6.44. As stated in Section 4.2, relation among thrust units and reference PWM signal is identified. During the tests, consumed current according to the reference PWM signal is measured, and the operating voltage is constant. So, consumed power of all thrust units are known related to reference PWM signal.

The first phase in the first flight section, power is only consumed by rotary wings. In the second phase, motor 5 starts to rotate so consumes energy. In the third phase, the required power is consumed by fixed wings. In the fourth phase, motor 5 slows down, so its consumed power and rotary wings start to rotate. In the second flight section, one of the load is released, so consumed powers both in rotary and fixed wing sections are relatively less to the first flight section.

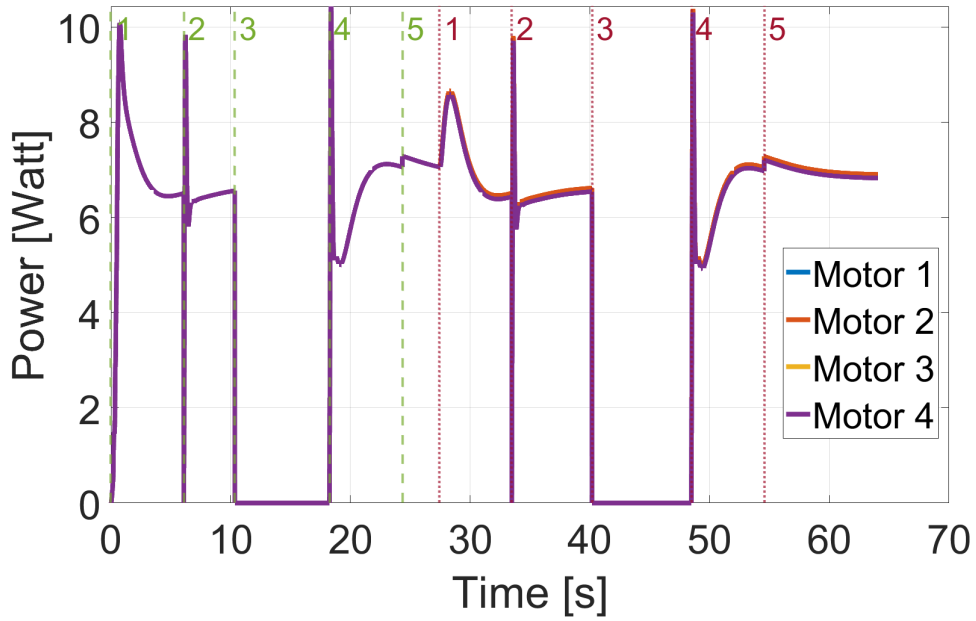

Figure 6.42: Power consumption of rotary wings of fixed wing VTOL air vehicle

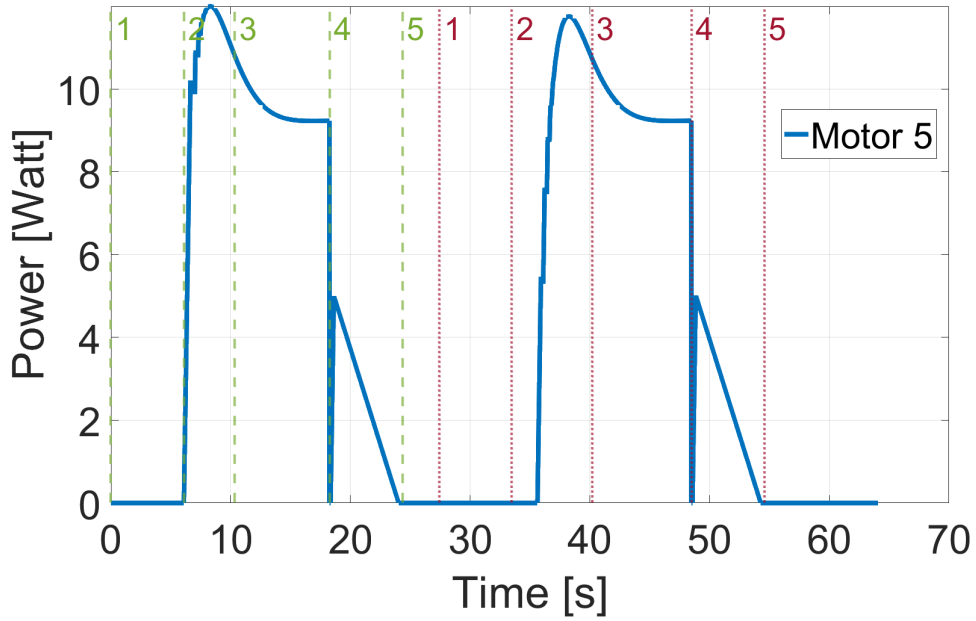

Figure 6.43: Power consumption of fixed wings of fixed wing VTOL air vehicle

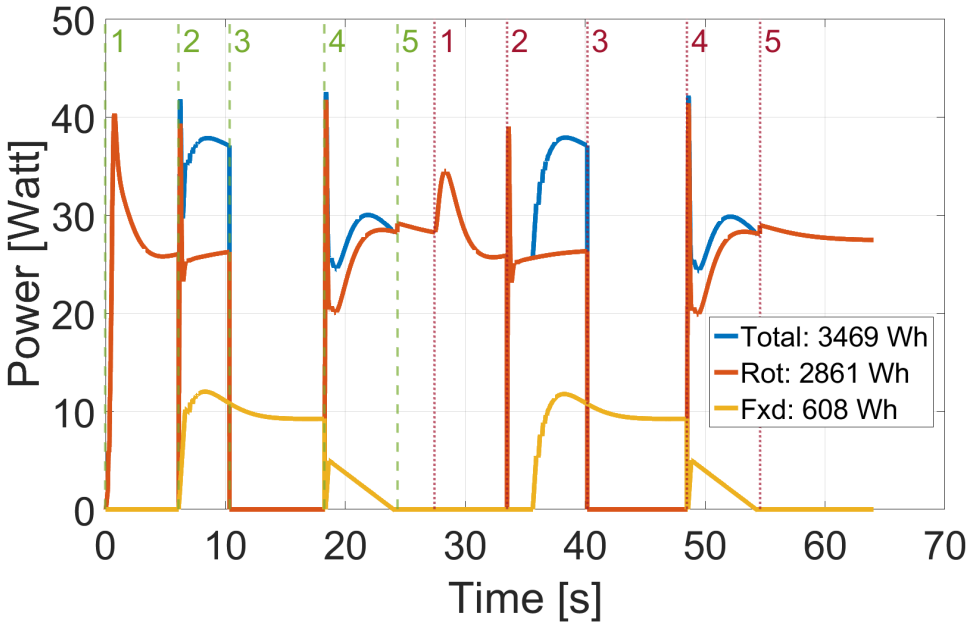

Figure 6.44: Power consumption of fixed wing VTOL air vehicle

Another important point that needs to be considered is the physical limits of the actuators of the fixed wing VTOL air vehicle. As stated in Section 4.2, servo motors are used in control surfaces, and brushless DC motors are used both in vertical and horizontal thrusters. Rotational position limits and positions of the control surfaces are given in Figure 6.45. Forward and reverse position limits are depicted as horizontal blue lines. During the system identification tests, forward and reverse limits of the control surfaces of the fixed wing VTOL air vehicle are measured as $\pm 15°$. Rotational positions of the control surfaces during the scenario are in the hardware limits. Vertical thrusters are also work in the hardware limits. Rotational velocities of the vertical thrusters and hardware limits are seen in Figure 6.46.

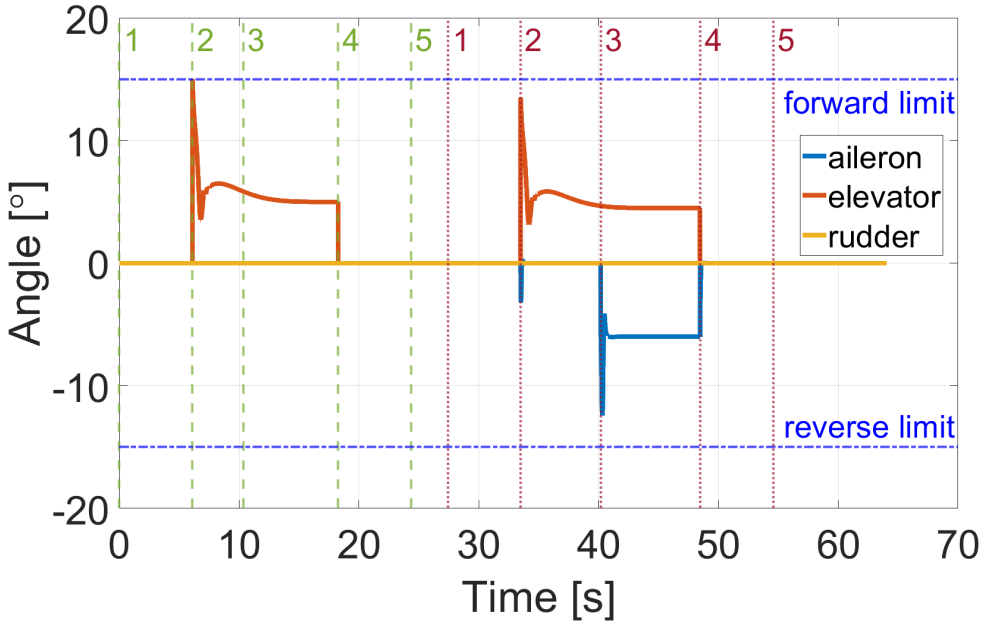

Figure 6.45: Control surface positions of fixed wing VTOL air vehicle

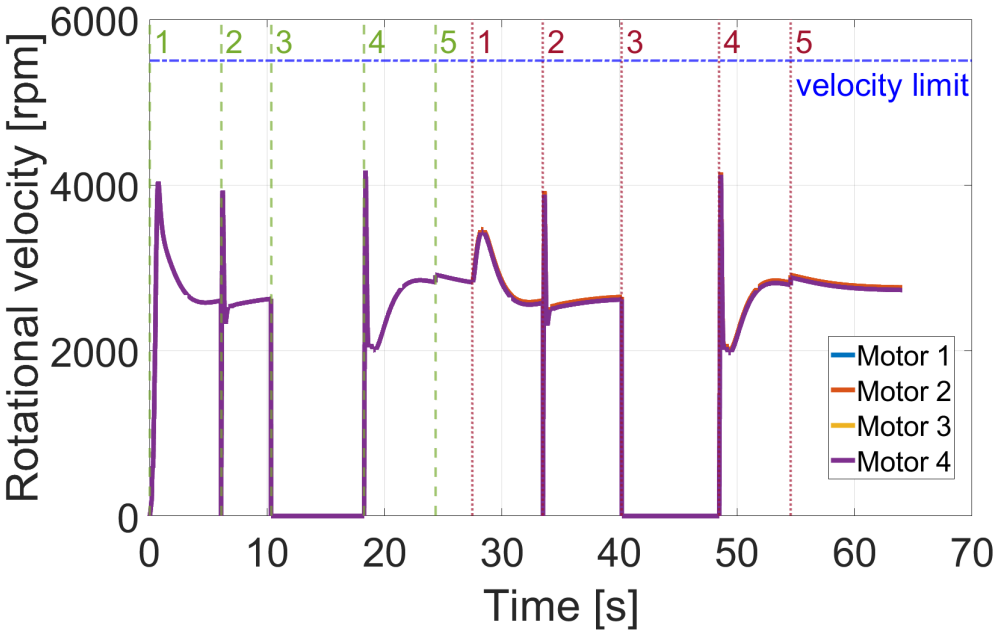

Figure 6.46: Vertical thrusters' velocities of fixed wing VTOL air vehicle

CHAPTER 7

CONCLUSION

The motivation of this study is to merge the advantages of rotary and fixed wing air vehicles in one platform, which is called as a fixed wing VTOL air vehicle. It can take-off and land vertically and fly interminable distances compared to the rotary wing air vehicles. In our daily life, unmanned fixed and rotary wings are widely used in many civil and military applications. New needs arise with the developed technologies in material, electronic, and software areas. New designs come with more complex structures and the need for efficiency.

In this study, it is aimed to develop efficient guidance, autopilot, and control algorithm without sacrificing the performance of the fixed wing VTOL air vehicle. To do that, the fixed wing VTOL air vehicle is separated into two air vehicles such as rotary and fixed wing. ADRC, a well-known controller algorithm, is designed and combined with a trajectory tracking algorithm. The developed system is tested under different load conditions such as unloaded, asymmetric constant load and a slung load. Flight tests prove that the algorithms in controlling the rotary wing air vehicle as well as rejecting the unknown disturbances during the flight. Another step is to model and design a control algorithm for a fixed wing air vehicle. Designed algorithms are verified with the flight tests. The final step is to design an efficient algorithm for the fixed wing VTOL air vehicle. The most critical sections are the transitions among vertical and horizontal flights. Control allocation algorithms are investigated and applied to the system to reduce power consumption during transition phases. Developed algorithms are tested in a simulation environment, and efficiency is proved.

Besides the above studies, a real scenario is designed to see the performance of the designed system. The scenario may be possible in daily life, for example, medicine

transportation in earthquake rubble. Besides, weaponized unmanned air vehicles loaded symmetrically at the beginning of a mission. After one ammunition is released, asymmetric load condition occurs. Developed algorithms are proved in scenario results both in efficiency and performance.

A fixed wing VTOL air vehicle is developed physically. It was planned to complete the flight tests with the fixed wing VTOL air vehicle after the rotary and fixed wing air vehicles. The material of the main wing is foam. Because of its flexible structure, rotary wing air vehicle part does not behave as a rigid body. Though it is hardened with a rod, there is a twist in the main wing while the rotary wing motors try to hold the attitude. Some rods can be placed among rotary wing motors parallel to the main wing, and results can be verified with flight tests.

Power consumption of the fixed wing VTOL air vehicle is given in Figure 6.44. The first phase in the first flight section, power is only consumed by rotary wings. In the second phase, motor 5 starts to rotate so consumes energy. In the third phase, the required power is consumed by fixed wings. In the fourth phase, motor 5 slows down so its consumed power and rotary wings start to rotate. In the second flight section, one of the load is released, so consumed powers both in rotary and fixed wing sections are relatively less to the first flight section.

REFERENCES

[1] F. Gao, S. Wang, Y. Wu, G. Zhao, B. Wang, and J. Hu, "A novel inverse method for automatic uav line patrolling with magnetic sensors," pp. 481–485, 05 2018.

[2] T. Thaden, "Social informatics and aviation technology," *Bulletin of the American Society for Information Science and Technology*, vol. 26, pp. 13 – 14, 02 2005.

[3] W. E. Green and P. Y. Oh, "A fixed-wing aircraft for hovering in caves, tunnels, and buildings," in *2006 American Control Conference*, pp. 6 pp.–, 2006.

[4] "The wright brothers." `https://airandspace.si.edu/exhibitions/wright-brothers/online/`. Accessed: May 2020.

[5] "World's first helicopter." `https://connecticuthistory.org/worlds-first-helicopter-today-in-history`. Accessed: May 2020.

[6] "Choosing a fixed wing drone." `https://www.heliguy.com/blog/2016/03/01/choosing-fixed-wing-drone`. Accessed: May 2020.

[7] P.-M. Basset, A. Tremolet, and T. Lefebvre, "Rotary wing uav pre-sizing : Past and present methodological approaches at onera," 01 2014.

[8] M. A. Boon, A. P. Drijfhout, and S. Tesfamichael, "Comparison of a fixed-wing and multi-rotor uav for environmental mapping applications: A case study," *ISPRS - International Archives of the Photogrammetry, Remote Sensing and Spatial Information Sciences*, vol. XLII-2/W6, pp. 47–54, 2017.

[9] M. Heaphy, M. Watt, J. Dash, and G. Pearse, "Uavs for data collection-plugging the gap," *New Zealand Journal of Forestry*, vol. 62, pp. 23–30, 04 2017.

[10] A. Joshi, A. Tripathi, and R. N. Ponnalgu, "Modelling and design of a hybrid aerial vehicle combining vtol capabilities with fixed wing aircraft," in *2019 6th*

International Conference on Instrumentation, Control, and Automation (ICA), pp. 47–51, 2019.

[11] M. Tielin, Y. Chuanguang, G. Wenbiao, X. Zihan, Z. Qinling, and Z. Xiaoou, "Analysis of technical characteristics of fixed-wing vtol uav," in *2017 IEEE International Conference on Unmanned Systems (ICUS)*, pp. 293–297, 2017.

[12] R. Austin, *Unmanned Aircraft Systems: UAVS Design, Development and Deployment*. John Wiley and Sons Ltd.

[13] F. Çakıcı and M. K. Leblebicioğlu, "Design and analysis of a mode-switching micro unmanned aerial vehicle," *International Journal of Micro Air Vehicles*, vol. 8, no. 4, pp. 221–229, 2016.

[14] M. R. Cabello, S. Fernández, M. Pous, E. Pascual-Gil, L. D. Angulo, P. López, P. J. Riu, G. G. Gutierrez, D. Mateos, D. Poyatos, M. Fernandez, J. Alvarez, M. F. Pantoja, M. Añón, F. Silva, A. R. Bretones, R. Trallero, L. Nuño, D. Escot, R. G. Martin, and S. G. Garcia, "Siva uav: A case study for the emc analysis of composite air vehicles," *IEEE Transactions on Electromagnetic Compatibility*, vol. 59, no. 4, pp. 1103–1113, 2017.

[15] R. P. Supriyono, D. Danardono, and E. P. Budiana, "Cooling load calculation for electric vehicle with composite body using cltd/scl/clf method," in *2013 Joint International Conference on Rural Information Communication Technology and Electric-Vehicle Technology (rICT ICeV-T)*, pp. 1–3, 2013.

[16] "Drone autopilot system with the best drone app.." `https://dronee.aero/pages/cockpit`. Accessed: Sept. 2019.

[17] "Navio2 overview." `https://ardupilot.org/copter/docs/common-navio2-overview.html`. Accessed: Sept. 2019.

[18] "Beaglebone blue." `https://docs.px4.io/v1.9.0/en/flight_controller/beaglebone_blue.html`. Accessed: May. 2020.

[19] "Micropilot - world leader in professional uav autopilots." `https://www.micropilot.com/product-tour-uav-autopilots-01.htm`. Accessed: May. 2020.

[20] "Hex cube (pixhawk 2)." https://docs.px4.io/v1.9.0/en/flight_controller/pixhawk-2.html. Accessed: May. 2020.

[21] R. Behinfaraz and A. R. Ghiasi, "A survey on reliability analysis in controller design," in *2018 IEEE 14th International Colloquium on Signal Processing Its Applications (CSPA)*, pp. 198–202, March 2018.

[22] N. Koyama, K. Kubota, I. Kitamuki, M. Nitta, and K. Kato, "Survey of a controller design method based on experimental data and a proposal of data conversion method," in *2012 12th International Conference on Control, Automation and Systems*, pp. 873–877, Oct 2012.

[23] D. Jouve, J. P. Rognon, and D. Roye, "Effective current and speed controllers for permanent magnet machines: a survey," in *Fifth Annual Proceedings on Applied Power Electronics Conference and Exposition*, pp. 384–393, March 1990.

[24] S. Khatoon, M. Shahid, Ibraheem, and H. Chaudhary, "Dynamic modeling and stabilization of quadrotor using pid controller," in *2014 International Conference on Advances in Computing, Communications and Informatics (ICACCI)*, pp. 746–750, Sep. 2014.

[25] M. A. Kiyashko, A. K. Sholmov, and A. A. Efremov, "Quadrotor mathematical and information model analysis," in *2017 IEEE Conference of Russian Young Researchers in Electrical and Electronic Engineering (EIConRus)*, pp. 901–904, Feb 2017.

[26] A. Zulu and S. John, "A review of control algorithms for autonomous quadrotors," *CoRR*, vol. abs/1602.02622, 2016.

[27] D. Matouk, O. Gherouat, F. Abdessemed, and A. Hassam, "Quadrotor position and attitude control via backstepping approach," in *2016 8th International Conference on Modelling, Identification and Control (ICMIC)*, pp. 73–79, Nov 2016.

[28] B. Lotfi, M. Goharimanesh, and L. Huang, "Modelling and control of quadrotor maneuvers with variations of center of gravitry (cog)," in *2015 IEEE International Conference on Advanced Intelligent Mechatronics (AIM)*, pp. 1570–1574, July 2015.

[29] E. Ekawati, A. Widyotriatmo, and I. Askandari, "Quadrotor position control based on model identification and proportional-derivative algorithm," in *2014 2nd International Conference on Technology, Informatics, Management, Engineering Environment*, pp. 169–173, Aug 2014.

[30] A. S. Onen, L. Cevher, M. Senipek, T. Mutlu, O. Gungor, I. O. Uzunlar, D. F. Kurtulus, and O. Tekinalp, "Modeling and controller design of a vtol uav," in *2015 International Conference on Unmanned Aircraft Systems (ICUAS)*, pp. 329–337, 2015.

[31] O. Tekinalp, A. T. Kutay, D. Kaya, D. F. Kurtulus, I. Simsek, S. Soysal, and G. Hosgit, *Propulsion System Selection and Modeling for a Quadrotor with Search and Rescue Mission*.

[32] H. Çakır and D. Kurtulus, "Hovering control of a tilt-wing uav," 09 2019.

[33] J. Han, "From pid to active disturbance rejection control," *IEEE Transactions on Industrial Electronics*, vol. 56, pp. 900–906, 2009.

[34] S. Zhonghua, "Design and simulation of naval gun servo controller based on adrc," in *2019 11th International Conference on Measuring Technology and Mechatronics Automation (ICMTMA)*, pp. 345–349, 2019.

[35] Shiqi Zhao, Hejin Xiong, Junjie Chang, and Jian Fu, "The adrc and simulation of pitching angle for unmanned aerial vehicles," in *2015 Chinese Automation Congress (CAC)*, pp. 427–430, 2015.

[36] H. Duan, K. W. Han, Y. Zhang, and Y. Tian, "Control for ball and plate system based on rbf-adrc," in *2012 IEEE International Conference on Mechatronics and Automation*, pp. 434–439, 2012.

[37] Y. Han and R. Geng, "Active disturbance rejection control of underwater high-speed vehicle," in *2012 IEEE International Conference on Automation and Logistics*, pp. 550–553, 2012.

[38] M. Aydemir and K. Arikan, "Evaluation of the disturbance rejection performance of an aerial manipulator," *Journal of Intelligent and Robotic Systems*, 04 2019.

[39] A. N. Wan, G. M. S. Sim, R. W. L. Koh, R. K. F. Koh, G. T. Teo, T. H. Yap, T. Nilju, S. Srigrarom, F. Holzapfel, V. Marvakov, P. Bhadwaj, S. Tantrairatn, and S. Sakulthong, "Development of ugs-tum vertical take off landing (vtol) drone with flight control," in *2019 First International Symposium on Instrumentation, Control, Artificial Intelligence, and Robotics (ICA-SYMP)*, pp. 213–221, 2019.

[40] J. Apkarian, "Attitude control of pitch-decoupled vtol fixed wing tiltrotor," in *2018 International Conference on Unmanned Aircraft Systems (ICUAS)*, pp. 195–201, 2018.

[41] J. Liang, Q. Fei, B. Wang, and Q. Geng, "Tailsitter vtol flying wing aircraft attitude control," in *2016 31st Youth Academic Annual Conference of Chinese Association of Automation (YAC)*, pp. 439–443, 2016.

[42] Z. Zaludin and E. Gires, "Automatic flight control requirements for transition flight phases when converting long endurance fixed wing uav to vtol aircraft," in *2019 IEEE International Conference on Automatic Control and Intelligent Systems (I2CACIS)*, pp. 273–278, 2019.

[43] J. k. Gunarathna and R. Munasinghe, "Development of a quad-rotor fixed-wing hybrid unmanned aerial vehicle," in *2018 Moratuwa Engineering Research Conference (MERCon)*, pp. 72–77, 2018.

[44] "Arcturus uav." https://arcturus-uav.com/. Accessed: May. 2020.

[45] "Alti - the world's best endurence vtol air vehicle fleet." https://www.altiuas.com/. Accessed: May. 2020.

[46] "Cgt50 uav." https://ivmeihs.com/cgt50/. Accessed: May. 2020.

[47] J. Leško, M. Schreiner, D. Megyesi, and L. Kovács, "Pixhawk px-4 autopilot in control of a small unmanned airplane," in *2019 Modern Safety Technologies in Transportation (MOSATT)*, pp. 90–93, Nov 2019.

[48] L. Meier, P. Tanskanen, F. Fraundorfer, and M. Pollefeys, "Pixhawk: A system for autonomous flight using onboard computer vision," in *2011 IEEE International Conference on Robotics and Automation*, pp. 2992–2997, May 2011.

[49] A. D. Team, "Mission planner." https://ardupilot.org/planner/. Accessed: May. 2020.

[50] QGroundControl, "Qgc-qgroundcontrol." http://qgroundcontrol.com/. Accessed: May. 2020.

[51] P. D. Team, "Cube flight controller." https://dev.px4.io/v1.9.0/en/log/logging.html. Accessed: May. 2020.

[52] Z. Mustapa, S. Saat, S. H. Husin, and T. Zaid, "Quadcopter physical parameter identification and altitude system analysis," in *2014 IEEE Symposium on Industrial Electronics Applications (ISIEA)*, pp. 130–135, Sep. 2014.

[53] C. Ma, M. Z. Q. Chen, J. Lam, and K. C. Cheung, "Joint unscented kalman filter for dual estimation in a bifilar pendulum for a small uav," in *2015 10th Asian Control Conference (ASCC)*, pp. 1–6, May 2015.

[54] M. Saedan and P. Puangmali, "Characterization of motor and propeller sets for a small radio controlled aircraft," in *2015 10th Asian Control Conference (ASCC)*, pp. 1–6, May 2015.

[55] D. Shatat and T. A. Tutunji, "Uav quadrotor implementation: A case study," in *2014 IEEE 11th International Multi-Conference on Systems, Signals Devices (SSD14)*, pp. 1–6, Feb 2014.

[56] Yongxi Lyu, Weiguo Zhang, Jingping Shi, Xiaobo Qu, and Jun Che, "Post stall maneuver control of advanced fighter considering the unsteady aerodynamics," in *2016 IEEE Chinese Guidance, Navigation and Control Conference (CGNCC)*, pp. 1193–1199, Aug 2016.

[57] "Xflr5." http://www.xflr5.tech/xflr5.htm. Accessed: May. 2020.

[58] Y. Wang, Y. Zhao, G. Xia, A. Qiu, Q. Shi, and R. Liu, "A scale factor self-calibration method for a batch of mems gyroscopes based on virtual coriolis force," in *2018 14th IEEE International Conference on Solid-State and Integrated Circuit Technology (ICSICT)*, pp. 1–3, 2018.

[59] B. Etkin, *Dynamics of Atmospheric Flight*. Dover Books on Aeronautical Engineering, Dover Publications, 2012.

[60] H. H. Liu, "Fixed-wing dynamics and control." https://static1.squarespace.com/static/56e4a24bc6fc082c7577a416/t/5718f7377da24fd2759818bd/1461253948078/Hugh_AER_1216_lecture.pdf, Feb. 2016.

[61] A. Guclu, D. Kurtulus, and K. Arikan, "Hybrid stabilization of attitude dynamics of a fixed and rotary wing air vehicle," *SUHAD*, vol. 1, p. 65–73, 05 2016.

[62] A. Guclu, D. F. Kurtulus, and K. B. Arikan, *Attitude and Altitude Stabilization of Fixed Wing VTOL Unmanned Air Vehicle*.

[63] A. Guclu, "Attitude and altitude control of an outdoor quadrotor."

[64] W. Chenlu, C. Zengqiang, S. Qinglin, and Z. Qing, "Design of pid and adrc based quadrotor helicopter control system," in *2016 Chinese Control and Decision Conference (CCDC)*, pp. 5860–5865, May 2016.

[65] A. Guclu, K. Arikan, and D. Kurtulus, "Hibrit hava aracı yükseklik ve yönelim dinamiklerinin Çok girdili Çok Çıktılı doğrusal aktif bozucu savurucu ile denetimi," in *TOK2018 Otomatik Kontrol Ulusal Toplantısı*, 09 2018.

[66] G. Zhu, J. Qi, and C. Wu, "Landing control of fixed-wing uav based on adrc," in *2019 Chinese Control Conference (CCC)*, pp. 8020–8025, July 2019.

[67] A. Guclu, K. Arikan, and D. Kurtulus, "Hibrit İnsansız hava aracının yönelim dinamiklerinin hibrit denetimi," in *Ulusal Havacılık ve Uzay Konferansı*, 09 2016.

[68] K. Craig, "Observers in control systems." http://www.multimechatronics.com/wp-content/uploads/2017/04/course-notes/Observers-in-Control-Systems.pdf. Accessed: Jan. 2020.

[69] J. Songsiri, "Observer-based controller design." http://jitkomut.eng.chula.ac.th/ee635/obsv-fb-design.pdf. Accessed: Jan. 2020.

[70] Z. Gao, "Scaling and bandwidth-parametrization based controller tuning," in *American Control Conference*, vol. 6, pp. 4989–4996, 2003.

[71] Z. Z. B. Guo, *Extended State Observer*. John Wiley and Sons Ltd.

[72] D. Sun, "Comments on active disturbance rejection control," *IEEE Transactions on Industrial Electronics*, vol. 54, no. 6, pp. 3428–3429, 2007.

[73] T. Johansen and T. Fossen, "Control allocation—a survey," *Automatica*, vol. 49, p. 1087–1103, 05 2013.

[74] J. Bolling, W. Durham, J. Bolling, and W. Durham, *Control allocation with adaptive failure control*.

[75] J. Fan, Z. Zheng, and Y. Zhang, *Control Allocation-based Fault-tolerant Control for Over-actuated Systems with Saturation and Imperfect Fault Information*.

[76] M. Verhaegen, S. Kanev, R. Hallouzi, C. Jones, J. Maciejowski, and H. Smail, *Fault Tolerant Flight Control - A Survey*, pp. 47–89. Berlin, Heidelberg: Springer Berlin Heidelberg, 2010.

[77] L. Xulin and G. Yuying, "Fault tolerant control of a quadrotor uav using control allocation," in *2018 Chinese Control And Decision Conference (CCDC)*, pp. 1818–1824, 2018.

[78] C. Liu, X. Zhu, and B. Jiang, "Fault tolerant control based on adaptive control allocation with a multiple effectors aircraft application," in *2012 American Control Conference (ACC)*, pp. 2533–2538, 2012.

[79] W. Duan and D. Wang, "A fault-tolerant control method for satellite with uncertainties," in *Proceedings of the 33rd Chinese Control Conference*, pp. 3082–3087, 2014.

[80] J. Kim, I. Yang, and D. Lee, "Accommodation of actuator faults using control allocation with modified daisy chaining," in *2011 11th International Conference on Control, Automation and Systems*, pp. 717–720, 2011.

[81] W. C. Durham, "Constrained control allocation," *Journal of Guidance, Control, and Dynamics*, vol. 16, no. 4, pp. 717–725, 1993.

[82] J. Petersen and M. Bodson, "Constrained quadratic programming techniques for control allocation," *Control Systems Technology, IEEE Transactions on*, vol. 14, pp. 91 – 98, 02 2006.

[83] M. Chen, "Constrained control allocation for overactuated aircraft using a neurodynamic model," *IEEE Transactions on Systems, Man, and Cybernetics: Systems*, vol. 46, no. 12, pp. 1630–1641, 2016.

[84] L. Yang, Y. Zhong, and G. Shen, "Control allocation and management for aircraft with multiple effectors," in *2009 IEEE Aerospace conference*, pp. 1–8, 2009.

[85] O. Härkegård, "Dynamic control allocation using constrained quadratic programming," *Journal of Guidance, Control, and Dynamics*, vol. 27, no. 6, pp. 1028–1034, 2004.

[86] M. Bodson, "Evaluation of optimization methods for control allocation," *Journal of Guidance, Control, and Dynamics*, vol. 25, no. 4, pp. 703–711, 2002.

[87] J. Virnig and D. Bodden, *Multivariable control allocation and control law conditioning when control effectors limit*.

[88] M. Bodson, "Evaluation of optimization methods for control allocation," *Journal of Guidance, Control, and Dynamics*, vol. 25, no. 4, pp. 703–711, 2002.

[89] J. M. Buffington, *Modular Control Law Design for the Innovative Control Effectors (ICE) Tailless Fighter Aircraft Configuration 101-3, Tech. Rep. Report. AFRL-VA-WP-1999-3057*. Wright Patterson AFB.

[90] W. S. Levine, *The Control Handbook: Control System Applications, Second Edition*. CRC Press.

[91] D. Luenberger, *Introduction to Linear and Nonlinear Programming*. Addison Wesley Longman.

[92] T. Wang, L. Wang, J. Liang, and Y. Chen, "Autonomous control and trajectory tracking of quadrotor helicopter," in *2012 IEEE International Conference on Computer Science and Automation Engineering (CSAE)*, vol. 3, pp. 251–255, May 2012.

[93] E. Suicmez, "Trajectory tracking of a quadrotor unmanned aerial vehicle (uav) via attitude and position control."

APPENDIX A

CODE DEPLOYMENT FROM MATLAB TO PIXHAWK CUBE

In this study, all guidance and control algorithms are developed in Matlab/Simulink 2017b environment. To run the algorithms in real-time, they are deployed to a Pixhawk Cube controller board. Steps are given below followed during code deployment from MATLAB/Simulink to Pixhawk Cube controller board.

- Before installing the Pixhawk firmware, some basic programs such as Pixhawk Toolchain, Windows Ubuntu Bash, PX4 Ubuntu Compilers and MATLAB PSP support must be installed.
- **Pixhawk Toolchain** installer must be downloaded from PX4 website. After downloading, toolchain files must be installed according to the workspace, Figure A.1.

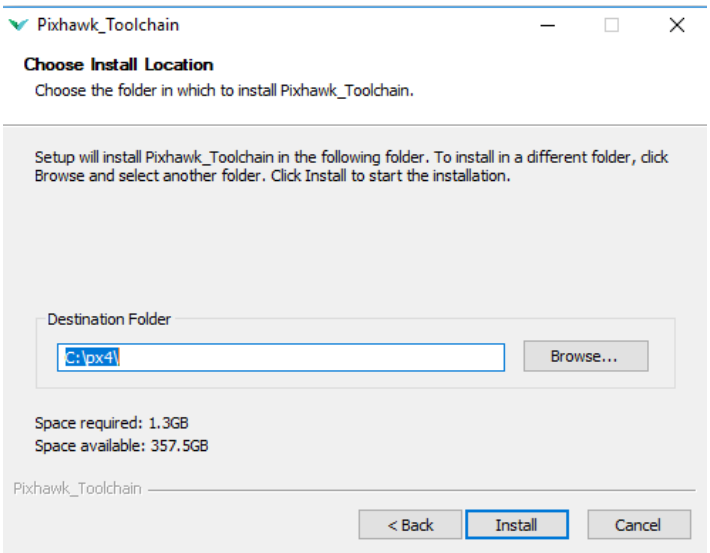

Figure A.1: Pixhawk Toolchain setup (screenshot)

- **Windows Ubuntu Bash 16.04** can be installed from Microsoft Store, Figure A.2.

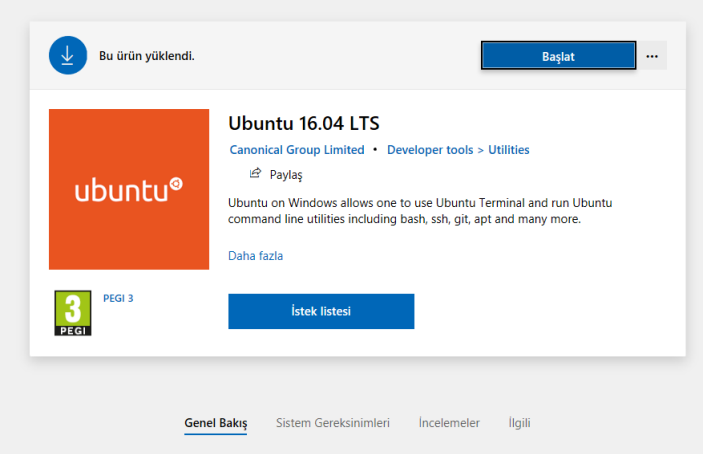

Figure A.2: Ubuntu Bash in Microsoft store (screenshot)

- A username and a password must be set at the end of the installation of the Windows Ubuntu Bash.
- A bash file must be installed from the link below;
  https://dev.px4.io/en/setup/dev_env_windows_bash_on_win.html
- Install the bash on Windows
- Open the bash shell
- Download the windows_bash_nuttx.sh from the link below;
  'wget http://raw.githubusercontent.com/PX4/Devguide/master/build_scripts /windows_bash_nuttx.sh'
- Run the script using the command below;
  source windows_bash_nuttx.sh
- **Matlab PSP Support Package** can be download from the link below;
  https://www.mathworks.com/hardware-support/px4-autopilots.html
- After the download is completed, PSP support is run with the command below in the command window;
  PixhawkPSP('c:\px4')

- Validate the path of the setup, download the firmware, and validate the firmware using 'PX4 Installation and CMake Configuration' window.
- Until the 4^{th} step, use C:\Windows\System32\bash.exe as bash path, Figure A.3.

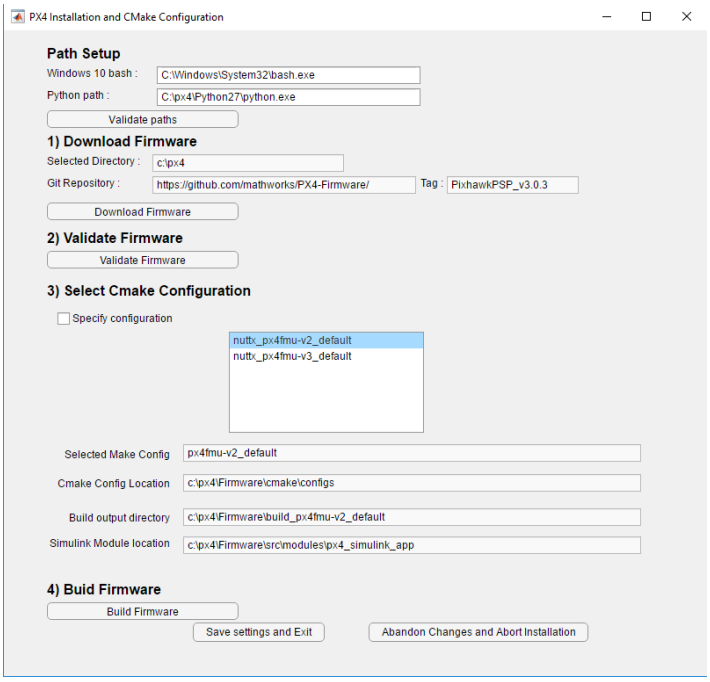

Figure A.3: PX4 Installation and CMake Installation (screenshot)

- Create a new file at location C:\Windows\named as Sysnative. And copy Bash.exe from C:\Windows\System32 to C:\Windows\Sysnative.
- Select Cmake Configuration as nuttx_px4fmu-v3_default.
- Change bash path as C:\Windows\System32\bash.exe.
- Build firmware.

CURRICULUM VITAE

PERSONAL INFORMATION

Surname, Name	: Güçlü, Anıl
Nationality	: Turkish (TC)
Date of Birth	: 30 October 1987
Place of Birth	: Keçiören/Ankara, Turkey
Phone	: +90 535 469 11 25
E-mail	: anilguclu@gmail.com

EDUCATION

Degree	Institution	Year of Graduation
M.S.	Atılım University, Mechatronics Eng. Dept.	2012
B.S.	Atılım University, Mechatronics Eng. Dept.	2009
High School	Kanuni Lisesi	2004

WORK EXPERIENCE

Year	Place	Enrollment
2018-2020	Roketsan Missile Inc.	Lead Engineer
2016-2018	Roketsan Missile Inc.	Senior Specialist Engineer
2014-2016	Roketsan Missile Inc.	Specialist Engineer
2010-2014	Roketsan Missile Inc.	Engineer
2009-2010	Atılım University, Mechatronics Eng. Dept.	Research Assistant

SKILLS

Computing : MS Office/VS

: MATLAB, Simulink

: LabVIEW, LabVIEW Real-Time, LabVIEW FPGA

Model Aircraft : Commercial pilot

: Autopilot designer/integrator

TRAININGS

PLC Siemens S7-300

LabVIEW Core 1-2

LabVIEW Real-Time

LabVIEW FPGA

TEACHING

2018-2019 Fall	MECE 539 Flying Robotics
2017-2018 Spring	MECE 522 Control Engineering II
2017-2018 Fall	MECE 521 Control Engineering I
2016-2017 Summer	MECE 306 System Dynamics and Control
	Atılım University, Mechatronics Eng. Dept.

2015	LabVIEW Real-Time
2014	LabVIEW FPGA
2013	LabVIEW Core 1-2
	Roketsan Missile Inc.

PUBLICATIONS

Thesis

1. Design of robust controllers for an outdoor quadrotor platform
   Atılım University, Mechatronics Eng. Dept., 2012

Journals

1. Güçlü A., Kurtuluş D.F., Arıkan K.B. Sabit ve Döner Kanatlı Hava Aracının Yönelim Dinamiklerinin Hibrit Denetimi, Sürdürülebilir Havacılık Arastırmaları Dergisi, SÜHAD 2016, pp.66-73, Cilt 1, Sayı 2.

2. Atlas E., Erdogan M.I., Ertin O.B., Güçlü A., Saygı Y.E., Kaynak Ü.,Kasnakoglu C., Hardware-in-the-loop Test Platform Design for UAV Applications, Applied Mechanics and Materials, 2015, DOI:10.4028/www.scientific.net/AMM.789-790.681.

Conferences

1. Güçlü A., Arıkan K.B., Kurtulus D.F., Hibrit Hava Aracı Yükseklik ve Yönelim Dinamiklerinin Çok Girdili Çok Çıktılı Dogrusal Aktif Bozucu Savurucu ile Denetimi, Otomatik Kontrol Ulusal Toplantısı, TOK 2018, Kayseri.

2. Güçlü A., Kurtulus D.F., Arıkan K.B., Attitude and Altitude Stabilization of Fixed Wing VTOL Unmanned Air Vehicle, AIAA Modeling and Simulation Technologies Conference, AIAA 2016, Washington D.C. USA.

3. Güçlü A., Arıkan K.B., Kurtulus D.F., Hibrit Insansız Hava Aracının Yönelim Dinamiklerinin Hibrit Denetimi, Ulusal Havacılık ve Uzay Konferansı, UHUK 2016, Kocaeli.

4. Akyürek S., Güçlü A., Kaynak Ü., Kasnakoglu C., Insansız Hava Araçları için Çift Telli Sarkaç Kullanılarak Atalet Momentlerinin Hesaplanması ve Otopilot Tasarımı, Otomatik Kontrol Ulusal Toplantısı, TOK 2016, Eskisehir.

5. Güçlü A., Atay Y., Genc Y., A Development Study on Performance of a Real-Time Interface Device, Progress in Systems Engineering, ICSEng 2014, Las Vegas, USA.

6. Güçlü A., Aliew F., Çizgisel Düzlemdeki Sarkacın Bulanık Mantık Denetimci Tipi ile Denetimi, Otomatik Kontrol Ulusal Toplantısı, TOK 2013, Malatya.

7. Güçlü A., Arıkan K.B., Irfanoglu B., Dört Döner Kanatlı Dıs Ortam Hava Aracının Yönelim ve Yükseklik Denetimi, Otomatik Kontrol Ulusal Toplantısı, TOK 2012, Nigde.